DESIGN OF AN ULTRA-WIDEBAND FREQUENCY SYSTEM FOR NON-DESTRUCTIVE ROOT IMAGING

A Thesis Submitted to the
College of Graduate and Postdoctoral Studies
in Partial Fulfillment of the Requirements
for the degree of Master of Science
in the Department of Electrical and Computer Engineering
University of Saskatchewan
Saskatoon

By
Thomas Truong

Permission to Use

In presenting this thesis in partial fulfilment of the requirements for a Postgraduate degree from the University of Saskatchewan, I agree that the Libraries of this University may make it freely available for inspection. I further agree that permission for copying of this thesis in any manner, in whole or in part, for scholarly purposes may be granted by the professor or professors who supervised my thesis work or, in their absence, by the Head of the Department or the Dean of the College in which my thesis work was done. It is understood that any copying or publication or use of this thesis or parts thereof for financial gain shall not be allowed without my written permission. It is also understood that due recognition shall be given to me and to the University of Saskatchewan in any scholarly use which may be made of any material in my thesis.

Requests for permission to copy or to make other use of material in this thesis in whole or part should be addressed to:

Head of the Department of Electrical and Computer Engineering
57 Campus Drive
University of Saskatchewan
Saskatoon, Saskatchewan, Canada, S7N 5C9

and

College of Graduate and Postdoctoral Studies
Room 116 Thorvaldson Building, 110 Science Place
University of Saskatchewan
Saskatoon, Saskatchewan, Canada, S7N5C9

Abstract

This thesis outlines the design and implementation of an ultra-wideband imaging system for use in imaging potted plant root system architectures. Understanding the root system architecture as plants develop is critical for plant phenotyping and ultra-wideband imaging systems have shown potential as a portable, low-cost solution to non-destructively imaging root system architectures. The proposed system is separated into three main subsystems: a Data Acquisition module, a Data Processing module, and an Image Processing and Analysis module. For each module, essential parameters and variables which largely affect the quality of the produced images and measurements of the system are analyzed and discussed.

The Data Acquisition module is responsible for collecting ultra-wideband signal reflections off the potted roots in dry soil. The most critical variables for performance of the entire system are the relative permittivities of the root and the soil. Insufficient contrast between root and soil relative permittivity results in poor performance of the imaging system. Both simulated (using finite-difference time-domain methods) and experimental trials were performed and designed for data collection. The Data Processing module receives the ultra-wideband reflection data from the Data Acquisition module and produces a 2D image using delay-and-sum beamforming. This method takes advantage of known physical and electrical parameters to generate an energy mapping of reflective objects in the soil medium to be imaged. Careful design of parameters such as the steering vector and window size are essential to optimizing the quality of the results.

The Image Processing and Analysis module removes any artifacts present in the produced images from the Data Processing module by primarily using morphological transformations. A modified top-hat transformation is used and the size of the structuring elements help remove unwanted artifacts.

The system performs reasonably well under controlled soil conditions, and there are large improvements to be made with increasing the bandwidth of the ultra-wideband device. However, since the performance of the device is extremely reliant on the soil conditions, it is recommended that further work on ultra-wideband imaging systems for roots to be focused on measuring and modeling the complex electromagnetic properties of soil at high frequencies.

Acknowledgements

I would like to thank my supervisors Dr. Anh Dinh and Dr. Khan Wahid. Their continued mentorship and confidence in my ability to independently research my own topics has provided me the opportunity to pursue a career path in research.

I would also like to thank my friends for making my time in school a memorable and enjoyable experience.

Finally, I cannot put into words how appreciative I am for all the support and care which my parents have given me. My accomplishments have only been possible because of their dedication to immigrate to Canada and give my sister and I the best possible life they could.

Contents

List of Tables

List of Figures

List of Abbreviations

CT	(X-ray) Computed Tomography
DAS	Delay-and-sum
EIS	Electrical Impedance Spectroscopy
EM	Electromagnetic
ERT	Electrical Resistivity Tomography
FDTD	Finite-difference Time-domain
GUI	Graphical User Interface
GPR	Ground Penetrating Radar
MIMO	Multiple-Input Multiple-Output
MRI	Magnetic Resonance Imaging
P410	PulsON 410
RSA	Root System Architecture
SAR	Synthetic Aperture Radar
SUT	System Under Test
TEz	Transverse Electric (polarization)
TMz	Transverse Magnetic (polarization)
PET	Positron Emission Tomography
UWB	Ultra Wide-band

Chapter 1

Introduction

This chapter seeks to define the problem background and the reasoning for the need of the development of a non-destructive root imaging system. This chapter also presents the research objectives of this thesis and provides an overview of the content of the thesis.

1.1 Problem Background

Ensuring high crop production yield is critical in maintaining global food security [1–3]. Global crop demand is expected to double by 2050 [4], requiring crop yield increases of 2.4% annually [3]; however, current global efforts are only increasing crop yield by about 1.3% annually [2,3]. A large portion of this deficit is because 30% of the land used for crop growing has stagnant or falling annual crop yields due to unfavourable environmental conditions [5]. The method of selective breeding to create environmentally stress tolerant crops has been the most effective method for maximizing crop yields for the last half century [3]. Selective breeding methods rely on the analysis of the gene-environment interactions which are exhibited through physical characteristics in the plants [6]. This process of collecting and analyzing environmental responses and physical characteristics is called plant phenotyping and has been an essential method for meeting global crop demands. Unfortunately, effective phenotyping of crops requires large quantities of accurate environmental and plant data [3]. The lack of reliable information on growing environments and individual plant measurements has bottlenecked advancements in improving crop yield [6]. Narrowing the issue further, the non-destructive collection of accurate data on roots, a complicated organ that is critical in the development of the plant, has proven to be a significant challenge which further inhibits plant phenotyping research [7,8]. The challenge of characterizing plant roots comes with the hidden nature of the roots as they are concealed by the medium they are grown in. As such, a low-cost and portable non-destructive device and imaging algorithm which measures the characteristics of plant roots would greatly benefit the field of plant phenotyping by providing root information to plant scientists who can use the informationto improve crop yields and help meet global demands.

In the past, methods for root measurements were labour intensive and highly destructive which often inhibited the development of the roots. A common method was a root excavation which required physically removing the plant from its growing medium to measure characteristics [9]. The cumbersome and destructive nature of this method made it difficult for researchers to properly record and analyze the growth of the roots. More recently, methods utilizing advanced imaging techniques such as magnetic resonance imaging (MRI) [10], positron emission tomography (PET) [11], and ultra-wideband imaging [8] have been in development for use in root phenotyping research. In particular, ultra-wideband (UWB) devices have been increasingly popular for imaging concealed structures. The compact form and low-cost of ultra-wideband equipment relative to the equipment required for MRI and PET makes UWB an attractive option for potential use in root phenotyping purposes [12].

1.1.1 The Importance of Roots and Root Phenotyping

Healthy roots are critical to the development and productivity of a plant on numerous levels. Roots bring in water and nutrients, store essential resources, and anchor the plant to the growing medium [13]. The term root system architecture (RSA) is used to describe the spatial distribution of the root within the growing medium. The RSA is highly dynamic and knowledge of the RSA as it develops is crucial for understanding how different root traits can benefit a plant's development and productivity [14]. Due to the root's role in plant development, plant scientist's have heavy interest in being able to non-destructively measure and determine crucial characteristics in the RSA in order to breed optimally productive crops which respond well to various environmental stresses. For example, characteristics such as primary root length [15] and root diameter [16] determine how much access the plant has to stored water and how well the plant can penetrate harder growing mediums. The deeper the root the better the access and the larger the diameter the better the penetration.

Plant phenotyping allows researchers and crop field managers understand which breeds have favourable root characteristics for the environment they are being grown to maximize crop productivity [3]. Being able to non-destructively image the RSA and measure characteristics like root depth and root diameter becomes essential for plant phenotyping.

1.2 Research Objective

In efforts to improve information acquisition on roots for plant phenotyping purposes, the primary goal of this thesis project was to develop and evaluate the feasibility of an UWB imaging system as a low-cost and portable solution to non-destructively measure potted taproot plants. The project sought to identify and analyze critical system parameters which dictate the quality of the produced images and measurements.

The system collected pertinent UWB signal data, processed the data to form an image, and then analyzed and measured characteristics of the root using the produced image. Potted taproot systems were the primary system of interest to be imaged because taproot systems contain a large primary root which is advantageous for testing the capabilities of ultra-wideband technology for root imaging. The primary quantitative metrics used in this thesis will be the error in the root depth and root diameter measurements.

1.3 Thesis Overview

This chapter, Chapter 1, introduces the necessary background information needed to demonstrate the need for the development of a non-destructive root imaging system. Chapter 1 introduces the primary goal of this thesis, which is to discuss the development of an UWB based root imaging system and analyze and evaluate the system's capabilities and potential for use in root phenotyping purposes.

Chapter 2 seeks to provide literature on current efforts and other technologies used to measure and analyze the RSA. Chapter 2 also provides literature on recent efforts to use UWB based devices to image concealed objects and structures.

Chapter 3 contains a a high level description and block diagram of the system and methodology used to generate non-destructive root images on both simulated and experimental roots. The chapter primarily seeks to provide the reader a general sense of the modules developed and the technical tasks they accomplish to contribute to the non-destructive root imaging system.

Chapter 4 provides the low level description and the technical details of the system modules needed to image a simulated pot and root model. Derivations of the methods used to generate, process, and analyze the UWB signals are presented in this chapter.

Chapter 5 contains the results and analysis of important system parameters for the developed imaging system. System limitations and potential methods of improvement are explored.

Chapter 6 discusses the implementation details of the experimental trials and the necessary modifications needed to developed system modules to operate with the PulsON 410 UWB signal emitting device.

Chapter 7 analyzes the results of the experimental trials implemented in Chapter 6. The chapter also recreates the circumstances of the experimental trials using simulations in order to examine potential sources of improvement for the system.

Chapter 8 concludes the findings of the thesis, provides general remarks and insight into the system developed, and offers suggestions for future work and sources of improvement.

Chapter 2

Literature Review

Section 2.1 summarizes current methods which are used for non-destructive root phenotyping. This subsection briefly describes several methods and determines the feasibility of each method based on the scope of this project. Section 2.2 is a review of UWB imaging theory and applications. The section also covers the potential of UWB devices to be used for non-destructive root phenotyping.

2.1 Current Methods for Non-destructive Root Phenotyping

A summary of the various non-destructive root phenotyping methods is given on Table 2.1.

Table 2.1: Summary of current methods used for non-destructive root phenotyping.

Method	**Approximate Cost**	**Portability of equipment**	**Resolution**	**Other notes**
Rhizotrons	50-100,000 USD [17]	low	mm to cm scale	higher costs result in higher throughput
MRI	>50,000 USD [18]	low	mm scale	
PET	>75,000 USD [19]	low	mm scale	uses potentially harmful radiotracers
X-ray CT	>50,000 USD [19]	low	mm scale	uses potentially harmful high energy EM radiation
EIS	>3,500 USD [20]	high		no image produced
ERT	>200 USD	high	dm scale	
GPR and UWB	>5000 USD [21]	medium-high	cm scale	UWB root imaging has little research

Rhizotrons

Rhizotrons are structures constructed specifically for studying root and soil interaction [22]. Generally, rhizotron structures are built with reinforced glass walls and the plant is grown within those walls in order to observe root growth. Plants are grown either within or around the rhizotron and their growth is observed through the glass. Rhizotrons are often used in combination with RGB and infrared imaging devices in order to characterize roots [23].

One of the primary issues with rhizotrons include their high associated size and monetary costs of construction and maintenance [23]. Other issues include the adverse effects on the natural growth of roots if the roots are grown in transparent media such as a hydroponic solution or if the roots are constrained by the size of the rhizotron [23].

Magnetic Resonance Imaging (MRI)

MRI is a common imaging technique used in the medical field to detect concealed structures in the human body with high resolution. It only follows that MRI has found use in researching plant roots. It has been used to research the effect of pot size on root structure [24]. Additionally, because of the high resolution, research has been done on damage to sugar beet roots caused by disease in the lab [10].

Unfortunately, MRI is not feasible for many places for use high throughput root phenotyping. The associated costs and the bulkiness of the equipment restricts the ability of MRI technology to be used in plant phenotyping. Studies often required expensive rental time on third party MRI machines. Moreover, MRI has difficulties imaging roots in most natural soils [25].

Positron Emission Tomography (PET)

PET is a technique also often used in the medical field to detect concealed structures. PET images are produced by detecting positrons emitted by a radioactive isotype which is injected to the system to be scanned [26]. This results in very high quality images of roots, and can be used in conjunction with other imaging techniques to acquire complementary information [11, 26]. MRI-PET imaging techniques are continuing to be developed for both plant phenotyping and medical imaging [9].

Also similar to MRI, PET is not feasible for high throughput root phenotyping for most applications due to the costs and bulkiness of the equipment required.

X-ray Computed Tomography (CT)

X-ray CT is capable of producing non-destructive 3D root images measuring the interactions of high energy electromagnetic waves with the system to be imaged [9]. X-ray CT is capable of delivering very high quality models of the RSA [27–29].

Once again, X-ray CT, much like the other medical imaging techniques, is encumbered by needing the use of expensive and bulky scanning equipment, making it unsuitable for use in many facilities.

Electrical Impedance Spectroscopy (EIS)

Electrical Impedance Spectroscopy involves characterizing materials through impedance measurements at varying frequencies of alternating current. The impedance measurements can be correlated to various qualities of the root such as biomass and surface area. The EIS measurements in successful journals generally use a two electrode set up to excite the voltages and measure root biomass and root surface area [9,30,31]. Measurements of root biomass and root surface area can be quickly and roughly estimated using EIS [30]; however, using EIS for phenotyping purposes is severely limited as EIS cannot produce images of the concealed roots [9].

The simplicity and speed of EIS measurements makes EIS worth investigating in the field of high-throughput phenotyping, but the focus for this thesis will be on imaging methods which can reveal more information than just surface area and biomass.

Electrical Resistivity Tomography (ERT)

Electrical Resistivity Tomography involves measuring the spatial distribution of soil resistivity. Roots are detected through mapping the soil resistivity on a plane and then analyzing the anomalies in the resistivity distribution. Generally, successful applications ERT in imaging roots is done with arrays of electrodes [32, 33]. This method is capable of producing 2D and

3D images of plant roots at a low resolution. ERT has been developed well enough to be utilized for *in situ* measurements of tree root mass distribution as well as tree root morphology [32]. ERT becomes ineffective for plants with lower root densities such as alfalfa [33].

The tap root system of canola plants have a density which lies between that of alfalfa and larger tree roots; however, the resolution of the produced images are quite poor for *in situ* applications. As such, using ERT for plant root phenotyping may be feasible and worthwhile to investigate in the future, but other methods of root phenotyping will be explored for this project as the resolution of ERT is questionable.

Ground Penetrating Radar (GPR) and Ultra-wideband (UWB) Imaging

In the past, GPR ($\sim$100 MHz-2 GHz frequencies) has been popular for geological surveying. Additionally, there have also been studies on the use of conventional GPR to measure tree roots with varying success in tree root imaging [34, 35], through pavement tree root locating [36], and tree root biomass estimating [37]. The technology involves mapping propagating electromagnetic waves phenomena through soil and root structures [36]. Generally, GPR transceivers are placed above ground and is highly dependent on soil composition as well as root orientation which limits its usage to large tree roots and roots that are in homogenous soils [9, 34].

More recently, UWB imaging has been partially successful in non-destructively imaging lower density plant roots such as sugar beet root [8]. UWB technology uses a broad frequency spectrum (as opposed to smaller frequency bands as in conventional GPR) to image materials [8, 38]. Although UWB technology is relatively new in the field of root phenotyping, it has been successful in other applications such as concealed weapon detection [12, 38], through wall imaging [12, 38], and biomedical imaging [12, 39].

UWB imaging techniques and its success in other fields sparks interest in developing an UWB system to determine its feasibility in plant root phenotyping. UWB imaging techniques show great promise for its application in high-throughput root phenotyping which warrants further research and investigation on the technology.

2.2 Ultra-wideband Sensing and Applications

2.2.1 Definition and Theory

UWB spectrums are defined by having either a large -10 dBm fractional bandwidth ($b_0 \geq 0.2$) or a large -10 dBm absolute bandwidth ($B \geq 500$MHz) as defined by Spectrum Management and Telecommunications Radio Standards in Canada [40]. -10dBm is the threshold value as determined. Fractional and absolute bandwidths are defined as follows [12]:

$$b_0 = \frac{B}{f_m} = 2\frac{f_u - f_l}{f_u + f_l}$$
$$B = f_u - f_l$$

where:

- b_0 is the fractional bandwidth, unitless.
- B is the absolute bandwidth, Hz.
- f_m is the centre frequency, Hz.
- f_u is the upper cut-off frequency, Hz.
- f_l is the lower cut-off frequency, Hz.

In the time domain, this spectrum is produced by a short pulse (generally with energy concentrated around 1 ns for GHz frequencies) [12].

UWB radar involves transmitting an UWB pulse through the system under test (SUT) and receiving and processing the response from the SUT to detect the presence of concealed objects, much like conventional radar.

There are many design choices involved in UWB radar, such as operating frequencies, fractional bandwidth, number of transmitters/receivers, and transmitter/receiver configurations. Regardless of set-up, UWB radar focuses on measuring reflectance/transmittance of UWB signals from a SUT. These measurements can then be used to generate images of concealed objects within the SUT. Like conventional radar, UWB radar needs compensation systems that deal with unwanted wave phenomena.

2.2.2 Concealed Weapon Detection

Concealed weapon detection using UWB radar imaging has been highly successful in preliminary designs using a single transceiver synthetic aperture radar (SAR) [12,38], and multiple-input-multiple-output synthetic aperature radar (MIMO SAR) [38].

A single transceiver SAR utilizes a moving platform and multiple scans on a spatially static system to emulate a physical aperture radar array. This system allows imaging of static objects with only a single transmitter and receiver [12]. With this antenna set-up concealed weapons on dressed human analogues were easily detected. One study used a cylindrical scanning scheme for its SAR system to image the human analogue and clearly pinpoint the concealed weapon [12]. Figure 2.1 shows the results of the study [12].

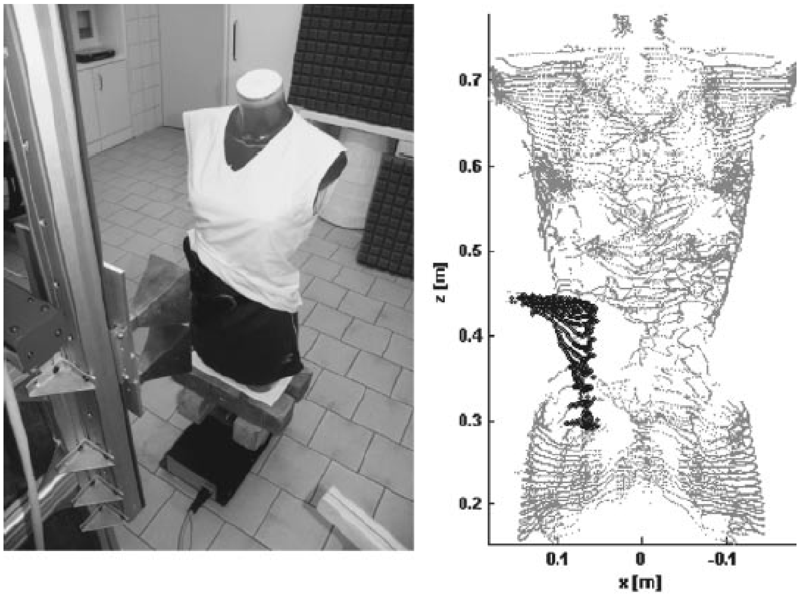

Figure 2.1: Female torso analogue with a concealed weapon and UWB surface reconstruction of analogue and the detection of the weapon.

One downside of a single transceiver SAR is that it requires many scans, and thus a long measurement time. A MIMO SAR is a balance between a single transceiver SAR and a full aperture radar array. The amount of scans is reduced significantly by introducing more transmitters and receivers. In his PhD Thesis, Xiaodong Zhuge demonstrated that a mannequin with a concealed revolver and knife was imaged using both a single transceiver SAR and MIMO SAR set-up. Both set-ups have nearly identical performance, and both were able to successfully identify the revolver and knife (circled for emphasis on figure) [38]. Figure 2.2 shows the results of the single transceiver SAR setup.

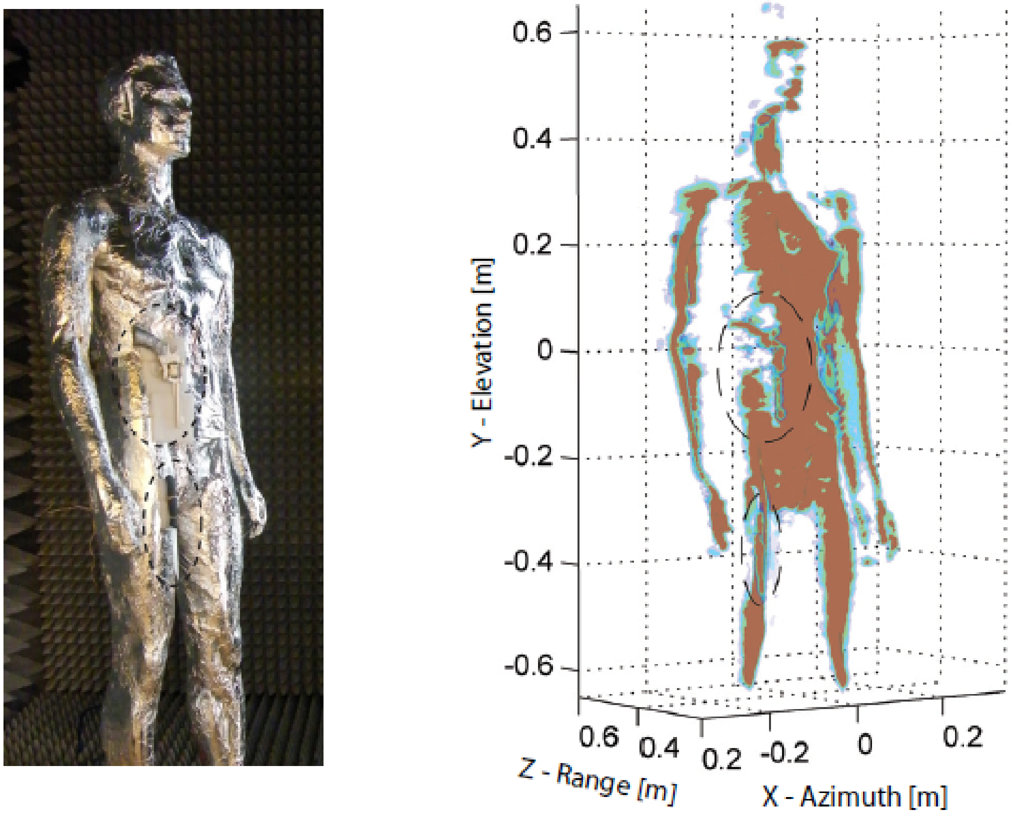

(a) RGB image of mannequin under test.

(b) UWB captured image of mannequin under test.

Figure 2.2: Images for (a) mannequin under test with concealed weapons and (b) reconstructed mannequin image using single transceiver SAR

2.2.3 Breast Cancer Screening

UWB sensing and imaging and its applicability in early breast cancer screening has been a popular topic since the late 1990s [12]. If further developed, it may be the preferred technology for early stage screening of breast cancer since it uses non-ionizing radiation is cost-effective when compared to X-ray imaging and MRI, respectively [12, 41, 42]. UWB imaging for breast cancer screening has been successful with imaging breast phantoms and has had varying success in clinical trials [41, 43, 44].

There are two major antenna configurations for UWB breast cancer screening: non-contact based and contact based.

In non-contact based screening, the antennas make no contact with the breast, much like in a SAR set-up. This configuration is less useful for breast cancer screening due to low signal penetration into the breast tissue because of high dielectric contrast between the medium surrounding the breast and the breast tissue [12].

Contact based screening has had the most success in correctly identifying tumours in breast tissue. In most setups, the antenna is not in direct contact with the breast tissue, but instead in contact with media that is specially designed to promote signal penetration into breast tissue. One study uses a medium with dielectric constant matched to breast fat [44], while another study uses a ceramic shell and paraffin coupling medium to remove air gaps between antenna and breast tissue [43]. Figure 2.3 shows clinical images of a detected tumour in breast tissue using a device developed by the University of Bristol [44].

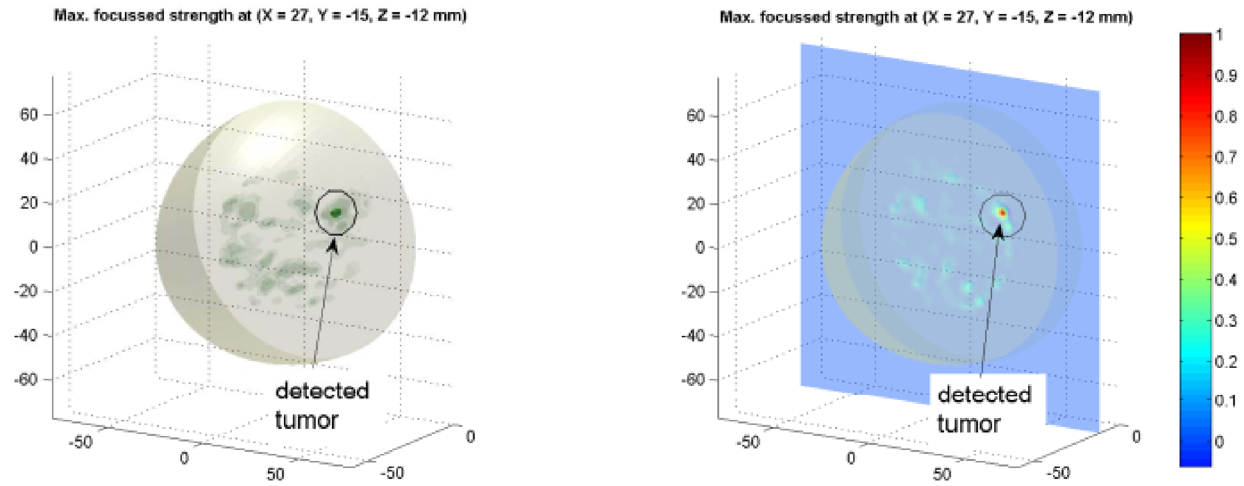

Figure 2.3: 3D clinical image using radar-based UWB and 2D Image of the plane where the tumour was detected.

All studies in this section utilize a delay-and-sum (DAS) beamforming algorithm for image formation. DAS beamforming creates an image by mapping backscattered energy as a function of space [12].

2.2.4 Sugar Beet Root Imaging

There has been one study [8] and PhD. thesis [45] on using UWB technology to image roots, both conducted by Christian Peveling-Oberhag at the University of Bonn for the department of Agricultural Engineering. Peveling-Oberhag had limited success in imaging roots of sugar beets and chard roots, however the design did not perform sufficiently to the specified goals of developing an automated cost-effective mobile sensor system to image and measure these roots.

Peveling-Oberhag designed a system that was based on a non-contact single transceiver SAR, much like the systems presented in previously in this section. The system consisted of a transceiver mounted on a linear actuator and a system under test (a potted sugar beet root or a chard root) was placed on a rotary actuator. The study used only basic time-gating methods to capture the data and simple filtering techniques to improve results [45]. There were issues with the linear actuator which, as stated in the dissertation, caused major problems with the accuracy of the images.

Chapter 3

Methodology Overview

This chapter intends to provide high level description of the methods used to develop the ultra-wideband imaging system described in Section 1.2, the research objective. Section 3.1 covers the high level system diagram and system block interactions for the system developed. Section 3.2 provides a high level description of the methods used in each of the system blocks for the simulated trials. Section 3.3 provides a high level description of the methods used in each of the system blocks for the experimental trials.

Low level descriptions and implementation details will be covered in Chapter 4 for the simulated trials and Chapter 6 for the experimental trials.

3.1 Simulation and Experimental Methodology Overview

The design of the ultra-wideband imaging system will be broken up into three main modules: a Data Acquisition module, a Data Processing module, and an Image Processing and Analysis module. Figure 3.1 shows the very high level block diagram for the system.

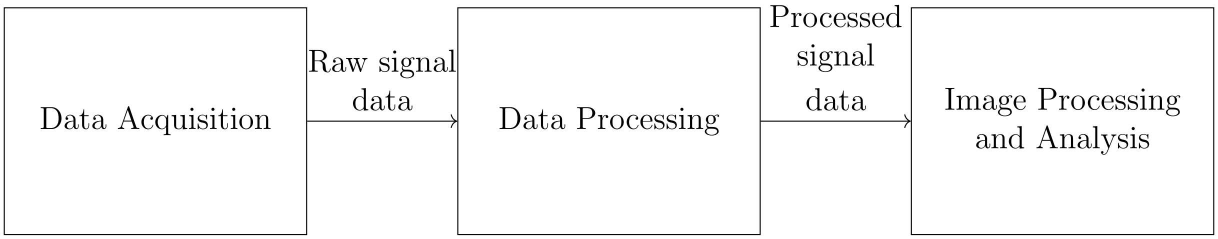

Figure 3.1: High level system block diagram for the ultra-wideband imaging system.

The Data Acquisition Module will mostly consist of the hardware and software needed to either simulate data or collect live data from experimental trials. Initially, the UWB device to be used for this project, the PulsON 410 (P410), was unavailable for use so the primary source of data was from simulations in MATLAB. These simulations used the finite-difference time-domain method to provide temporal signals of UWB reflections off of a digital pot and root model. Once the P410 arrived, an apparatus was constructed to collect data using the procedure developed in the simulations.

The data from these simulation trials allowed the development of the Data Processing module without needing to wait for data from experimental trials. Additionally, it allows for the analysis of results and parameters without needing to implement time and cost intensive hardware. Processing methods such as time gating and delay-and-sum (DAS) beamforming were used to form 2D images. Other methods included using Wiener filters and bandpass filters to reduce noise in the received UWB signal for the experimental trials.

The Image Processing and Analysis module measures the root depth and root diameter of the generated images. Image processing methods included top-hat transforms and image segmentation. Analysis tools included using energy histograms, segmentation methods, and interpolation methods to quantify the quality of the imaging system. Both simulated results and experimental results were quantified using the same metrics to allow for the analysis of potential sources of improvement in the experimental results.

3.2 Simulation Methodology

A non-contact, mono-static, single transceiver SAR system using UWB frequencies will be simulated to test the feasibility of this system configuration for non-destructive root imaging. This setup was selected based on its application in other fields such as hidden weapon detection and breast cancer screening. 2D simulations were done using the finite-difference time domain (FDTD) method to evaluate the feasibility of the proposed system. MATLAB was used to implement the simulations. A 2D model sufficiently modeled EM phenomena with relatively low computing power (when compared to 3D simulations). A configurable simulation will be set up to allow for adjustable electrical and physical properties on the soil, plant roots and pot medium. The 2D simulation will provide data to demonstrate how unwanted EM phenomena can be dealt with through various data collection and processing techniques such as time-gating, delay-and-sum beamforming, and noise rejection filters. Once

2D images are formed, measurements of root depth and average root diameter are made using segmentation and interpolation methods.

3.2.1 Data Acquisition

Physical Parameter Modeling

The simulations will be modeling a simple potted taproot. The constant physical parameters are shown in Figure 3.2. The distance from the surface of the soil to the bottom interior of the pot is 40 cm while the distance from the left interior of the pot to the right interior of the pot is 25 cm. The root diameter and root depth will be adjustable parameters during simulations. The pot wall width will be determined to minimize reflections at the carrier frequency. The distance of the transceiver to the exterior pot wall will be dependent on the thickness of the pot wall, but generally will be approximately 1.5 cm.

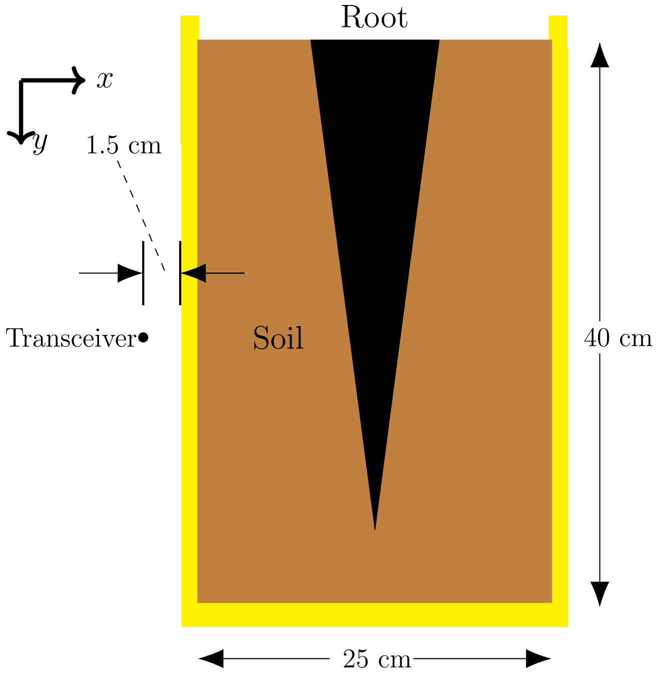

Figure 3.2: Physical parameters on pot and root model.

The vertical position of the transceiver will vary according to the number of scans that will be taken. The number of scans plays an important role in determining simulation time as well as experimental trial time, so an optimal number of scans had been determined with these simulations. Each vertical position is simulated to emit an UWB pulse from the transceiver and the subsequent reflections will be measured by the transceiver.

Electrical Parameter Modeling

Accurate electrical parameters for all materials in the system being simulated are needed for good simulation results that are reflective of real life phenomena. The most important electrical parameters for doing FDTD simulations are the relative permeability and relative permittivity. For the most part, the materials concerned with in this project are non-magnetic which simplifies the implementation of FDTD. The difficult parameter to determine is the relative permittivity of the materials involved.

In particular, the soil relative permittivity at high frequencies can be modeled in many ways, each with different results [46–48]. The accuracy of the models is highly dependent on soil characteristics such as soil composition and moisture content [46]. For the purposes of this project, a simple linear, isotropic, and non-dispersive model was used and was found to be sufficient to model experimental results. However, in the future this is a major topic of research that needs to be done to improve non-destructive root imaging techniques in general.

An advantage of using a pot to hold the soil is that it can act as a coupling medium for the transceiver and minimize unwanted reflections from the surface of the pot. As such, the permittivity and physical width of the pot in simulations were designed to minimize reflection from the pot wall.

3.2.2 Data Processing

The data received from the Data Acquisition Module is processed to create 2D images to be used for the measurement and analysis of the roots being scanned. Delay-and-sum beamforming was chosen to be implemented because it has been very successful in forming images for UWB breast cancer screening [41, 43, 44].

Delay-and-sum Beamforming

Delay-and-sum (DAS) beamforming takes advantage of known physical and electrical parameters to estimate the round-trip path time of propagating UWB waves from transmitter to receiver [12]. Any object within the soil medium that has a different relative permittivity than the soil will reflect energy back to the receiver, but the position of these objects are generally unknown. With DAS beamforming, we can generate an image which represents the reflected energy at each point from within the medium to be imaged.

The distances denoted r_1, r_2, r_3, and r_4 in Figure 3.3 are determined and the time it takes for the wave to travel this path was calculated. This time is used to estimate the reflected energy caused by any potential reflectors at the imaging point. This process is then iterated for many different imaging points and transmitter/receiver locations over the region of interest. After many iterations, an image is formed by combining the energy measurements are each imaging point and generating a spatially ordered array.

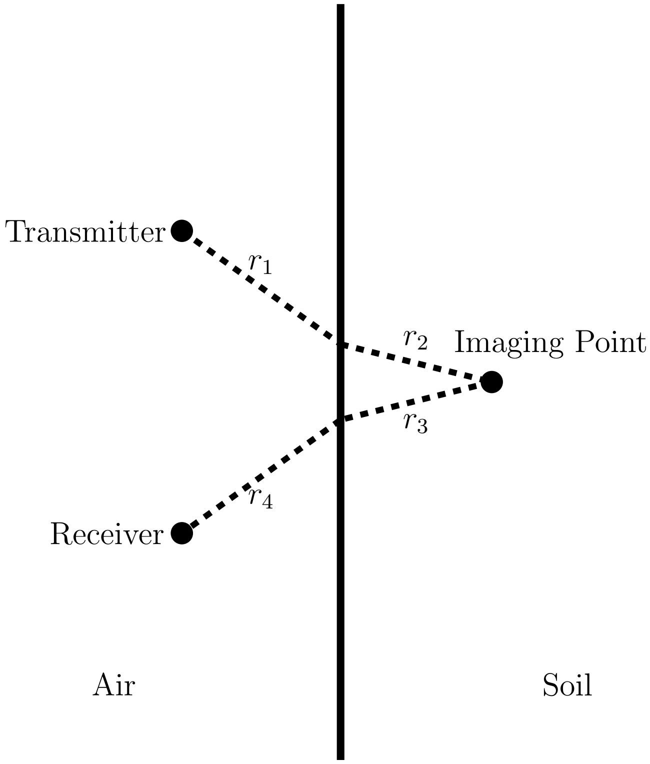

Figure 3.3: Example of ray paths calculated to the imaging point for DAS beamforming.

3.2.3 Image Processing and Analysis

The Image Measurement and Analysis module uses the 2D images to measure the depth and diameter of the potted carrot. Modified top-hat transformations and quantization methods were used to remove unwanted artifacts. These methods use information from analysis tools such as energy histograms to provide optimal images for measurement.

Image Histograms and Energy Histograms

An image histogram for an grayscale image is the plot of frequency of occurrence against the pixel intensity. The pixel intensities in the generated 2D images are correlated with the measured reflected energy from reflections. As such, we can multiply the pixel intensity with the number of occurrences at each pixel intensity and plot this value against the pixel intensity to arrive at an energy histogram. A completely homogeneous soil medium with a good relative permittivity contrast between root and soil will have an energy histogram that shows that most of the energy is concentrated in the higher pixel intensities. This is an important tool to estimate the amount of noise and clutter present within an image in an unsupervised fashion.

Root Depth and Diameter Measurement

The depth and the diameter measurements are the primary metrics for determining the quality of the imaged root. The height is measured by flattening the image along the vertical axis by detecting the presence of the root along each horizontal row. The average diameter is then calculated by calculating the area of the root and dividing it by the height. Since the simulation parameters are known exactly and error can be calculated and these measurements are used primarily to judge the quality of the image produced.

3.3 Experimental Methodology

A non-contact, bi-static SAR system using the P410 will be simulated to test the feasibility of this system configuration for non-destructive root imaging. The device emits a 3.1 GHz to 5.3 GHz UWB pulse. The scanning procedure was designed to match the procedure designed in the FDTD simulations. A MATLAB GUI was used to collect scans and save the data which was easily integrated with the data processing and image processing algorithms developed in the simulations. The data processing module was mostly the same and used DAS beamforming to create a 2D image. The only difference in the experimental trials was some additional processing in the form of Wiener filters and bandpass filters which were needed to remove unwanted noise caused by the P410 device. The Image Processing and Analysis module is identical for analyzing the generated 2D images from DAS beamforming except for how the ground truth depths and diameters were determined. Unlike the simulations where the imaged carrot's physical parameters are known exactly, the ground truth depth and diameter measurements for the experimental trials were made by measuring an RGB photo of the carrot.

3.3.1 Data Acquisition

An apparatus was constructed using the P410 to perform image potted carrots. The P410 was interfaced with MATLAB using a USB port. Since the P410 does not have a collocated transceiver, a non-contact, bi-static SAR scanning procedure was used. The apparatus allowed for easy adjustment of the transceiver height using a ball bearing platform and a clamping tool. Calibrating tests were done to measure the device's delays in scanning time and data acquisition. A graphical user interface (GUI) was designed in MATLAB to streamline the scanning process and shorten scanning times.

Physical Set-up

Figure 3.4 shows the physical dimensions of the potted taproot. The main difference between the experimental set-up and the simulated set-up is the separation of the transmitter and receiver by 4 cm since the P410 uses separate antenna for transmitting and receiving. The vertical positions of the transmitter were adjusted based on the center of the transmitting antenna. Other differences include the depth of the soil, size of the pot, and size of the taproot (a carrot is chosen) due to the availability of materials for the apparatus.

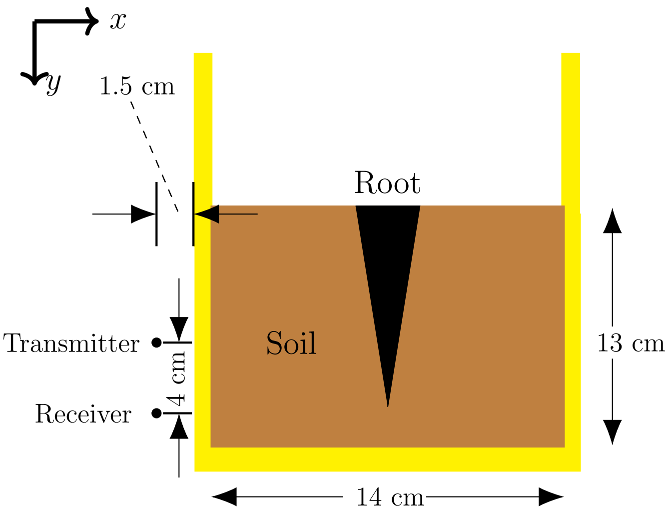

Figure 3.4: Dimensions of the P410 imaged potted carrot.

Scanning Procedure and Graphical User Interface

The GUI was designed in MATLAB to streamline the scanning process of buried carrots. The user inputs the number of vertical positions, the number of scans to average per vertical position, and the number of rotational positions. Once the scans are completed, the collected data is then saved in a .mat format for processing.

3.3.2 Data Processing

The Data Processing Module for the experimental trials uses similar methods as the simulated trials. The major difference is that the experimentally acquired data required additional processing in the form of Wiener filters and bandpass filters to remove unwanted artifacts in the measured UWB reflections. Additionally, some upsampling and interpolation was also needed to compensate for the low sampling frequency of the P410.

Wiener Filter, Bandpass Filter, and Upsampling

The Wiener filter is used to remove large unwanted artifacts near the beginning of the waveform. Next, a bandpass filter with a pass frequency of 3.1 GHz to 5.3 GHz, the specified frequency of the P410's transmitted pulse to remove any unwanted frequencies that the receiver measured. Then an upsampling and interpolation filter is used to compensate for the low sampling frequency of the P410. DAS beamforming is performed as designed for the simulation trials.

3.3.3 Image Processing and Analysis

The Image Processing and Analysis module for the experimental trials is identical to the Image Processing and Analysis module for the simulation trials.

Chapter 4

Implementation of Simulated Trials Methodology

This chapter describes the low level implementation details needed for the imaging system. Section 4.1 covers the derivation of the finite-difference time-domain method for the simulated Data Acquisition module. Section 4.2 covers the implementation and set-up of the finite-difference time-domain method for the potted root system under test. Section 4.3 deals with the design and implementation of the Data Processing module. Finally, Section 4.4 covers the design and implementation of the Image Processing and Analysis module.

4.1 Data Acquisition: Finite-difference Time-domain Method Formulation

This section covers the formulation of the FDTD method and uses Allen Taflove's *Computational Electrodynamics, the finite-difference time-domain method* [49] and online course notes for EE 5303 from the University of Texas [50] as reference material. The formulation and simulation methods have been slightly modified to fit the simulation requirements for the objective of this thesis.

4.1.1 Maxwell's Equations and Constitutive Equations

The finite-difference time-domain method will be used for modeling the electrodynamics of the system under test. The formulation of the method begins with the time-domain Maxwell's differential equations.

$$\nabla \cdot \mathbf{E} = \frac{\rho}{\epsilon_0} \tag{4.1}$$

$$\nabla \cdot \mathbf{B} = 0 \tag{4.2}$$

$$\nabla \times \mathbf{E} = -\frac{\partial \mathbf{B}}{\partial t} \tag{4.3}$$

$$\nabla \times \mathbf{B} = \mu_0(\mathbf{J} + \epsilon_0 \frac{\partial \mathbf{E}}{\partial t}) \tag{4.4}$$

where:

- $\mathbf{E}$ is the electric field intensity, $\frac{\text{V}}{\text{m}}$.
- ρ is the volume charge density, $\frac{\text{C}}{\text{m}^3}$.
- ϵ_0 is the permittivity of free space, $\approx 8.854 \times 10^{-12}$ $\frac{\text{F}}{\text{m}}$.
- $\mathbf{B}$ is the magnetic flux density, $\frac{\text{Wb}}{\text{m}}$.
- μ_0 is the permeability of free space, $= 4\pi \times 10^{-7}$ $\frac{\text{H}}{\text{m}}$.
- $\mathbf{J}$ is the electric current density, $\frac{\text{A}}{\text{m}}$.

Equations (4.1)-(4.4) describe how electromagnetic fields are produced in space. Next, the constitutive equations for electromagnetic materials are needed as follows:

$$\mathbf{D} = \epsilon_0 \epsilon_r \mathbf{E} \tag{4.5}$$

$$\mathbf{B} = \mu_0 \mu_r \mathbf{H} \tag{4.6}$$

where:

- $\mathbf{D}$ is the electric flux density, $\frac{\text{C}}{\text{m}^2}$.
- ϵ_r is the relative permittivity, unitless.
- $\mathbf{H}$ is the magnetic field intensity, $\frac{\text{A}}{\text{m}}$.
- μ_r is the relative permeability, unitless.

Equations (4.5) and (4.6) describe how electromagnetic fields interact with linear, non-dispersive, isotropic, and non-magnetic materials. Altogether, Equations (4.1)-(4.6) describe how waves propagate through various media and are the fundamental equations for the development of the finite-difference time-domain method.

We are not concerned with simulating a system that will contain any charges or current sources which allows the assumption $\rho = 0$ and $\mathbf{J} = 0$. Moreover, the system will contain only non-magnetic material which allows the assumption $\mu_r = 1$. These assumptions allow Equations (4.1), (4.4), and (4.6) to be simplified to:

$$\nabla \cdot \mathbf{E} = 0 \tag{4.7}$$

$$\nabla \times \mathbf{B} = \mu_0(\epsilon_0 \frac{\partial \mathbf{E}}{\partial t}) \tag{4.8}$$

$$\mathbf{B} = \mu_0 \mathbf{H} \tag{4.9}$$

Next the electric field intensity and the electric flux density is normalized to be:

$$\widetilde{\mathbf{E}} = \frac{1}{\eta_0}\mathbf{E} = \sqrt{\frac{\epsilon_0}{\mu_0}}\mathbf{E}$$

$$\widetilde{\mathbf{D}} = c_0\mathbf{D} = \frac{1}{\sqrt{\mu_0 \epsilon_0}}\mathbf{D}$$

where:

- $\widetilde{\mathbf{E}}$ is the normalized electric field intensity, $\frac{\mathrm{V}}{\mathrm{m}\Omega}$
- η_0 is the impedance of free space, $\approx 120\pi\ \Omega$.
- c_0 is the speed of light in free space, $\approx 299,792,458\ \frac{\mathrm{m}}{\mathrm{s}}$.

This simplifies Equation (4.5) to be:

$$\widetilde{\mathbf{D}} = \epsilon_r \widetilde{\mathbf{E}} \tag{4.10}$$

Which allows the curl Equations (4.3) and (4.8) (substituting (4.9) into (4.8)) to be written as:

$$\nabla \times \widetilde{\mathbf{E}} = -\frac{1}{c_0}\frac{\partial \mathbf{H}}{\partial t} \tag{4.11}$$

$$\nabla \times \mathbf{H} = \frac{1}{c_0}\frac{\partial \widetilde{\mathbf{D}}}{\partial t} \tag{4.12}$$

Note that Equation (4.10) is the only equation dependent on the relative permittivity and determines how the electromagnetic waves interacts with materials. This allows for easy modification of the simulations to accommodate more complex material properties as only the calculation of Equation (4.10) is affected. Equations (4.10), (4.11), and (4.12) are fundamental analytical equations for use in the finite-difference time-domain simulations using Yee's grid.

Table 4.1 summarizes the important equations for use in the FDTD simulations.

Table 4.1: Summary of derived analytical equations for use in FDTD simulations.

Equation	**Equation Description**	**Equation Number**
$\nabla \cdot \mathbf{E} = 0$	Gauss's law for charge-free materials. Divergence equation for electric fields.	(4.7)
$\nabla \cdot \mathbf{B} = 0$	Gauss's law for magnetism. Divergence equation for magnetic fields.	(4.2)
$\nabla \times \widetilde{\mathbf{E}} = -\frac{1}{c_0}\frac{\partial \mathbf{H}}{\partial t}$	Normalized Maxwell-Faraday's equation. Curl equation for electric fields.	(4.11)
$\nabla \times \mathbf{H} = \frac{1}{c_0}\frac{\partial \widetilde{\mathbf{D}}}{\partial t}$	Ampere's Circuital Law. Curl equation for magnetic fields.	(4.12)
$\widetilde{\mathbf{D}} = \epsilon_r \widetilde{\mathbf{E}}$	Normalized constitutive equation for electric fields.	(4.10)
$\mathbf{B} = \mu_0 \mathbf{H}$	Constitutive equation for magnetic fields in non-magnetic media.	(4.9)

4.1.2 Temporal Derivative Approximations

The FDTD uses a forward finite difference to approximate the time derivative which can be applied to Equation (4.11).

$$\nabla \times \widetilde{\mathbf{E}}(t) = -\frac{1}{c_0}\frac{\mathbf{H}(t + \Delta t/2) - \mathbf{H}(t - \Delta t/2)}{\Delta t} \tag{4.13}$$

where:

- Δt is the minimum time step of the simulation, s.

- t is the instant of time the simulation is currently calculating, s.

Similarly, a central finite difference is done for Equation (4.12).

$$\nabla \times \mathbf{H}(t + \Delta t/2) = \frac{1}{c_0} \frac{\widetilde{\mathbf{D}}(t + \Delta t) - \widetilde{\mathbf{D}}(t)}{\Delta t} \tag{4.14}$$

The normalized electric flux density $\widetilde{\mathbf{D}}$ (and also the electric field intensity $\widetilde{\mathbf{E}}$) exists at time 0, Δt, $2\Delta t$, ..., $(N-1)\Delta t$ where N is the number of time steps needed for the simulation. Note that the magnetic field intensity $\mathbf{H}$ (and also the magnetic flux density $\mathbf{B}$) is staggered and is defined to exist at $\Delta t/2$, $3\Delta t/2$, ... $(2N-1)\Delta t/2$. Also note that the difference approximations in Equations (4.13) ($\frac{\mathbf{H}(t+\Delta t/2) - \mathbf{H}(t-\Delta t/2)}{\Delta t}$) and (4.14) ($\frac{\widetilde{\mathbf{D}}(t+\Delta t) - \widetilde{\mathbf{D}}(t)}{\Delta t}$) exist at t and $t + \Delta t/2$ respectively.

4.1.3 Yee Lattice

At any point in free space, the electromagnetic field vectors can be described as $\mathbf{E} = E_x\hat{\mathbf{x}} + E_y\hat{\mathbf{y}} + E_z\hat{\mathbf{z}}$ and $\mathbf{H} = H_x\hat{\mathbf{x}} + H_y\hat{\mathbf{y}} + H_z\hat{\mathbf{z}}$. Normally, each of the vector components would coincide on the same point on the grid unit cell. A Yee Lattice is the staggering the field components to different positions within the unit cells of the simulation grid [51].

Figure 4.1 shows the locations of each of the field components in the unit grid cell [50]. The staggering of the field components naturally satisfies the divergence Equations (4.2) and (4.7) because all of the field components on the entire simulation grid form closed loops and so there is no divergence anywhere on the simulation grid. Additionally, it simplifies the calculating of the curl Equations (4.11) and (4.12).

4.1.4 Spatial Derivative Approximations

We need to define some notational quirks which arise from using a Yee lattice in our simulations before we can define the approximations for the spatial derivatives. The notation (i,j,k) refers to the voxel corresponding to the i$^{\text{th}}$, j$^{\text{th}}$, k$^{\text{th}}$ grid position in the simulation. Figure 4.2 shows an example of a 3x3x3 simulation grid containing a total of 27 voxels. We will denote $\widetilde{\mathbf{E}}|_{i,j,k} = \widetilde{E}_x|_{i,j,k}\hat{\mathbf{x}} + \widetilde{E}_y|_{i,j,k}\hat{\mathbf{y}} + \widetilde{E}_z|_{i,j,k}\hat{\mathbf{z}}$ to represent to normalized the electric field vector

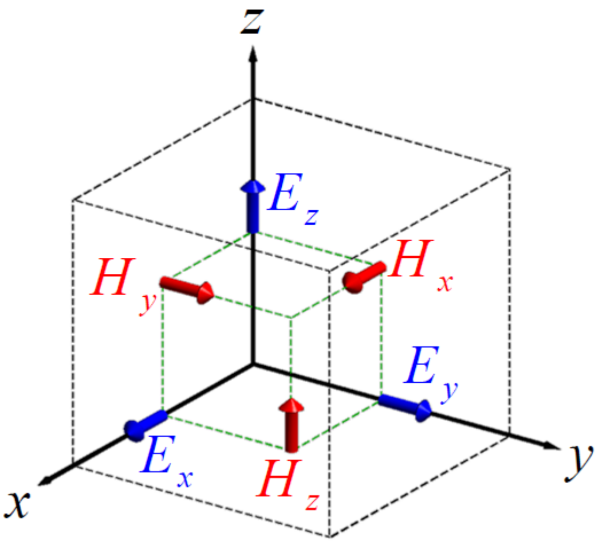

Figure 4.1: The location of the field vectors within a unit voxel.

located at voxel (i,j,k). Note that although the components $E_x|_{i,j,k}$, $E_y|_{i,j,k}$, and $E_z|_{i,j,k}$ are in the same voxel, they are staggered according to the Yee lattice configuration shown in Figure 4.1. Similarly, the magnetic field will be denoted $\mathbf{H}|_{i,j,k} = H_x|_{i,j,k}\hat{\mathbf{x}} + H_y|_{i,j,k}\hat{\mathbf{y}} + H_z|_{i,j,k}\hat{\mathbf{z}}$. Again, although the magnetic field components are in the same voxel, they are still staggered according to the Yee lattice.

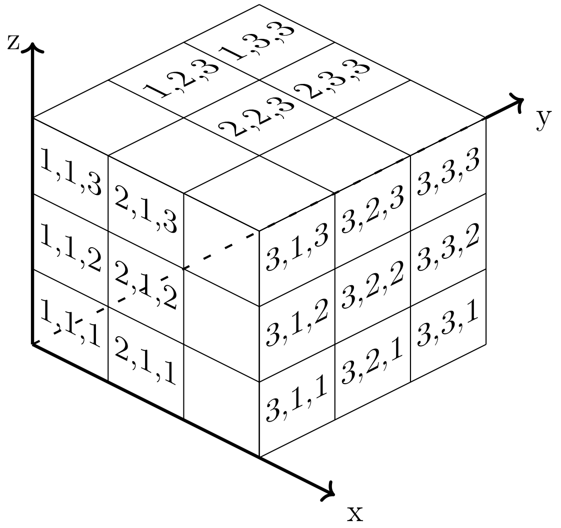

Figure 4.2: 3x3x3 simulation grid example illustrating the grid index notation.

To approximate the analytical Equations (4.11) and (4.12), we first need to expand the them. Assuming linear, non-dispersive, isotropic material, Equation (4.11) expands to three equations:

$$\frac{\partial \widetilde{E}_z}{\partial y} - \frac{\partial \widetilde{E}_y}{\partial z} = -\frac{1}{c_0}\frac{\partial H_x}{\partial t} \tag{4.15}$$
$$\frac{\partial \widetilde{E}_x}{\partial z} - \frac{\partial \widetilde{E}_z}{\partial x} = -\frac{1}{c_0}\frac{\partial H_y}{\partial t} \tag{4.16}$$
$$\frac{\partial \widetilde{E}_y}{\partial x} - \frac{\partial \widetilde{E}_x}{\partial y} = -\frac{1}{c_0}\frac{\partial H_z}{\partial t} \tag{4.17}$$

And Equation (4.12) expands to the three equations:

$$\frac{\partial H_z}{\partial y} - \frac{\partial H_y}{\partial z} = \frac{1}{c_0}\frac{\partial \widetilde{D}_x}{\partial t} \tag{4.18}$$
$$\frac{\partial H_x}{\partial z} - \frac{\partial H_z}{\partial x} = \frac{1}{c_0}\frac{\partial \widetilde{D}_y}{\partial t} \tag{4.19}$$
$$\frac{\partial H_y}{\partial x} - \frac{\partial H_x}{\partial y} = \frac{1}{c_0}\frac{\partial \widetilde{D}_z}{\partial t} \tag{4.20}$$

Note that all field components in Equations (4.15)-(4.20) are functions of time and space in Cartesian coordinates, but the function arguments are omitted for visual clarity.

The spatial derivatives of these equations will also be approximated using a forward and backward finite difference. With the spatial approximations we arrive at the following equations for the electric field:

$$\frac{\widetilde{E}_z|_{i,j+1,k}(t) - \widetilde{E}_z|_{i,j,k}(t)}{\Delta y} - \frac{\widetilde{E}_y|_{i,j,k+1}(t) - \widetilde{E}_y|_{i,j,k}(t)}{\Delta z} = -\frac{1}{c_0}\frac{\partial H_x}{\partial t} \tag{4.21}$$
$$\frac{\widetilde{E}_x|_{i,j,k+1}(t) - \widetilde{E}_x|_{i,j,k}(t)}{\Delta z} - \frac{\widetilde{E}_z|_{i+1,j,k}(t) - \widetilde{E}_z|_{i,j,k}(t)}{\Delta x} = -\frac{1}{c_0}\frac{\partial H_y}{\partial t} \tag{4.22}$$
$$\frac{\widetilde{E}_y|_{i+1,j,k}(t) - \widetilde{E}_y|_{i,j,k}(t)}{\Delta x} - \frac{\widetilde{E}_x|_{i,j+1,k}(t) - \widetilde{E}_x|_{i,j,k}(t)}{\Delta y} = -\frac{1}{c_0}\frac{\partial H_z}{\partial t} \tag{4.23}$$

And also the magnetic field:

$$\frac{H_z|_{i,j,k}(t+\Delta t/2) - H_z|_{i,j-1,k}(t+\Delta t/2)}{\Delta y} - \frac{H_y|_{i,j,k}(t+\Delta t/2) - H_y|_{i,j,k-1}(t+\Delta t/2)}{\Delta z} = \frac{1}{c_0}\frac{\partial \widetilde{D}_x}{\partial t} \tag{4.24}$$

$$\frac{H_x|_{i,j,k}(t+\Delta t/2) - H_x|_{i,j,k-1}(t+\Delta t/2)}{\Delta z} - \frac{H_z|_{i,j,k}(t+\Delta t/2) - H_z|_{i-1,j,k}(t+\Delta t/2)}{\Delta x} = \frac{1}{c_0}\frac{\partial \widetilde{D}_y}{\partial t} \tag{4.25}$$

$$\frac{H_y|_{i,j,k}(t+\Delta t/2) - H_y|_{i-1,j,k}(t+\Delta t/2)}{\Delta x} - \frac{H_x|_{i,j,k}(t+\Delta t/2) - H_x|_{i,j-1,k}(t+\Delta t/2)}{\Delta y} = \frac{1}{c_0}\frac{\partial \widetilde{D}_z}{\partial t} \tag{4.26}$$

The right-hand side of Equations (4.15)-(4.20) contain the time derivatives which were approximated with a central and forward finite differences in Section 4.1.2. Equations (4.10), (4.13), (4.14), and (4.21) to (4.26) are the essential equations for implementing a 3D FDTD for linear, non-dispersive, and isotropic material.

4.1.5 Implementation of a 2D FDTD

The 3D FDTD equations will be reduced to 2D in order to reduce the computational complexity of the simulations. Reduction to the 2D grid operates in the assumption that the z-axis completely uniform.

$$\frac{\partial}{\partial z} = 0$$

This allows us to simplify Equations (4.21),(4.22), (4.24), and (4.25) to:

$$\frac{\widetilde{E}_z|_{i,j+1}(t) - \widetilde{E}_z|_{i,j}(t)}{\Delta y} = -\frac{1}{c_0}\frac{\partial H_x(t)}{\partial t} \tag{4.27}$$

$$-\frac{\widetilde{E}_z|_{i+1,j}(t) - \widetilde{E}_z|_{i,j}(t)}{\Delta x} = -\frac{1}{c_0}\frac{\partial H_y(t)}{\partial t} \tag{4.28}$$

$$\frac{H_z|_{i,j}(t+\Delta t/2) - H_z|_{i,j-1}(t+\Delta t/2)}{\Delta y} = \frac{1}{c_0}\frac{\partial \widetilde{D}_x(t)}{\partial t} \tag{4.29}$$

$$-\frac{H_z|_{i,j}(t+\Delta t/2) - H_z|_{i-1,j}(t+\Delta t/2)}{\Delta x} = \frac{1}{c_0}\frac{\partial \widetilde{D}_y(t)}{\partial t} \tag{4.30}$$

Equations (4.27), (4.28), and (4.23) have now decoupled from Equations (4.29), (4.30), and (4.26). The former set of equations models the transverse electric polarization (TEz polarization) and the latter set of equations is the transverse magnetic polarization (TMz polarization). Generally, both sets of equations must be simulated, but since our materials will be isotropic, both sets will yield the same results because they are numerically the same. As such, only the TEz mode will be simulated to further reduce computational complexity.

We will also rearrange Equations (4.10), (4.13), and (4.14) to the following:

$$\widetilde{\mathbf{E}}(t) = \frac{1}{\epsilon_r}\widetilde{\mathbf{D}}(t) \tag{4.31}$$

$$\mathbf{H}(t+\Delta t/2) = (c_0\Delta t)(\nabla \times \widetilde{\mathbf{E}}(t)) + \mathbf{H}(t-\Delta t/2) \tag{4.32}$$

$$\widetilde{\mathbf{D}}(t+\Delta t) = (c_0\Delta T)(\nabla \times \mathbf{H}(t+\Delta t/2)) + \widetilde{\mathbf{D}}(t) \tag{4.33}$$

Equations (4.26), (4.27), (4.28), (4.31), (4.32), and (4.33) allow us to update the electric field, magnetic field, and electric flux density for use in the simulations. Figure 4.3 shows the flow of calculations for simulating the electric and magnetic fields for a 2D FDTD simulation in TEz polarization. This procedure allows us to simulate UWB frequencies interacting with the pot and root system and will provide the data needed to create the processing methods for the Data Processing and Image Processing and Analysis modules.

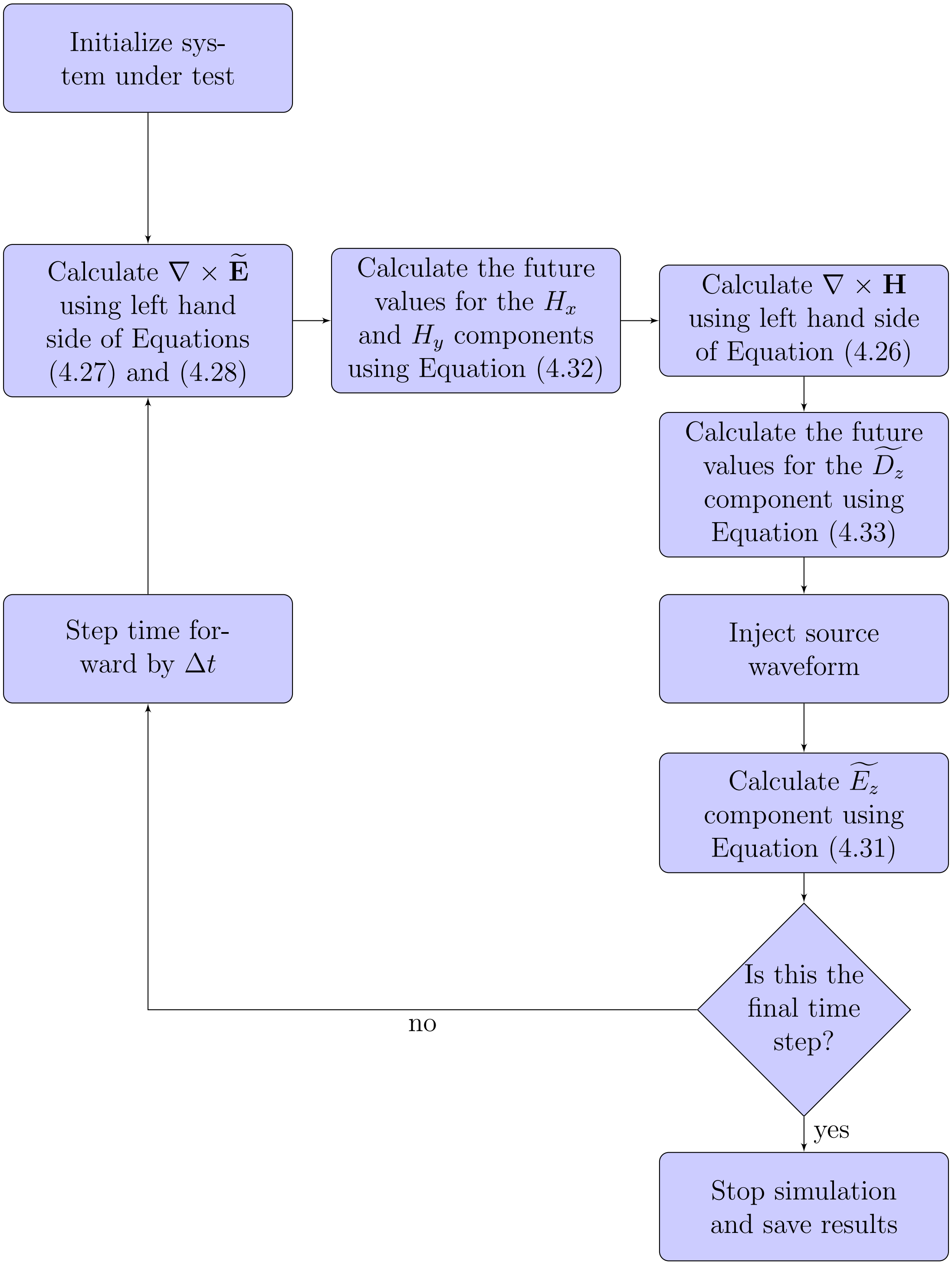

Figure 4.3: 2D-FDTD Program Flow Diagram

4.2 Data Acquisition: Simulation Implementation

This section covers the development and selection of important parameters for the implementation of the 2D FDTD algorithm and development of the system under test in MATLAB.

4.2.1 Courant Stability Condition

The Courant Stability condition limits the maximum duration the time step can be in simulations to ensure that the simulations accurately model the changing electric and magnetic fields on the simulation grid [49]. For simulation stability, the maximum time step must be small enough so that a wave propagating in free space (at c_0) must never travel further than the minimum grid resolution.

$$\Delta t \leq \frac{\Delta s}{c_0} F \tag{4.34}$$

where:

- Δs is the minimum grid resolution along any dimension of the simulation, m.
- F is a safety factor, $F \leq 1$ unitless.

A safety factor of $F = 0.5$ is selected for the simulations to ensure accuracy and stability of all simulations run. Generally, the minimum grid resolution was selected to be at least 0.0333 cm and could be smaller depending on the size of the smallest modeled feature in the simulations.

4.2.2 Ultra-wideband Gaussian Pulse Source

A Gaussian pulse waveform $g(t)$ is defined to be as:

$$g(t) = exp\big(- (\frac{t - t_0}{\tau})^2 \big) \tag{4.35}$$

where:

- t_0 is the time from 0 seconds to the peak of the pulse at baseband, s.

- τ is a parameter which determines the frequency range of the pulse, s.

We will select $\tau = 0.5/(2.2\times 10^9)$ s and $t_0 = 3\tau = 6.8\times 10^-10$ s to have a pulse with full width at half maximum of approximately 2.2 GHz and to shift the waveform so that the majority of the energy is present at $t \geq 0$ s. Equation (4.35) is then multiplied with a 4.3 GHz carrier to create a source waveform that contains frequencies of 3.1 GHz to 5.3 GHz.

$$g_{src}(t) = exp\Bigg(- \Bigg(\frac{t - 3\cdot 2.2\times 10^9}{2.2\times 10^9})^2\Bigg)\Bigg) \cdot \cos\left(2\pi \cdot 4.3\times 10^9 t\right) \tag{4.36}$$

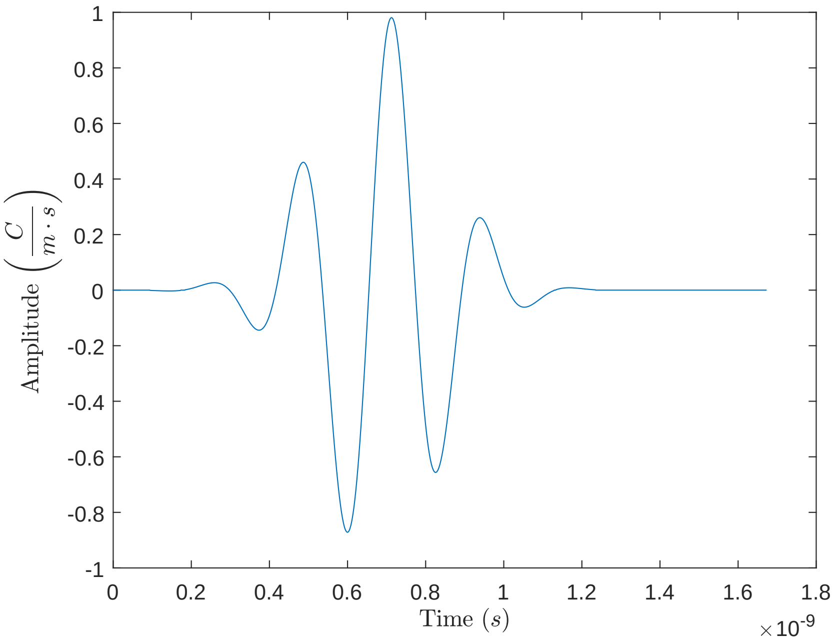

Figure 4.4: The 3.1 GHz - 5.3 GHz Gaussian pulse used as the source waveform for the simulations.

Equation (4.36) is shown in Figure 4.4. The frequency range of these simulations is selected to match the frequency of the PulsON P410 device [21].

4.2.3 Pot and Root Model

Physical Parameters

As shown in Figure 3.2 from Section 3.2.1, the distance from the surface of the soil to the bottom interior of the pot is a constant 40 cm while the distance from the left interior wall of the pot to the right interior wall of the pot is 25 cm. The pot wall width will be determined to minimize reflections at the carrier frequency for normal incidence. The optimal width for the pot is [52]:

$$D_{pot} = M \frac{c_0/f_c}{4\sqrt{\epsilon_{r,pot}\mu_{r,pot}}} \tag{4.37}$$

where:

- D_{pot} is the width of the pot wall to minimize reflections, m.
- M is an odd, positive integer, unitless.
- f_c is the frequency of the carrier, $\frac{1}{s}$.

The exact values used for Equation (4.37) varies depending on the chosen permittivity for the soil, and subsequently the permittivity of the pot. The parameter M is chosen so that the pot wall is chosen sufficiently wide to reflect typical pot wall widths.

The distance of the transceiver to the exterior pot wall will be dependent on the thickness of the pot wall with the following relation:

$$D_{trans} = 0.035 - D_{pot} \tag{4.38}$$

where:

- D_{trans} is the distance from the exterior pot wall to the transceiver, m.

The number of scans and the size of the root were varied to determine the limitations of the imaging system developed. The full results and analysis of these scans are discussed in Section 5.1 since an understanding of the Data Processing and Image Processing and Analysis Modules are needed for the discussion.

Electrical Parameters

The permittivity of the pot is designed to be:

$$\epsilon_{r,pot} = \sqrt{\epsilon_{r,soil}} \tag{4.39}$$

Designing the electrical parameters of the pot with Equation (4.39) along with the designed physical width from Equation (4.37) allows the pot to act as an antireflection coating [52] for the center frequency of the UWB Gaussian pulse. This will maximize the energy that is transmitted into the soil, thus resulting in more energy in the reflections off the root.

As briefly mentioned in Chapter 3, soil relative permittivity at high frequencies can be modeled in many ways, each with different results [46–48] and the accuracy of the models is highly dependent on soil characteristics such as soil composition and moisture content [46]. For the purposes of this project, a simple linear, isotropic, and non-dispersive model was used and was found to be sufficient to model experimental results. One important thing to keep in mind when choosing soil and root permittivity values is that it is ideal for DAS beamforming if the root relative permittivity is much different than the soil relative permittivity. A high permittivity contrast causes less energy to be transmitted and more energy to be reflected. Another important quality is to have the root permittivity be lower than the soil relative permittivity as this allows for total internal reflection to occur. Total internal reflection is where all of the incident energy with an incident angle past the critical angle is reflected [52]. Larger energy reflections off the root improves the signal to noise ratio of the received signals, and thus the quality of the images produced with DAS beamforming.

The importance of having a high permittivity contrast between soil and root becomes apparent when macroscopic reflective materials are added to the soil. These macroscopic materials vary in size and permittivity from the soil and represent portions of soil which slightly different compositions due to soil clumping, the presence of foreign objects, and the presence of varying water or air pockets. Again, the full results and analysis of these scans are discussed in a later section, Section 5.2, since an understanding of the Data Processing and Image Processing and Analysis Modules are needed for the discussion.

4.2.4 Data Acquisition Results

The simulations result in a reflected wave measured for one scan as shown in Figure 4.5. These reflections allow us to generate an energy mapping of the system under test showing where the most reflective materials are in the soil, and are the main output of the Data Acquisition Module. Note that Figure 4.5 has the y-axis scaled to show the amplitude of the reflections at 3 ns to 7 ns. The high amplitude measurements before 2 ns is the measurement of the source waveform.

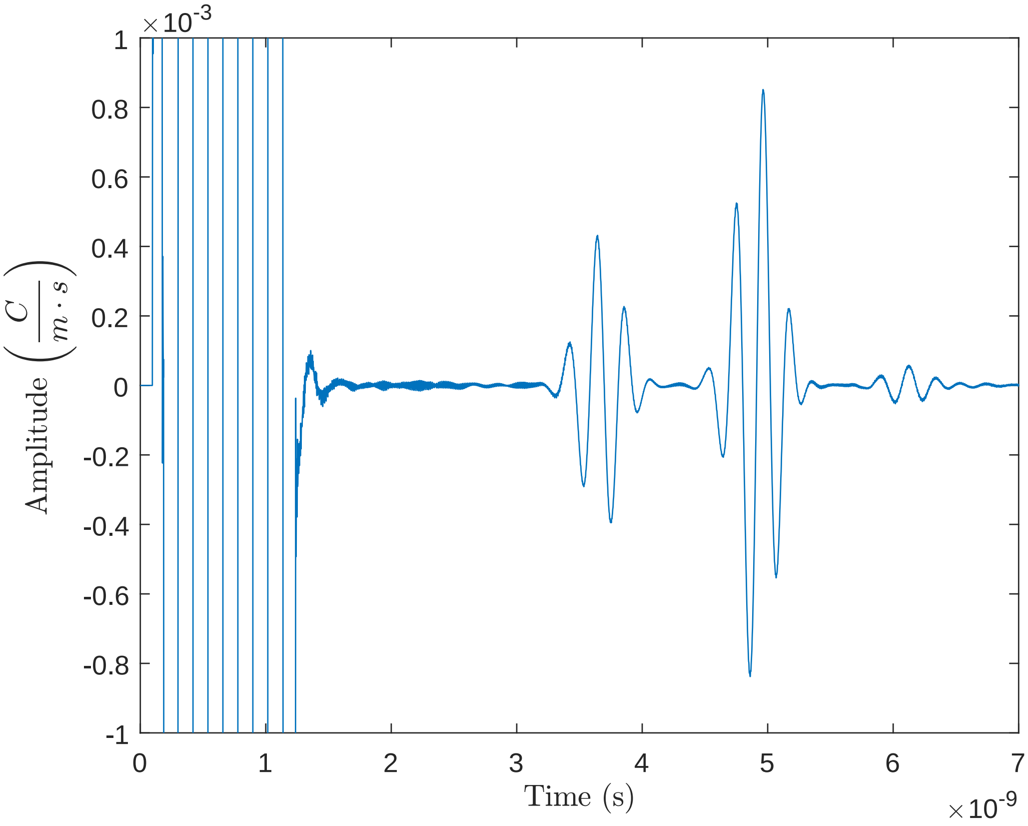

Figure 4.5: Example of a reflected waveform measured during one run of the simulations as shown.

We will define $b_i(t)$ to be the measured reflected waveform, where $i = 1, 2, \ldots, N$ and where N is the total number of scans. $b_1(t)$ refers to the waveform measured when the transceiver is positioned closest to the surface of the soil and $b_N(t)$ refers to the waveform measured when the transceiver is positioned closest to the bottom of soil.

4.3 Data Processing: Delay-and-sum Beamforming Methodology

The formulation of the delay-and-sum beamforming algorithm in this section uses Chapter 4.10 in the Handbook of Ultra-Wideband Short-Range Sensing Theory, Sensors, Applications as a reference [12]. Modifications are made to optimize the algorithm for maximizing the quality of the imaged potted roots.

One set of simulated scans described in the Data Acquisition Module produces a set of reflected waveforms $b_i(t)$. The peak energy occurrences in each waveform $b_i(t)$ correlate to approximate distances from transceiver to reflecting material. Delay-and-sum beamforming forms an image based on known physical and electrical parameters using $b_i(t)$.

4.3.1 Steering Vector Design

A steering vector $h_i^{(x_r,y_r)}(t)$ is defined and it is an impulse function with a time delay equal to the time it takes a wave to travel the most direct path from transceiver at the i^{th} scanning position to imaging point (x_r, y_r) and back to the transceiver. The distance the wave traveled is needed to calculate the appropriate time delay for $h_i^{(x_r,y_r)}(t)$.

Figure 4.6 shows the vectors $\mathbf{r_1}$, $\mathbf{r_2}$, and $\mathbf{r_3}$ which determines the most direct path that a wave can travel from transceiver to imaging point. The values $x_a, y_a, x_1, x_2, x_r, y_r, \epsilon_{r,pot}, \epsilon_{r,soil}$ are known and y_1, y_2 are not known. To determine the magnitudes of the vectors r_1, r_2, and r_3, we must first find y_1 and y_2. Using $n = \sqrt{(\mu_r \epsilon_r)}$ and Snell's law we can solve for y_1 and y_2. Figure 4.7 shows the geometries needed to solve the problem. The angles θ_1, θ_2, and θ_3 are related to the geometries.

$$\sin\theta_1 = \frac{|y_1 - y_a|}{|\mathbf{r_1}|} \tag{4.40}$$

$$\sin\theta_2 = \frac{|y_2 - y_1|}{|\mathbf{r_2}|} \tag{4.41}$$

$$\sin\theta_3 = \frac{|y_r - y_2|}{|\mathbf{r_3}|} \tag{4.42}$$

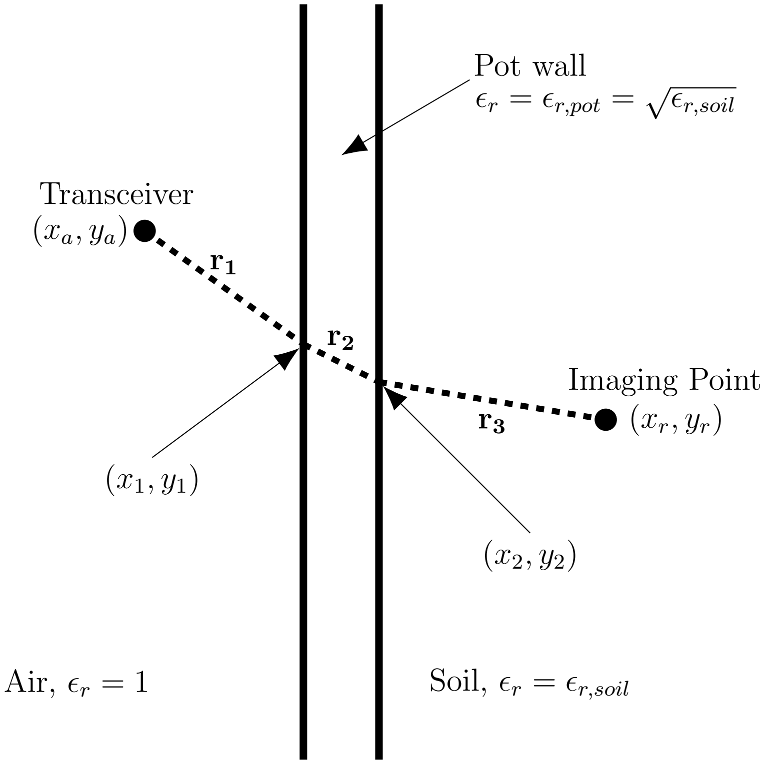

Figure 4.6: Most direct path from transceiver to imaging point to calculate for DAS beamforming.

Note that the absolute values on the distances for $y_1 - y_a$, $y_2 - y_1$, and $y_r - y_2$ are used to ensure the equations hold true no matter the vertical positioning of the transceiver and the imaging point. Additionally, the angles are related to each other using Snell's law.

$$\sin\theta_1\sqrt{\epsilon_{r,air}} = \sin\theta_2\sqrt{\epsilon_{r,pot}} \tag{4.43}$$

$$\sin\theta_2\sqrt{\epsilon_{r,pot}} = \sin\theta_3\sqrt{\epsilon_{r,soil}} \tag{4.44}$$

Substituting Equations (4.40), (4.41), and (4.42) into Equations (4.43) and (4.44) yields:

$$\frac{|y_1 - y_a|}{|\mathbf{r_1}|}\sqrt{\epsilon_{r,air}} = \frac{|y_2 - y_1|}{|\mathbf{r_2}|}\sqrt{\epsilon_{r,pot}} \tag{4.45}$$

$$\frac{|y_2 - y_1|}{|\mathbf{r_2}|}\sqrt{\epsilon_{r,pot}} = \frac{|y_r - y_2|}{|\mathbf{r_3}|}\sqrt{\epsilon_{r,soil}} \tag{4.46}$$

Substituting in the magnitudes of r_1, r_2, and r_3 in terms of their coordinates into Equations

(4.45) and (4.45) provides us with the final equations used for solving y_1 and y_2.

$$\frac{|y_1 - y_a|}{\sqrt{(x_1 - x_a)^2 + (y_1 - y_a)^2}}\sqrt{\epsilon_{r,air}} = \frac{|y_2 - y_1|}{\sqrt{(x_2 - x_1)^2 + (y_2 - y_1)^2}}\sqrt{\epsilon_{r,pot}} \tag{4.47}$$

$$\frac{|y_2 - y_1|}{\sqrt{(x_2 - x_1)^2 + (y_2 - y_1)^2}}\sqrt{\epsilon_{r,pot}} = \frac{|y_r - y_2|}{\sqrt{(x_r - x_2)^2 + (y_r - y_2)^2}}\sqrt{\epsilon_{r,soil}} \tag{4.48}$$

Equations (4.47) and (4.47) are difficult to solve analytically so and MATLAB's *fzero* function is used to solve for y_1 and y_2. The *fzero* function uses a combination of bisection, secant, and inverse quadratic interpolation methods to find the root of the input equations [53].

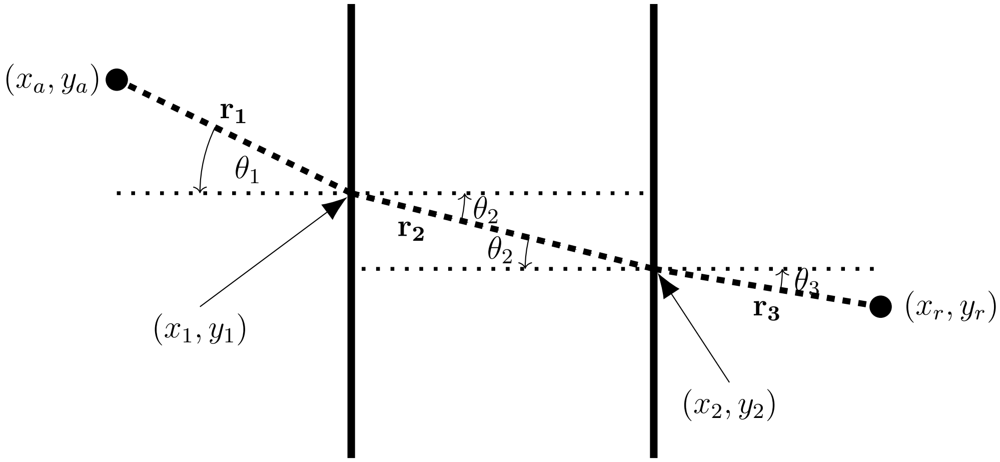

Figure 4.7: Angles and vectors needed to solve for y_1 and y_2 in Figure 4.6.

With known values for y_1 and y_2, numerical values are then calculated for $\mathbf{r_1}$, $\mathbf{r_2}$, and $\mathbf{r_3}$. The total time of flight T can then be calculated as:

$$T = 2 \cdot \left(\frac{|\mathbf{r_1}|}{c_0} + \frac{|\mathbf{r_2}|}{c_0}\sqrt{\epsilon_{r,pot}} + \frac{|\mathbf{r_3}|}{c_0}\sqrt{\epsilon_{r,soil}}\right) \tag{4.49}$$

Note that Equation (4.49) has a factor of 2 to account for the entire distance from transceiver, to imaging point, back to transceiver. The steering vector is then defined to be:

$$h_i^{(x_r,y_r)}(t) = \delta(t + t_0 + T) \tag{4.50}$$

where:

- $h_i^{(x_r,y_r)}(t)$ is the steering vector for the $\mathrm{i_{th}}$ scan at imaging point (x_r, y_r), unitless.
- t_0 is the time to the peak of the baseband UWB pulse as defined in Section 4.2.2, s.

Equation (4.50) is referred to as the steering vector and is essential to the performance of DAS beamforming. It is important to keep in mind that for every position (x_r, y_r) to be imaged there are N transceiver locations, each with their own steering vector.

4.3.2 Calculating Pixel Intensity and Creating an Image

A single transceiver waveform and one imaging point will be used for the purposes of explaining the calculation of pixel intensity. Figure 4.8 shows the selected wave path for the example. The set of scans used for this example has 12 scans, 35 cm depth, 3 cm average diameter, 20 soil relative permittivity, and 10 root relative permittivity.

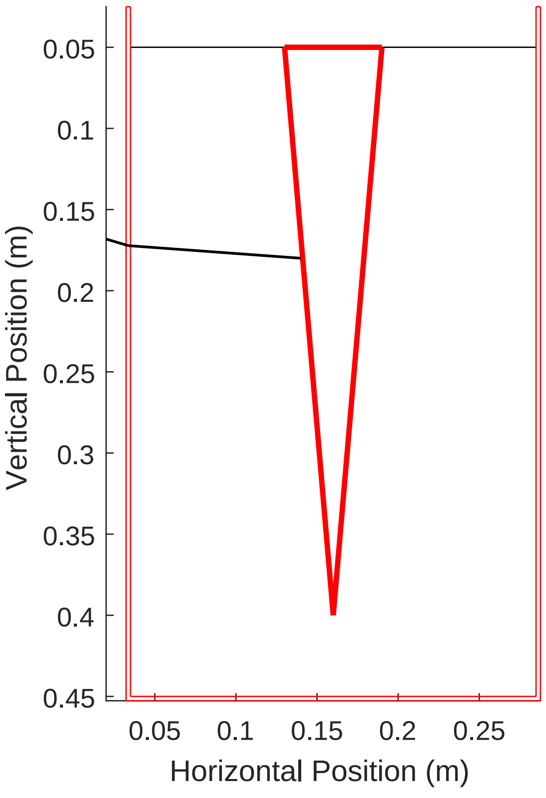

Figure 4.8: Scan position 4 and calculated ray for emitted UWB pulse, $\epsilon_{r,soil} = 20$ and $\epsilon_{r,root} = 10$.

In particular, we need to first determine the steering vector for $b_4(t)$ at the imaging point $(x_r, y_r) = (0.14, 0.18)$, ie. we are calculating $h_4^{(0.14,0.18)}(t)$. For scan position 4 at imaging point

(0,14,18) we use Equation (4.49) and (4.50) to calculate $h_4^{(0.14,0.18)}(t) \approx \delta(t + 5.44 \cdot 10^{-9})$. We can overlay the steering vector with the waveform by flipping the steering vector about $t = 0$ and plotting both. Figure 4.9 shows that the calculated steering vector lies within one of the measured reflections. This is logical because Figure 4.8 shows that the chosen imaging point, $(0.14, 0.18)$, is very close to the surface of the root which is causing high energy reflections.

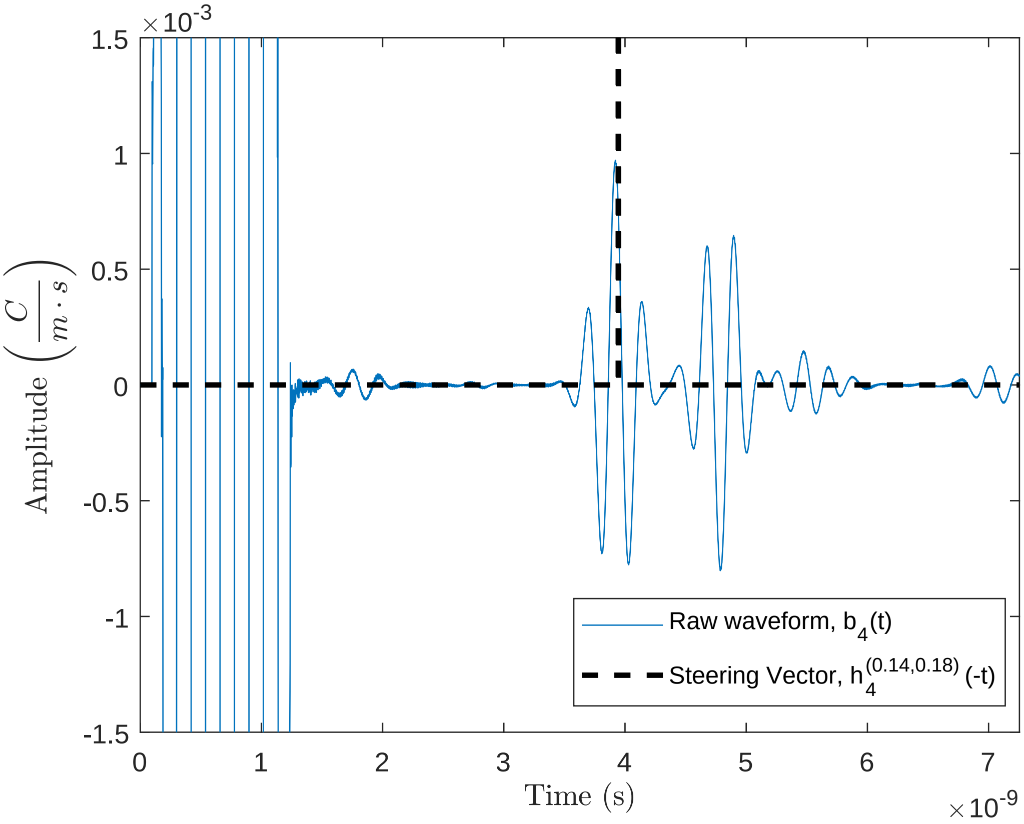

Figure 4.9: Raw waveform $b_4(t)$ and $h_4^{(0.14,0.18)}(-t)$, $\epsilon_{r,soil} = 20$ and $\epsilon_{r,root} = 10$.

We now define $z_4^{(0.14,0.18)}(t)$ to be the convolution of $h_4^{(0.14,0.18)}(t)$ and $b_4(t)$. More generally, this equation written as:

$$z_i^{(x_r,y_r)}(t) = h_i^{(x_r,y_r)}(t) * b_i(t) \tag{4.51}$$

where:

- $z_i^{(x_r,y_r)}(t)$ is the convolution of the steering vector and measured waveform for the i$^{\text{th}}$ scan at imaging point (x_r, y_r), $\frac{C}{m \cdot s}$.

$z_4^{(0.14,0.18)}(t)$ is a waveform which contains the marked portion of $b_4(t)$ in Figure 4.9 centered at $t = 0$. The energy for the signal is then calculated using:

$$I_i(x_r, y_r) = D_i(x_r, y_r) \int_{-W/2}^{W/2} z_i^{(x_r,y_r)} dt \tag{4.52}$$

where:

- $I_i(x_r, y_r)$ is the energy contribution from the i$^{\text{th}}$ scan at imaging point (x_r, y_r), $\frac{C^2}{m^2 \cdot s}$.
- $D_i(x_r, y_r)$ is a scalar weighting for the i$^{\text{th}}$ scan at imaging point (x_r, y_r), unitless.
- W is the window of time in of energy to be used for the image, s.

The weighting value $D_i(x_r, y_r)$ is a scalar value from 0 to 1. The value is determined by how close the position of the transceiver is to the imaging point. The closer the position, the closer the value of $D_i(x_r, y_r)$ is to 1 for that particular scan and imaging point. This places emphasis on the scans closer to the imaging point to reduce the effect of potential multipath issues. Essentially, emphasis is placed on the the positions with the shortest direct wave paths to the imaging point. Equation (4.53) is the equation used for determining all the values for $D_i(x_r, y_r)$.

$$D_i(x_r, y_r) = 1 - \left| \frac{y_i - y_r}{max(\mathbf{y_{1,2,\ldots,N}} - y_r)} \right| \tag{4.53}$$

where:

- y_i is the vertical coordinate of the i$^{\text{th}}$, m.
- $\mathbf{y_{1,2,\ldots,N}}$ is the vector containing all the vertical scanning positions, m.

Since we are dealing with a finite length pulse, we choose a window size of approximately 0.23 ns, which corresponds to approximately one period of the 4.2 GHz carrier frequency. The signal $z_4^{(0.14,0.18)}(t)$ plotted from $t = -W/2$ to $t = W/2$ is shown in Figure 4.10. The length of W is a very important parameter and analysis of adjustment of W is done in Section 5.3. W is referred to as the window size.

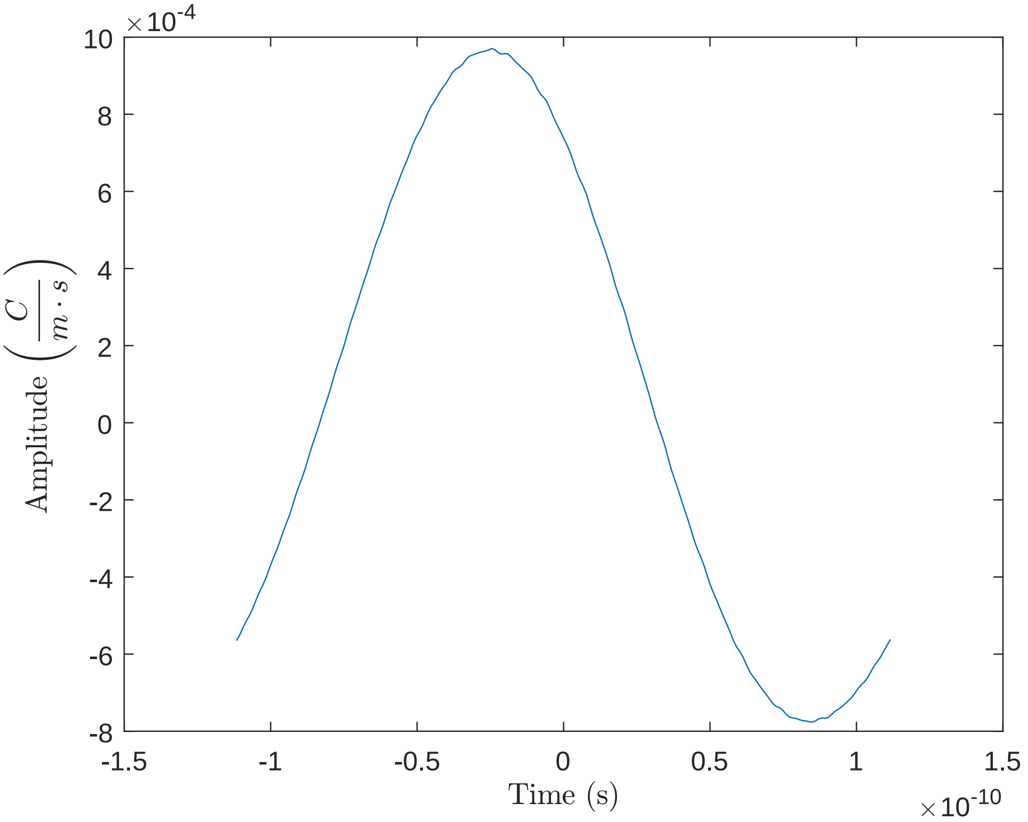

Figure 4.10: $z_i^{(x_r,y_r)}(t)$ plotted from $t = -W/2$ to $t = W/2$, $\epsilon_{r,soil} = 20$ and $\epsilon_{r,root} = 10$.

Equation (4.52) for $i = 4$ and $(x_r, y_r) = (0.14, 0.18)$ evaluates to $7.34 \cdot 10^{-9}$. This value is the energy contribution of the 4^{th} scan for the pixel at $(0.14, 0.18)$.

The process consisting of calculating is repeated for all scan positions. The pixel intensity for imaging point (x_r, y_r) for the final image is given by summing all the contributions of each scan.

$$I(x_r, y_r) = \sum_{i=1}^{N} I_i(x_r, y_r) \tag{4.54}$$

If x_r and y_r in Equation (4.54) are instead a set of vectors $\mathbf{x_r}$ and $\mathbf{y_r}$ corresponding to a spatial grid, then $I(\mathbf{x_r}, \mathbf{y_r})$ is rewritten as a matrix $\mathbf{I}(x, y)$ and is the unprocessed DAS beamforming image for this particular set of scans. Careful selection of vectors $\mathbf{x_r}$ and $\mathbf{y_r}$ is designed to exploit known knowledge of the root to reduce noise in the image and to reduce the time it takes to create an image. For example, if it is physically observed that the stem of the canola plant right at the surface of the soil exists at 3 cm from the pot, then it is likely that the root should be around 3 cm from the pot. $\mathbf{x_r}$ and $\mathbf{y_r}$ can be selected so that it images the region around 3 cm from the pot wall in this case, ignoring regions that may be too far from the stem location of the plant.

4.3.3 Simplifying Steering Vector Calculations

The values of y_1 and y_2 in Equations (4.47) and (4.48) need to be solved potentially thousands of times, significantly slowing the DAS beamforming algorithm. The problem is simplified by assuming that only one ray refraction occurs at the pot wall, as shown in Figure 4.11.

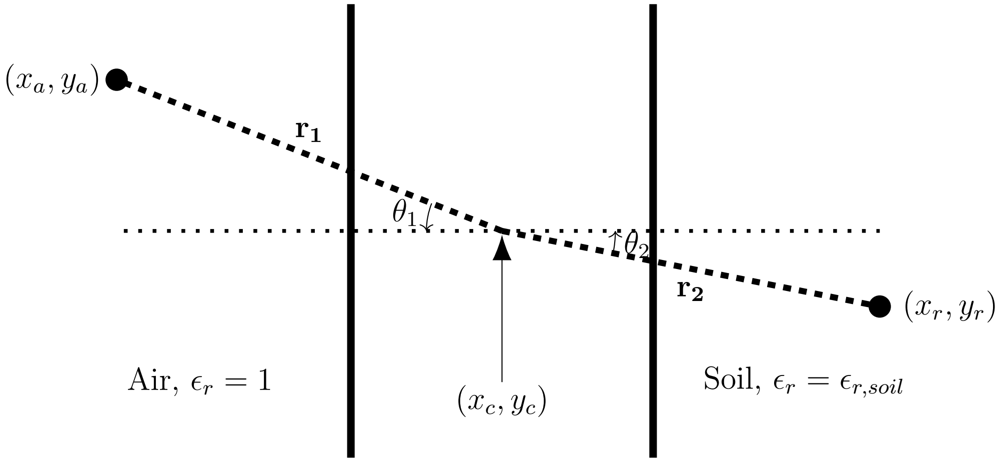

Figure 4.11: Angles and vectors needed to solve for y_c in the simplified refraction model.

Only the relative permittivity of the air and the soil will be used as an imaginary air-soil interface is assumed at the center of the pot wall. To calculate the ray paths we only need to solve y_c, as opposed to needing to solve for two vertical coordinates previously. Finding y_c is done using the same method and equations as Section 4.3.1. The geometries in Figure 4.11 and also Snell's law allows us to write:

$$\sin\theta_1 = \frac{|y_a - y_c|}{|\mathbf{r_1}|} \tag{4.55}$$

$$\sin\theta_2 = \frac{|y_c - y_a|}{|\mathbf{r_2}|} \tag{4.56}$$

$$\sin\theta_1\sqrt{\epsilon_{r,air}} = \sin\theta_2\sqrt{\epsilon_{r,pot}} \tag{4.57}$$

Substituting Equations (4.55) and (4.56) into (4.57) gives us the Equation (4.58).

$$\frac{|y_a - y_c|}{\sqrt{(x_a - x_c)^2 + (y_a - y_c)^2}}\sqrt{\epsilon_{r,air}} = \frac{|y_c - y_r|}{\sqrt{(x_c - x_r)^2 + (y_c - y_r)^2}}\sqrt{\epsilon_{r,soil}} \tag{4.58}$$

This simplification is still difficult to solve analytically, but it considerably speeds up the DAS beamforming algorithm since it only requires MATLAB's *fzero* function to find one root. This simplification significantly reduces the processing time required to create a DAS beamforming image and has negligible effects on the results as shown in Section 5.3.

4.3.4 Data Processing: Results

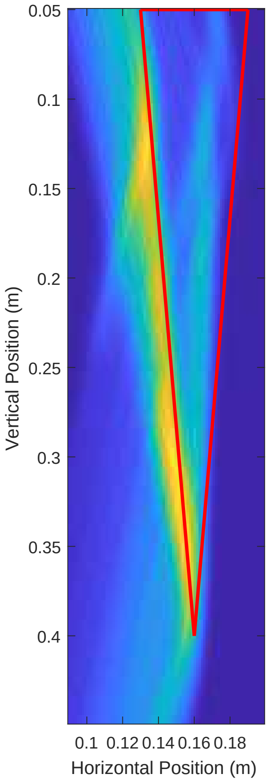

Figure 4.12: Unprocessed DAS beamforming image, $I(x_r, y_r)$ for 12 scanning positions as determined using method outlined in Section 4.3.2.

The primary purpose of the Data Processing Module is to produce a spatial 2D image as defined by $\mathbf{I}(x, y)$. The image should contain enough information on the energy distribution of the contents of the pot to be able to measure the surface location of the root. Figure 4.12 shows the final result of the image calculated from Section 4.3.2. Note that the thick line outlining the root is the actual location of the root, and is not a part of $\mathbf{I}(x, y)$.

$\mathbf{I}(x, y)$ is used in the Image Processing and Analysis Module to improve the quality of the image and measure important root characteristics such as depth and average diameter.

4.4 Image Processing and Analysis: Methodology

This section covers the image processing methods used to isolate the location of the root surface in the images produced by the Data Processing module. It is important to note that these methods are created assuming the actual location and size of the root is unknown. Creating this module in an unsupervised fashion will help in adapting the system to the experimental trials where information on a live root is unavailable. This section makes heavy use of MATLAB's Image Processing Toolbox [53].

4.4.1 Energy Histograms

An important used for analyzing and improving the quality of $\mathbf{I}(x, y)$ are the energy histograms and cumulative energy histograms. In particular, the cumulative energy histogram allows us to analyze the energy distribution of the image and remove unnecessary information.

The development of energy histograms starts with more conventional image histograms. First, $\mathbf{I}(x, y)$ is normalized to contain values ranging from 0-255, which is standard for 8-bit grayscale images. It is important to note that the values are not rounded to prevent loss in precision during processing and analysis. The image histogram of $\mathbf{I}(x, y)$ divides the pixel values into bins from 0-255 and places all the pixels in the image into the bin corresponding to each pixel's intensity.

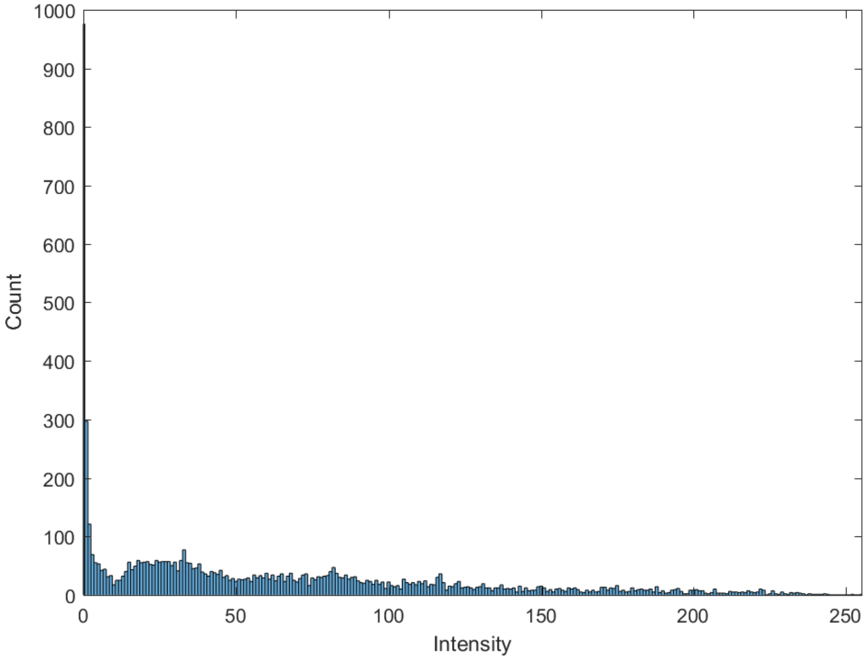

Figure 4.13: Image histogram for $\mathbf{I}(x, y)$ shown in Figure 4.12.

Figure 4.13 shows the image histogram for the unprocessed DAS beamforming image

$\mathbf{I}(x,y)$ created from the Data Processing Module. Note that most of the pixels are concentrated at around a 0 pixel intensity, with almost 1000 pixels around that value. This is logical since most of the energy in $\mathbf{I}(x,y)$ is very concentrated around the area of the root. The energy contribution of each bin is calculated by multiplying the bin value with the number of pixels in that particular bin. Plotting the energy contribution of each bin will be defined as the energy histogram and the energy histogram effectively maps how much energy is present at individual pixels relative to the energy in the entire image.

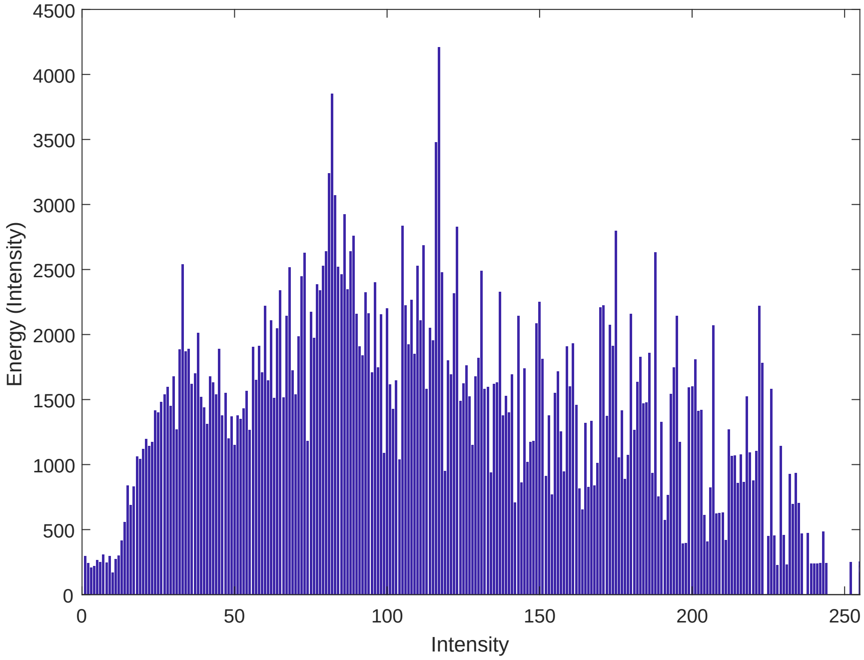

Figure 4.14: Energy histogram for $\mathbf{I}(x,y)$ shown in Figure 4.12.

Figure 4.14 shows the energy histogram for the same root and Figure 4.15 shows the cumulative energy histogram. This energy histogram allows for us quantitatively analyze the amount clutter present in the beamformed images. The dashed line at pixel intensity 111 is the 50% threshold intensity. Pixel intensities below 111 consist of 50% of the image's total energy. Generally, the 50% threshold intensity is fairly large (≥ 100) for a root image with low clutter.

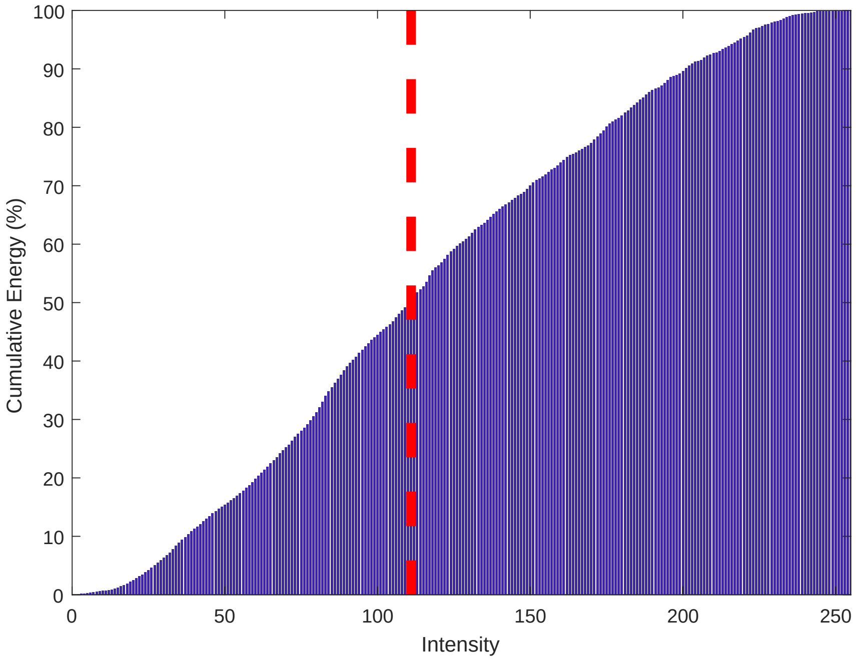

Figure 4.15: Cumulative energy histogram for $\mathbf{I}(x, y)$ shown in Figure 4.12.

4.4.2 Morphological Transformations

The primary image processing technique used to improve the image quality of the unprocessed DAS beamforming images is a modified white top-hat transform. A normal white top-hat transforms take a structuring element and performs a series of morphological transformations with the element to the desired image. The modified white top-hat transform does a similar series of morphological transformations. A structuring element is a 2D vector containing a shape that determines the size of details to retain. Equation (4.59) shows the operations needed to perform the modified white top-hat transformation.

$$\mathbf{T}(x, y) = \mathbf{I}(x, y) + ((\mathbf{I}(x, y) \ominus \mathbf{b}) \oplus \mathbf{c}) \tag{4.59}$$

where:

- $\mathbf{T}(x, y)$ is the modified white top-hat transformed image.
- $\mathbf{b}$ is the first selected structuring element.
- $\mathbf{c}$ is the second selected structuring element.

- $\ominus$ is the erosion operator.
- $\oplus$ is the dilation operator.

First, an erosion on $\mathbf{I}(x, y)$ is performed which removes bright artifacts that are smaller than the chosen size of $\mathbf{b}$. Consequently, this also removes the edges of larger high intensity regions. A dilation is performed using $\mathbf{c}$ to restore the edges of the larger high intensity regions. The result of $((\mathbf{I}(x, y) \ominus \mathbf{b}) \oplus \mathbf{c})$ is an image with small artifacts removed and larger high intensity regions emphasized. The final image $\mathbf{T}(x, y)$ becomes an image with the larger, high intensity regions emphasized over smaller, lower intensity regions. Optimal design of structural elements $\mathbf{b}$ and $\mathbf{c}$ varies dependent on the characteristics of $\mathbf{I}(x, y)$ and are critical to the performance of the analysis system and are analyzed in Section 5.5.

4.4.3 Image Quantization, Erosion, and Interpolation

The cumulative energy histogram of $\mathbf{T}(x, y)$ is analyzed and a binary mask is made by retaining only the pixel intensities above a specified threshold intensity, which is related to a percentage of energy to retain in the image. This is done to analyze and process the potential location of the root based on size and shape alone. Creating a binary mask helps remove high energy noise which may compete with the energy of the reflections off the surface of the root.

The optimal threshold intensity is an essential parameter that is dependent on the characteristics of $\mathbf{T}(x, y)$ and is analyzed in Section 5.6. All pixels that are below the threshold intensity are assigned a binary '0'. All pixels that are above the threshold intensity are assigned a binary '1'. A binary erosion transformation is done to remove unwanted smaller artifacts at the edges of the root surface. The largest area has half of its pixels removed, starting from the side closest to the pot to the center of the binary area. The remaining image is then interpolated to the center of the pot. The final binary image has its area measured. The height is measured by collapsing the columns with a bitwise 'or' operation and then summing the remaining pixels. The average diameter is calculated by dividing the measured area by the measured height and then multiplying by 2. The multiplication by 2 is needed because each image only provides information from the surface of the root to the center of the pot. Since the root is simulated to be aligned with the center of the pot, the calculated area of the root is only half of the total root area.

Chapter 5

Simulation Results

This chapter covers the results and analysis of important variables and parameters in the simulated trial results. Section 5.1 covers the results, analysis, and limitations of the physical parameters of the simulated trials. Section 5.2 covers the results and the significance of the electrical parameters used in the simulated trials and why a high root and soil relative permittivity contrast is necessary. Section 5.3 examines the simplification of the steering vector calculations to reduce image formation time while retaining image quality. Section 5.4 summarizes the effect of choosing an appropriate window size for the DAS beamforming algorithm. Section 5.5 analyzes the importance of selecting appropriate structuring element sizes for the morphological transformations. Finally, Section 5.6 covers how the threshold used for quantization is dependent on the quality of the image produced.

5.1 Physical Parameter Analysis

A fairly large taproot with a 35 cm depth and 3 cm average diameter will be scanned. The size of this taproot is approximately the size of fully grown canola roots [54]. The vertical scanning position begins at a depth of 2 cm from the surface and ends at 41 cm (which is 2 cm from the bottom of the pot). 21, 12, and 6 equally spaced scans were used and the unprocessed DAS beamforming results are shown in Figure 5.1. Each scan consists of running the simulations and injecting the 3.1 GHz to 5.3 GHz source waveform at the current transceiver location and subsequently measuring the reflected energy at the transceiver location. These simulations were run with a high permittivity contrast between soil ($\epsilon_{r,soil} = 20$) and root ($\epsilon_{r,root} = 10$) and no noise to maximize desired reflected energy.

Initially, qualitative observations of the unprocessed DAS beamforming images were the primary metric for developing a basic work flow for the system modules. The root depth and average root diameter measurements were done after processing once the Data Acquisition and Data Processing Modules were finished. The measurement results are summarized on Table 5.1. These measurements are made by keeping 35% of the energy for all scans and a structuring element of size 2 cm diameter for the modified top-hat transformations and 1 mm diameter for the mask erosion.

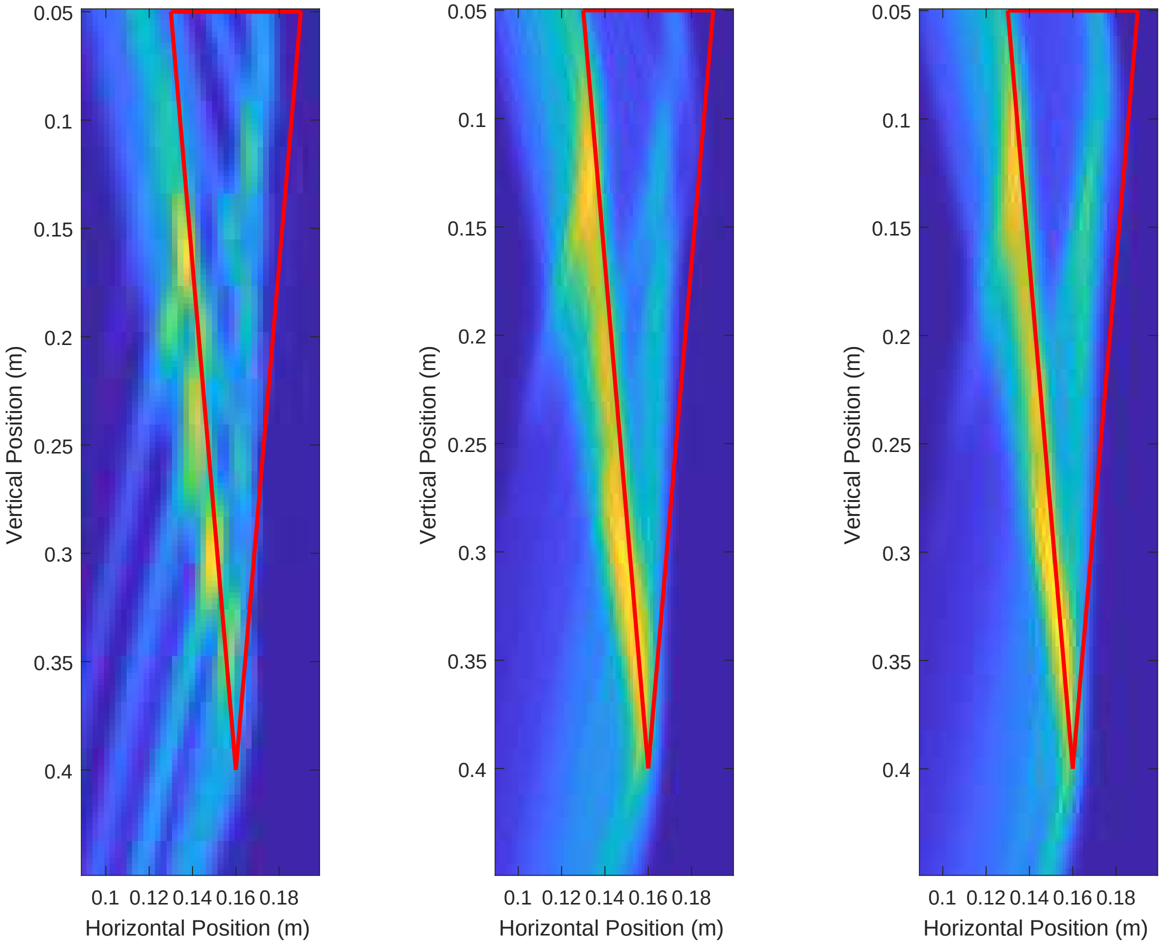

(a) 6 scans. **(b)** 12 scans. **(c)** 21 scans.

Figure 5.1: Unprocessed DAS beamforming images for (a) 6 scanning positions, (b) 12 scanning positions, and (c) 21 scanning positions.

Figure 5.1a shows that 6 scans has very distinct artifacts not present in Figure 5.1b and Figure 5.1c for 12 scans and 21 scans respectively. Judging qualitatively from the results in Figure 5.1, 12 scans performs quite similarly to 21 scans while taking effectively half the

Table 5.1: Measured root depths and root average diameters for images produced by varying the number of scanning positions.

Number of Scans	Measured Root Depth (cm)	Error in Depth Measurement (cm)	Average Measured Root Average Diameter (cm)	Error in Average Diameter Measurement (cm)
6	30.25	-5.75	3.85	+0.85
12	36.14	+1.14	3.14	+0.14
21	34.69	-0.31	3.29	+0.29

time to simulate and process. Table 5.1 confirms the qualitative analysis with quantitative measurements.

Note that the thick lines in Figure 5.1 indicate the actual position of the root. It is important to note that it is not the number of scans that is important, but the size of the spacing between the scans. In this case, we are dealing with a constant vertical scanning range so the spacing is only a function of the number of scans.

Next, with 12 scans per root, the size of the root was varied to determine how the root size will affect the imaging results. The full results and analysis are in Section 5.1. Table 5.2 summarizes the sizes simulated and the errors in measurements. These measurements are made by keeping 35% of the energy for all scans and a structuring element of size 2 cm diameter for the modified top-hat transformation and 2 mm diameter for the mask erosion.

Table 5.2: Root depths and average root diameters of model to be simulated and imaged.

Root Test Number	Root Depth (cm)	Percent Error in Depth Measurement (%)	Average Root Diameter (cm)	Percent Error in Average Diameter Measurement (%)
1	25.00	4.3	2.00	15.6
2	15.00	13.5	1.50	26.4
3	10.00	30.4	1.50	18.7
4	5.00	112.8	1.00	37.5

Table 5.2 shows increasing errors as the root sizes become smaller. In particular, Root Test Number 3 and 4 have very large percent errors with 30.4% and 112.8%, respectively.

Examining the unprocessed images in Figure 5.2 shows that there is a large amount of energy from that back side of the root (the side furthest from the transceiver), causing wave interference with the front side reflections and erroneous detection of the front side location. The unsupervised data and image processing methods used for measurements are unable to determine the location of the front surface of the root, causing large measurement errors which make the measured depth and diameter unreliable metrics. Moreover, the unprocessed images show that since the smaller size of the roots causes most of the energy concentrated around the tip of the root, further creating more erroneous results.

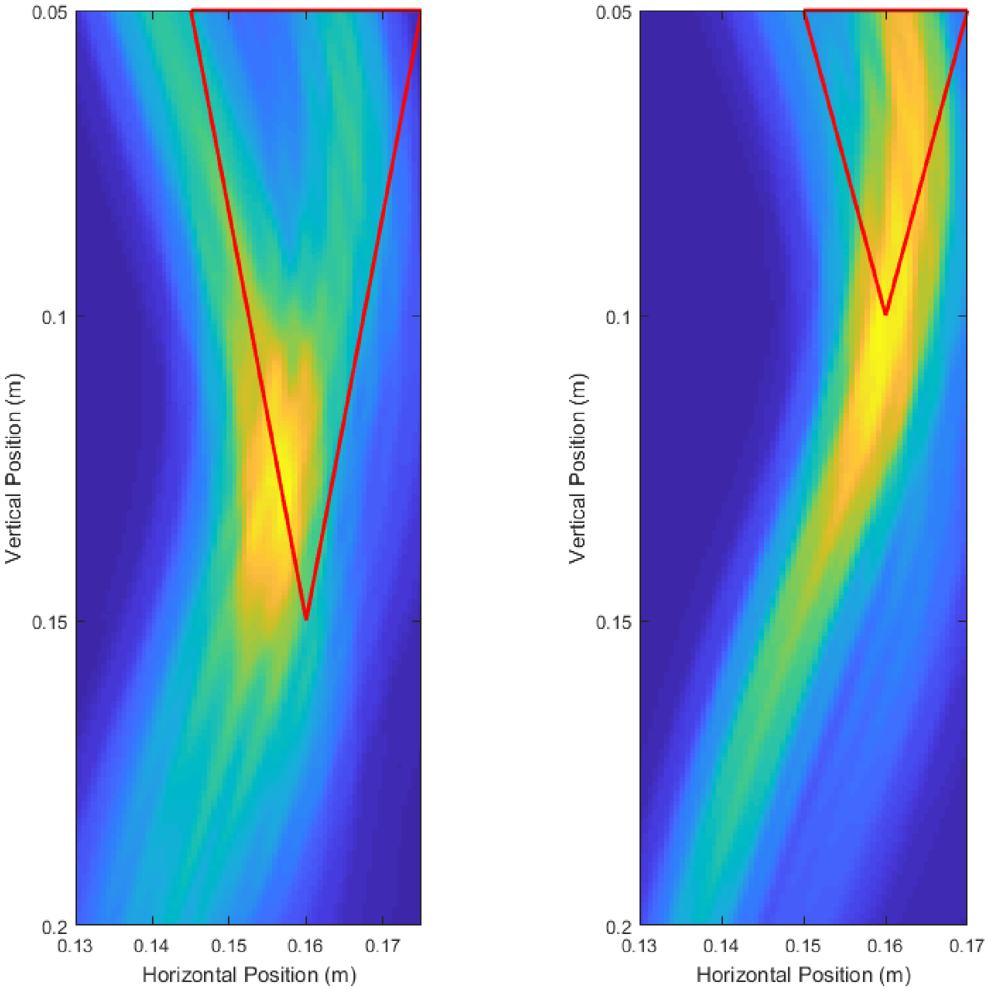

(a) Root Test Number 3.

(b) Root Test Number 4.

Figure 5.2: Unprocessed DAS beamforming images for a root with (a) 10.00 cm depth and 1.50 cm average diameter and (b) 5.00 cm depth and 1.00 cm average diameter.

In efforts to improve the unprocessed image quality, the scanning area is reduced from a range of 2 cm to 41 cm. For Root Test Number 3, the range becomes 2 cm to 17 cm. For Root Test number 4, the range becomes 2 cm to 10 cm. This effectively decreases the scan spacing from 3.36 cm to 1.33 cm for Root Test Number 3, and 3.36 cm to 0.75 cm for Root Test Number 4. Figure 5.3 shows the unprocessed images produced.

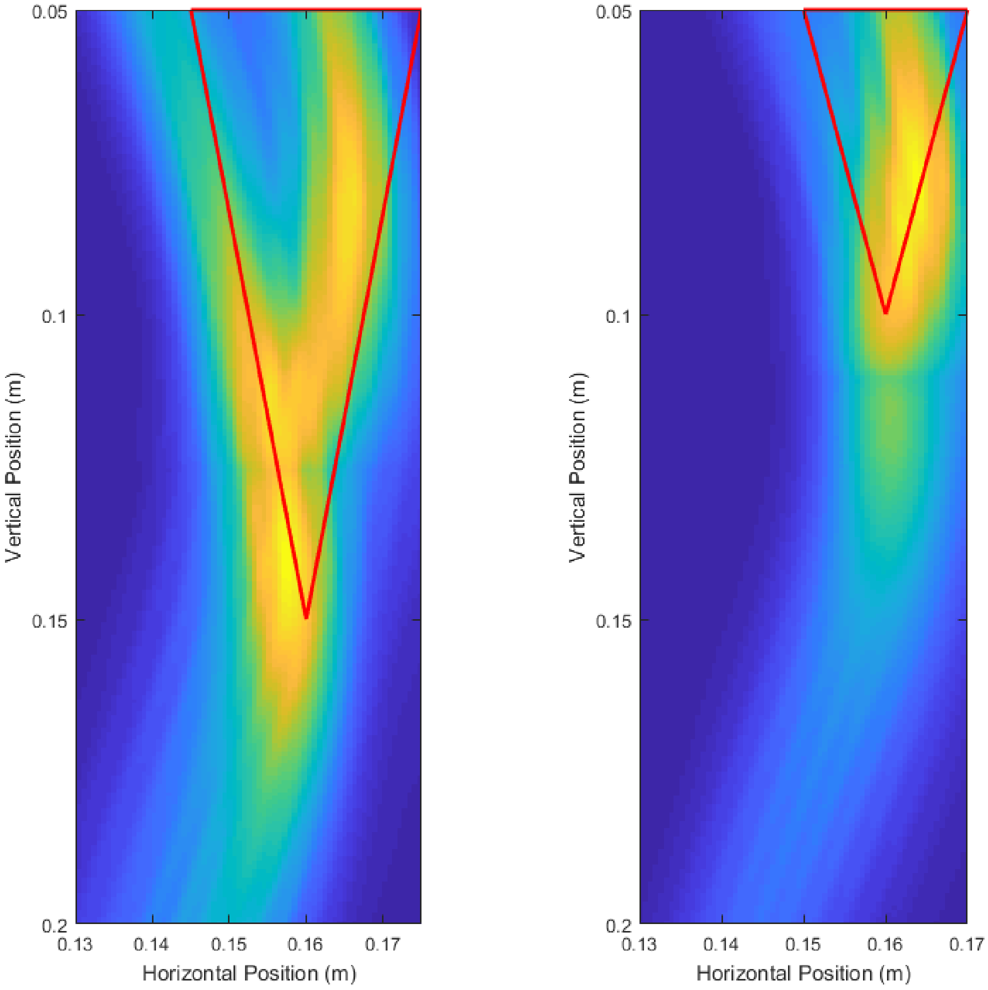

(a) Shortened scan range Root Test Number 3.

(b) Shortened scan range Root Test Number 4.

Figure 5.3: Unprocessed DAS beamforming images with a shortened scan range for a root with (a) 10.00 cm depth and 1.50 cm average diameter and (b) 5.00 cm depth and 1.00 cm average diameter.

Figure 5.3 shows some improvement in the quality of the image. The surface of the root is still poorly detected but the energy is slightly better concentrated around the location of the root. These root sizes show the limitation of the current UWB imaging system for imaging smaller roots.

5.2 Electrical Parameter Analysis

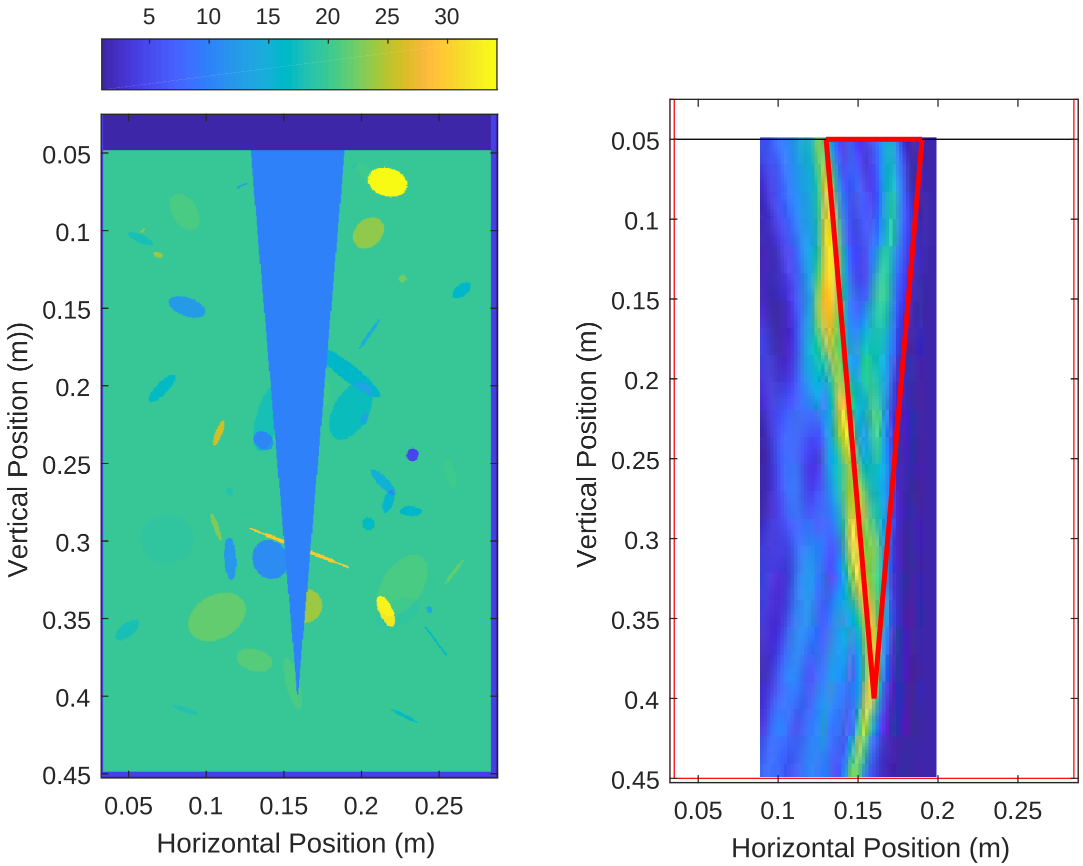

(a) The relative permittivity distribution of Root Test Number 5.

(b) The unprocessed DAS beamforming image for Root Test Number 5.

Figure 5.4: The unprocessed DAS beamforming image for a root with $\epsilon_r = 10$.

12 equally spaced scans were done on a 35 cm deep root with an average diameter of 3 cm. Macroscopic scattering objects were added to the soil each with randomly generated sizes and permittivities to demonstrate the importance of having a high root to soil relative permittivity contrast. The permittivity values selected are summarized on Table 5.3. For Root Test Number 6, the relative permittivity contrast between the macroscopic scatterers and soil is large when compared to the contrast between root and soil to demonstrate the effects of a low root to soil contrasat. These measurements are made by keeping 50% of the energy for all scans and a structuring element of size 2 cm diameter for the modified top-hat transformation and 1 mm diameter for the mask erosion.

Table 5.3: Root and soil relative permittivity of model to be simulated and imaged.

Root Test Number	Root Relative Permittivity	Soil Relative Permittivity
5	10	20
6	18	20

Figure 5.4 shows that the introduction of macroscopic scattering objects slightly degrades the quality of the image when compared to Figure 5.1b, which was imaged using the same simulation parameters but without the macroscopic scattering objects. There are more artifacts around the surface of the root as well as at the bottom tip of the root in Figure 5.4b. The quality overall, however, is still quite good as the majority of the energy in the image is concentrated around the front surface of the root.

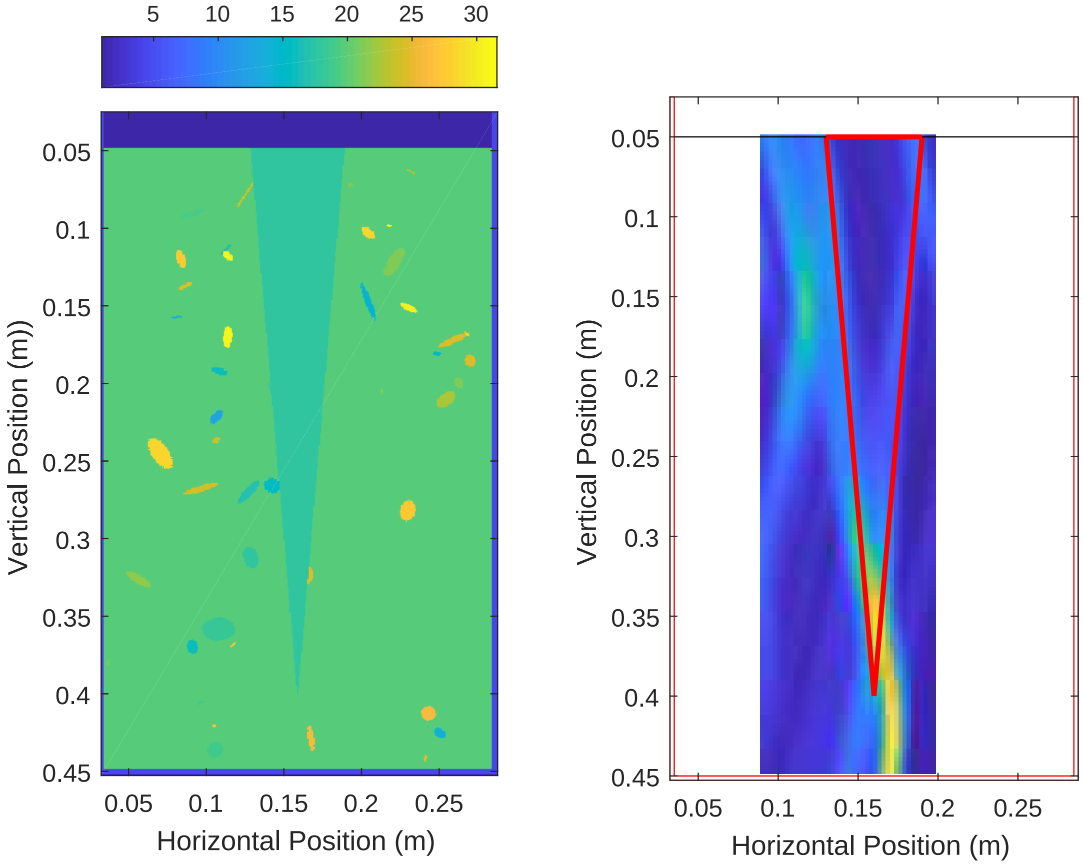

(a) The relative permittivity distribution of Root Test Number 6.

(b) The unprocessed DAS beamforming image for Root Test Number 6.

Figure 5.5: The unprocessed DAS beamforming image for a root with $\epsilon_r = 18$.

Figure 5.5 shows the image quality is severely reduced. Most of the energy in the image is concentrated around an area that is not near the front surface of the root. It would be very difficult to determine which regions of the image was related to the root without prior knowledge of the location of the root. Root Test Number 6 shows the limitations of the UWB imaging system designed when operating under noisy conditions with low contrast. It becomes impossible to separate information on the root from unwanted noise with a low relative permittivity contrast. This has been a common issue for many other non-destructive root imaging methods such as MRI and PET.

5.3 Steering Vector Analysis

The time saved using the simplifications made to the ray path calculations in Section 4.3.3 is shown in Table 5.4. Table 5.4 compares the approximate processing time to generate the DAS beamforming images for 6, 12, and 21 scanning positions.

Table 5.4: Calculation times for the complex and simplified path ray calculations for varying scan numbers.

Number of Scans	Complex DAS Beamforming Time (min)	Simple DAS Beamforming Time (min)
6	35.6	2.2
12	50.3	4.5
21	90.0	10.2

Qualitatively examining the figures in Figure 5.6 shows that they are very similar, with very little degradation in quality in the simplified image.

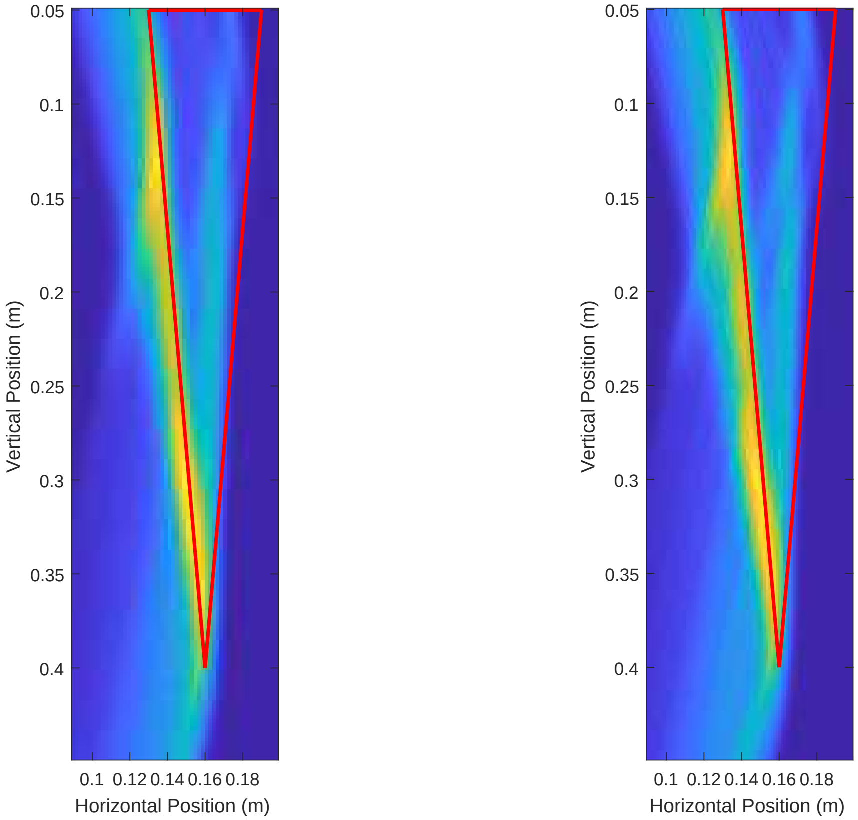

(a) Complex steering vector ray paths. **(b)** Simplified steering vector ray paths.

Figure 5.6: Unprocessed DAS beamforming images for (a) 12 scans with the complex steering vector ray path calculations and (b) 12 scans with the simplified steering vector ray path calculations.

Table 5.5 shows the error in the measurements between the complex and simplified ray path calculation type. There are 12 scans keeping 35% of the energy and with a 1 cm radius for erosion and dilation of image with no binary mask erosion. The quantitative results show that there is little difference between the complex and simplified methods of calculation. The impact of the simplifications made in Section 4.3.3 is negligible when considering the final result of the DAS beamforming method.

Table 5.5: Measured root depths and root average diameters for the complex and simplified ray path calculations.

Ray Path Calculation Type	Measured Root Depth (cm)	Error in Depth Measurement (cm)	Average Measured Root Average Diameter (cm)	Error in Average Diameter Measurement (cm)
Complex	36.54	+1.54	3.01	+0.01
Simplified	36.27	+1.27	3.13	+0.13

5.4 Window Size Parameter Analysis

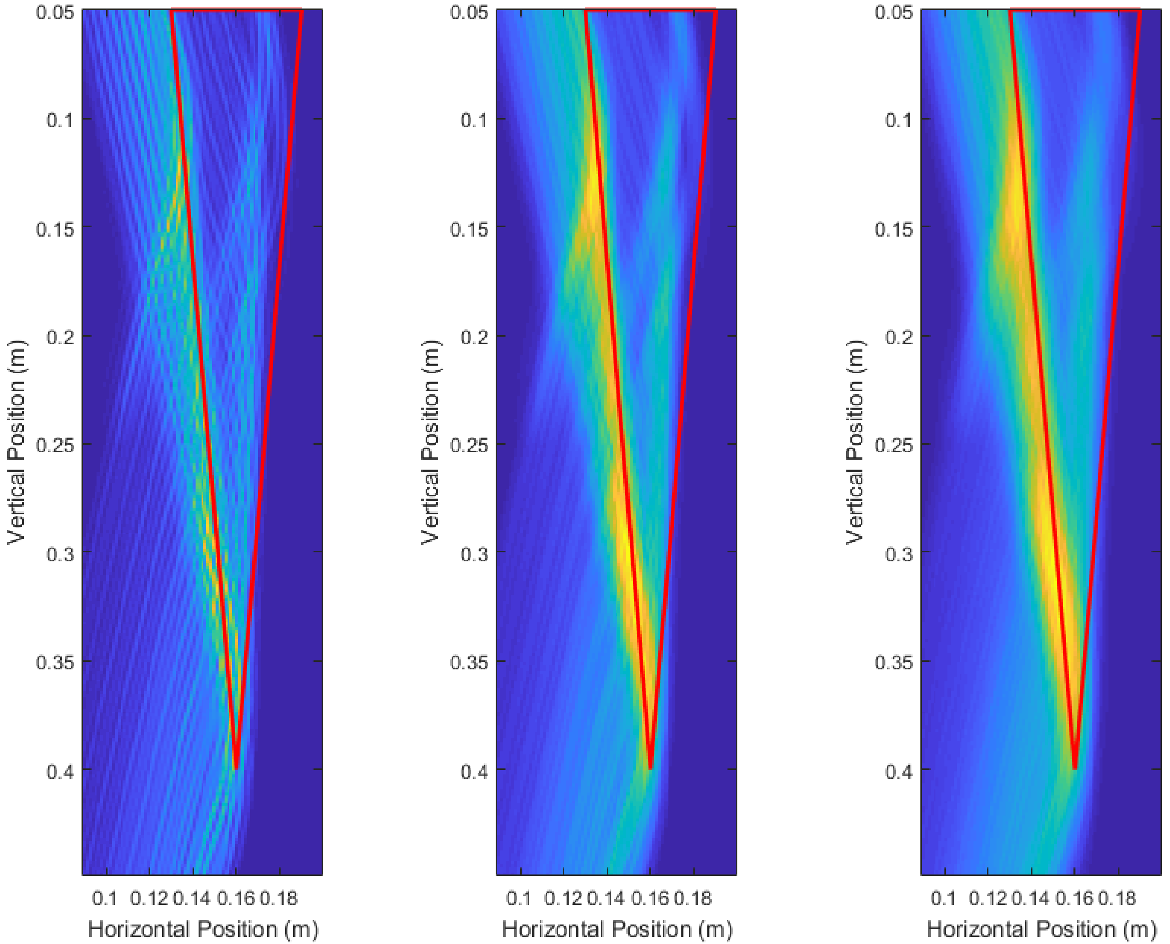

(a) Quarter cycle length. **(b)** Half cycle length. **(c)** One-and-half cycle length.

Figure 5.7: Unprocessed DAS beamforming images for (a) Quarter carrier cycle length (b) half carrier cycle length, and (c) one-and-half carrier cycle length

The window size W selected for the DAS beamforming algorithm needs to be carefully determined based on the period of the carrier frequency. If the window size is too short, then the energy contributions due to the oscillations of the carrier frequency become apparent. Figure 5.7a uses a quarter cycle length for the window size and has artifacts caused by the carrier frequency oscillations. Figure 5.7b uses a half cycle for the window size has some artifacts caused by the carrier frequency are evident. Figure 5.7c uses a one-and-half cycle length for the window size and there are no artifacts caused by the carrier frequency. However, too large of a window size puts the DAS beamformed image at higher risk to have artifacts caused by signal interference.

As such, about one cycle length is optimal for the beamforming algorithm, long enough to avoid carrier frequency artifacts and short enough to reduce reflection interference. Figure 5.1b, and all other scans in the analysis of this thesis, uses a one cycle length window size.

5.5 Morphological Transformation Parameter Analysis

The modified top-hat transformation, defined by Equation (4.59) to be

$$\mathbf{T}(x, y) = \mathbf{I}(x, y) + ((\mathbf{I}(x, y) \ominus \mathbf{b}) \oplus \mathbf{c})$$

is useful for emphasizing the surface of the roots in the DAS beamforming images. The transformation raises the intensity of larger objects in the image (which is generally the root) while reducing the intensity of smaller objects. The optimal selection of **b** and **c** is largely dependent the characteristics of the root to be imaged. Generally **c** will be selected to be roughly the same size at **b** to restore any lost information on the surface of interest. The optimal size for **b** is dependent on how large the root being imaged is. The larger the root, the larger **b** can be to reduce the intensity of smaller artifacts present in the image. Figure 5.8 compares the unprocessed image and the processed image on a root that has been distorted by macroscopic objects. A circular structuring element approximately 4 mm in diameter is used for both **b** and **c**.

The areas associated with the surface of the root become emphasized while some distortions, such as the high intensity distortion near the bottom tip of the root, are de-emphasized. Overall, this helps the unsupervised image processing method to identify the most likely location of the root.

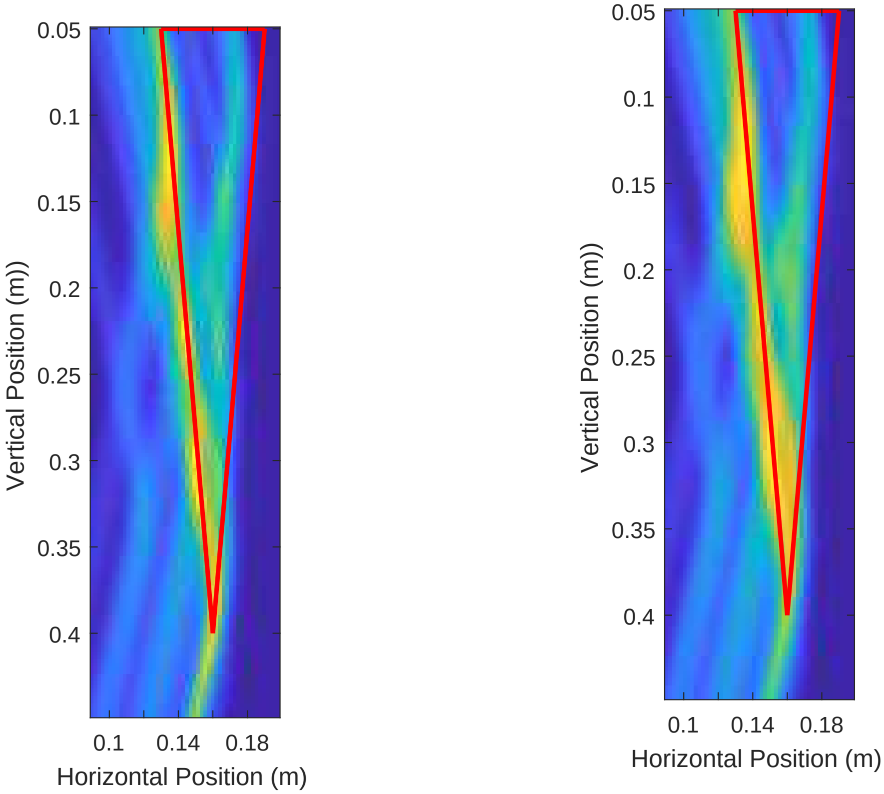

(a) Unprocessed DAS beamforming image.

(b) DAS beamforming image after modified top-hat.

Figure 5.8: DAS beamforming results for (a) the unprocessed image and (b) the image after the modified top-hat transformation.

The high intensity distortion near the bottom tip of the root is a common artifact caused by the beamforming algorithm. Occasionally, the modified top-hat transformation isn't sufficient to completely remove this 'tail' artifact. Once a quantized image is formed, we can use a binary erosion on the image to remove small distortions based on size and shape alone (and not intensity, which is what the modified top-hat transform also is dependent on). A subsequent binary dilation is also performed to restore any lost edges on the larger regions remaining after the binary erosion. Figure 5.9 shows the results of a binary erosion and dilation of 1 mm diameter.

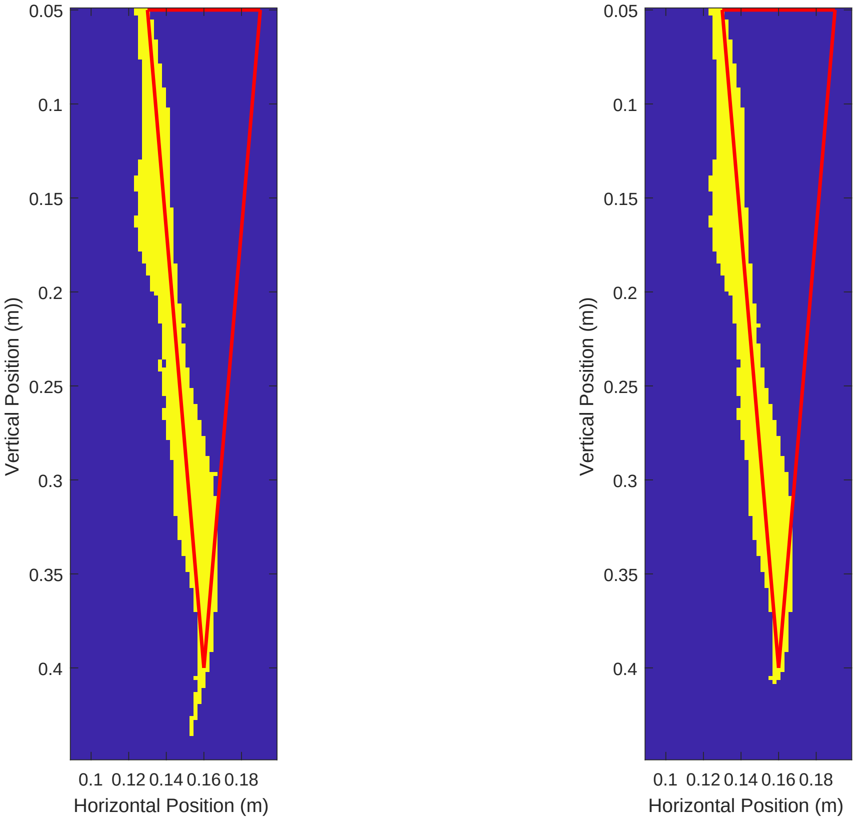

(a) No binary erosion.

(b) Binary erosion and dilation.

Figure 5.9: Binary masks for (a) no binary erosion performed and (b) a binary erosion and dilation performed.

The binary erosion significantly improved the measurements of the root by removing the ’tail’ artifact almost entirely. The image with no binary erosion had a height of 38.97 cm and average diameter of 2.87 cm. The image with a binary erosion and dilation had a height of 36.19 cm and average diameter of 2.97 cm.

Overall, morphological transformations are essential tools for refining the images produced by DAS beamforming, but careful selection of the parameters is needed to improve results rather than harming them. For example, for the same root as in Figure 5.9b, instead of using a 1 mm diameter structural element for the binary erosion, a 3 mm diameter one is used instead. This results in measurements of 29.34 cm depth and 2.84 cm average diameter, severely degrading the measurements since the erosion removes information on the root, and not just smaller artifacts. Selection of these structuring parameters is a task which requires knowledge of the intensity and size of any unwanted artifacts present.

5.6 Image Quantization Parameter Analysis

The image quantization used to generate the binary mask makes heavy use of the energy histograms as discussed in Section 4.4.1. As previously mentioned, high intensity regions in the image correlate to the location of reflecting materials in the media. If these high intensity regions are relatively localized to the surface of the root, and there aren't many other regions of high intensity in the image, then the energy histogram and cumulative energy histogram will show that most of the energy lies in higher intensity pixels.

The binary mask will keep a certain percentage of energy in the image, starting from the higher intensity pixels. Appropriate selection of this percentage is crucial to retaining information on the root while removing noise in high noise images. For images with low noise, any percentage between 30% and 60% will perform well in measurements. For higher noise images, a larger percentage is needed to prevent the removal of root information. The high noise image as shown in Figure 5.5 shows that distortions and artifacts dominate the image. To handle this, a higher percentage of energy is retained in the mask to ensure that all the root information is kept.

Figure 5.10a shows that retaining only 35% keeps the artifacts caused by other scatterers in the soil. Since the noise in the image dominates the desired root reflections, we cannot rely on assuming that the root will be the best reflector in the soil. Instead, more energy must be retained, in this case 70%, to keep the desired root information. Assuming the actual location of the root is relatively unknown, it is still very difficult to isolate the root surface. In general, as previously mentioned in Section 4.4.1 on energy histograms, if the 50% cutoff intensity is less than 100 (on a range of 0 to 255 for an 8-bit grayscale), there are likely many other scatterers in the soil and a larger percentage of energy should be retained.

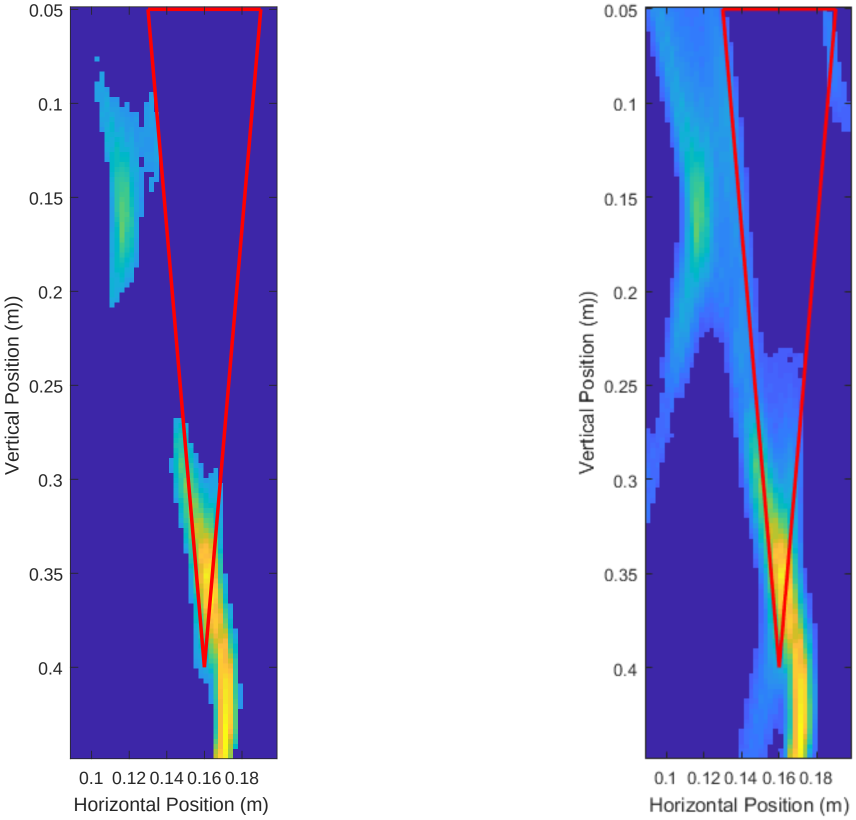

(a) 35% percent energy retained.

(b) 70% percent energy retained.

Figure 5.10: Comparison of a high noise image with (a) 35% percent energy retained and (b) 70% percent energy retained.

Chapter 6

Implementation of Experimental Trials Methodology and Results

This chapter describes the implementation of the hardware needed to conduct the experimental trials of this thesis. Section 6.1 describes the hardware implementation of the Data Acquisition module. Section 6.2 describes the extra filtering and upsampling needed to improve the quality of the collected scans from the experimental trials. Section 6.3 covers the relative permittivity used for the soil in the DAS beamforming algorithm. Section 6.4 covers the determination of the ground truths for the depth and average diameter of the buried carrots to be scanned. Section 6.5 contains the imaged results and measurements of the experimental trials conducted.

6.1 Data Acquisition: Hardware Implementation

6.1.1 PulsOn 410 by Time Domain Specifications

The UWB device used for transmitting and receiving the UWB signals is the PulsOn 410 (P410), and detailed information can be found on the Time Domain website [21]. The device transmits a 3.1 GHz to 5.3 GHz pulse and relays its measurements, sampled of approximately 16.4 GSa/s, via a USB connection. The device is compact, sitting on a 7.6 x 8.0 cm board which allows for portability and ease of use.

6.1.2 Apparatus and Scanning Set-up

An apparatus was constructed to hold the P410 device allowed for easy adjustment of the transceiver height using a ball bearing platform and a clamping tool. Calibrating tests were done to measure the device's delays. Since the P410 does not have a collocated transceiver, a non-contact, bi-static SAR scanning procedure was used. The location of the transmitter was used as reference during the scans and processing. The receiver and transmitter are separated by 4 cm from center to center. Figure 6.1 shows the scanning set-up for the system.

The P410 was interfaced with MATLAB using a USB port. A graphical user interface (GUI) was designed in MATLAB to streamline the scanning process and shorten scanning times. For each buried root, 4 sets of vertical scans positioned at 0°, 90°, 180°, and 270°are done. This allows us to construct a cross-sectional image of the buried root to be measured for depth and average diameter. Angles 0°and 180°will form cross-section side 1 and angles 90°and 270°will form cross-section side 2 on each carrot. Each vertical scan consists of 10 individual scans spaced 1 cm apart. Similar to the simulations, the scans begin at 2 cm from the surface of the soil to minimize unwanted interference from the soil-air interface at the surface of the soil.

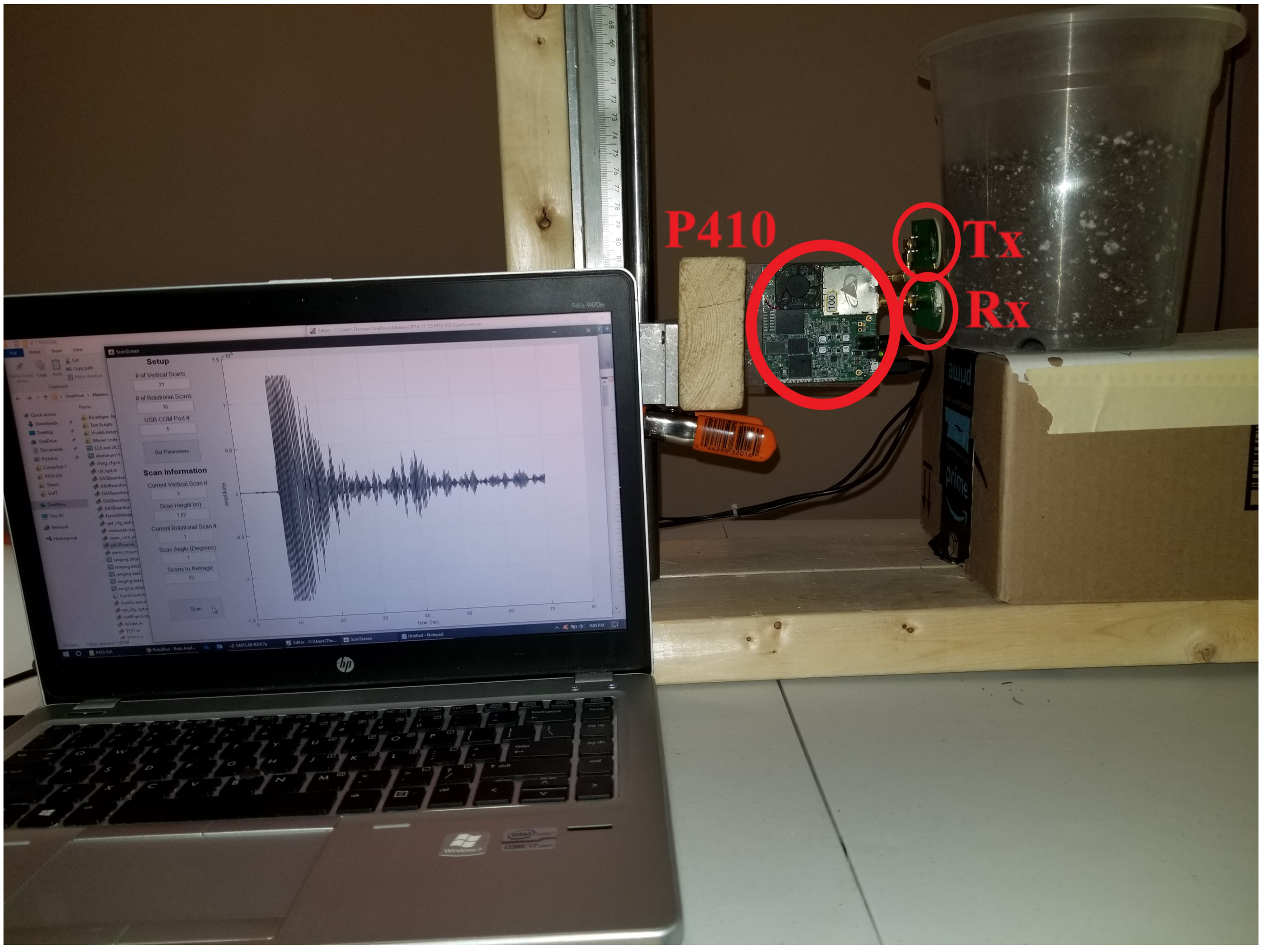

Figure 6.1: Apparatus set-up for scanning buried roots.

6.1.3 Pot and Root Characteristics

Figure 6.2 shows the physical dimensions of the potted taproot. The main difference between the experimental set-up and the simulated set-up is the separation of the transmitter and receiver by 4 cm since the P410 uses separate antenna for transmitting and receiving. The vertical positions of the transmitter were adjusted based on the center of the transmitting antenna. Other differences include the depth of the soil, size of the pot, and size of the taproot (a carrot is chosen) due to the availability of materials for the apparatus. Two carrots were scanned, Carrot 1 with approximately 6.3 cm depth and 2.2 cm average diameter, and Carrot 2 with approximately 5.6 cm depth and 2.1 cm average diameter. The scan height measurement is taken from the center of radiation of the transmitter. Additional results on other types of taproots are found in the Appendix.

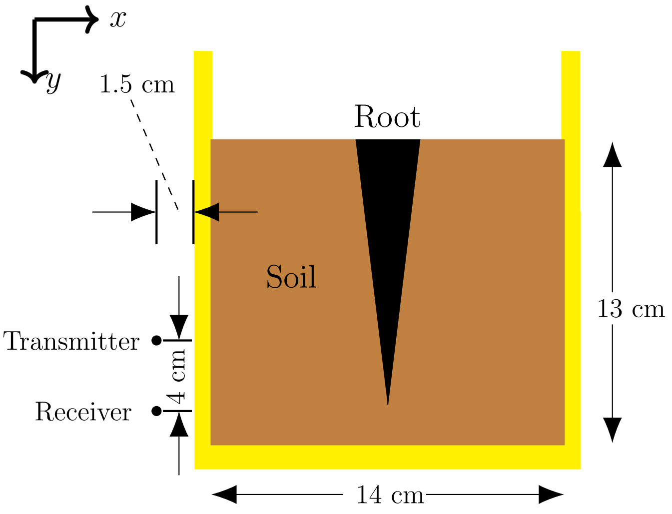

Figure 6.2: Dimensions of the P410 imaged potted carrot.

6.1.4 Data Acquisition Results

Figure 6.3 shows an example of a reflected waveform. The P410 was originally meant for long distance ranging purposes, so at minimum it collects 70 ns of measurements. A series of calibration tests to determine the start up time to be $t_0 \approx 11$ ns. This start up time is used to calculate part of the time delay for the steering vector in Equation (4.50).

With the selected physical parameters, the region of interest lies at around the 12 ns to

13 ns for calculating the DAS beamforming image. Unfortunately, this portion is in an area with large amounts of noise caused by the hardware in the P410 [21]. This hardware noise will be dealt with in Section 6.2.

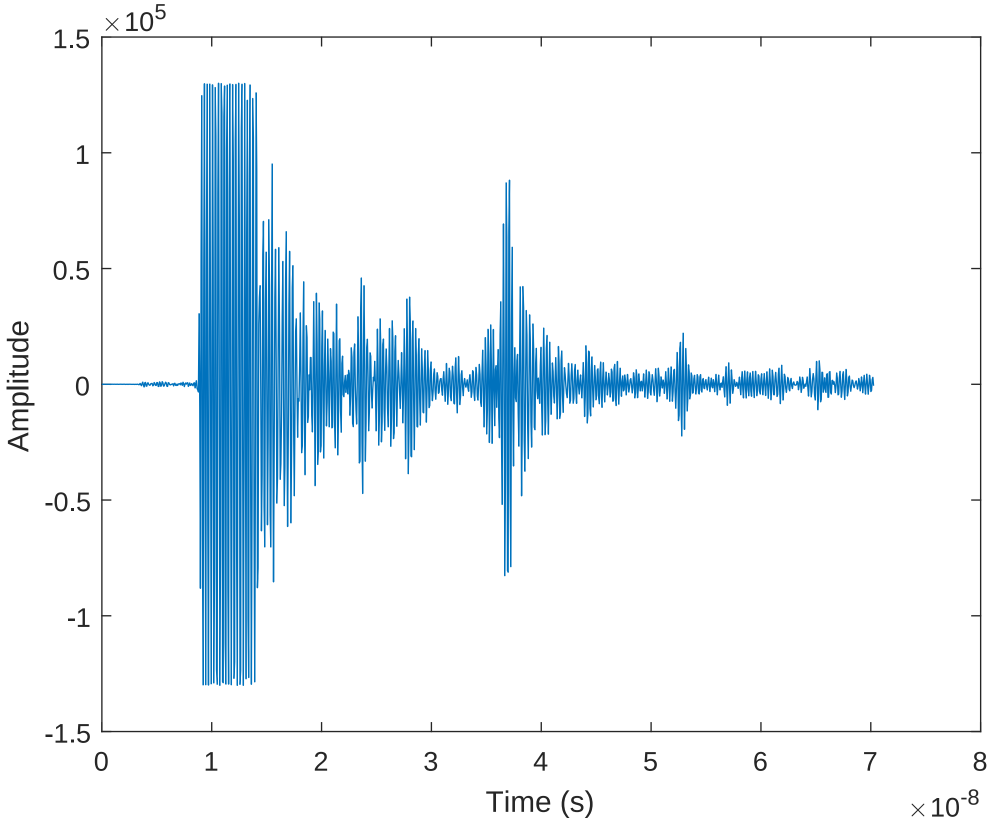

Figure 6.3: Example of a reflected waveform measured by the P410 device.

6.2 Data Processing: Noise Filtering and Upsampling

6.2.1 Wiener and Bandpass Filtering

The development of the Wiener filter uses section 18.6.3 of the Digital Signal Processing Handbook as reference with modifications to suit the problem at hand [55].

As seen in Figure 6.3, there is significant noise in the measured signals caused by the hardware in the first 15 ns of the captured waveform [21]. Since the noise is consistent in terms of amplitude and temporal location, the Wiener filter is able to estimate it on the assumption that the rest of the signal consists of only additive random processes.

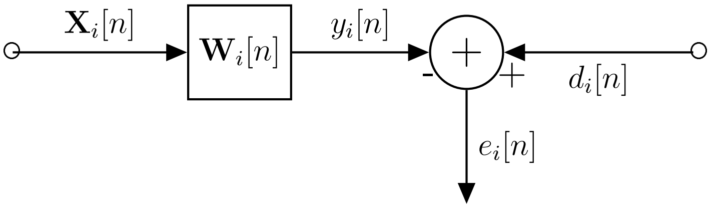

Figure 6.4: Block diagram for hardware noise removal system.

Figure 6.4 shows the general block diagram for the process to remove the hardware noise. The goal of a Wiener filter is to design the filter, $\mathbf{W}[n]$, to minimize the mean-squared error cost function, $J_{MSE}[n]$. $J_{MSE}[n]$ is defined as:

$$J_{MSE}[n] = \frac{1}{2}E(e^2[n]) \tag{6.1}$$

where:

- $J_{MSE}[n]$ is mean-squared error cost function.
- $E(e^2[n])$ is the expected value of the squared error.

Given $b_i[n]$ with $i = 1, 2, \ldots, N$ scans and Equation (6.1), we define the estimated hardware noise for the i$^{\text{th}}$ scan to be $y_i[n]$. We let the desired signal to be $d_i[n] = b_i[n]$. The input $\mathbf{X}_i[n]$ is a matrix which contains all the scans except for the i$^{\text{th}}$ scan. The optimal values for $\mathbf{W}_i[n]$ that minimize $J_{i,MSE}[n]$ for the i$^{\text{th}}$ is:

$$\mathbf{W}_i[n] = \mathbf{R}_{i,XX}^{-1}[n]\mathbf{P}_{i,DX}[n] \tag{6.2}$$

where:

- $\mathbf{W}_i[n]$ is the optimized filter to minimize $J_{MSE}[n]$ for the i$^{\text{th}}$ scan.
- $\mathbf{R}_{i,XX}^{-1}[n]$ is defined as $E(\mathbf{X}_i[n]\mathbf{X}_i^T[n])$.
- $\mathbf{P}_{i,DX}[n]$ is defined as $E(d_i[n]\mathbf{X}_i[n])$.

Equation (6.2) calculates the required filter coefficients to minimize $J_{i,MSE}[n]$. We can now calculate $y_i[n]$, which is the the estimated hardware noise for the i$^{\text{th}}$ scan using:

$$y_i[n] = \mathbf{W}_i[n]\mathbf{X}_i[n] \tag{6.3}$$

Equation (6.3) calculates the hardware noise signal for each scan. Equation (6.4) is the measured reflected signal with the hardware noise removed.

$$\beta_i[n] = b_i[n] - y_i[n] \tag{6.4}$$

Next, a bandpass filter with cut-off frequencies of 3.1 GHz to 5.3 GHz is used to remove unwanted electromagnetic noise at frequencies beyond the frequency of the P410. The Canadian Table of Frequency Allocations specifies many uses for frequencies in and around the P410 device for mobile use [56]. In particular, Wi-Fi and bluetooth services operate around 2.4 GHz and is present in the spectrum of each Wiener filtered scan $\beta_i[n]$. The filter is designed with MATLAB's *designfilt* command to be a bandpass filter with order 100 [53]. The order was chosen to be very large in order to ensure adequate attenuation outside the pass band. Figure 6.5 shows the pass and attenuation bands of the designed filter.

The filtered signal is denoted as:

$$\beta_{i,bp}[n] = \beta_i[n] * H[n] \tag{6.5}$$

where:

- $\beta_{i,bp}[n]$ is Wiener and bandpass filtered $b_i[n]$.
- $H[n]$ contains the filter coefficients for the 3.1 GHz to 5.3 GHz signal.

6.2.2 Upsampling and Interpolation

The sampling frequency of the device is 16.384 GSa/s, resulting in a sample every 61 ps and this severely limits the abilities of DAS beamforming. In theory, 61 ps is enough time for electromagnetic waves in free space to travel $(61 \times 10^{-12} \cdot c_0) = 1.8 \times 10^{-2}$ m. For calculating

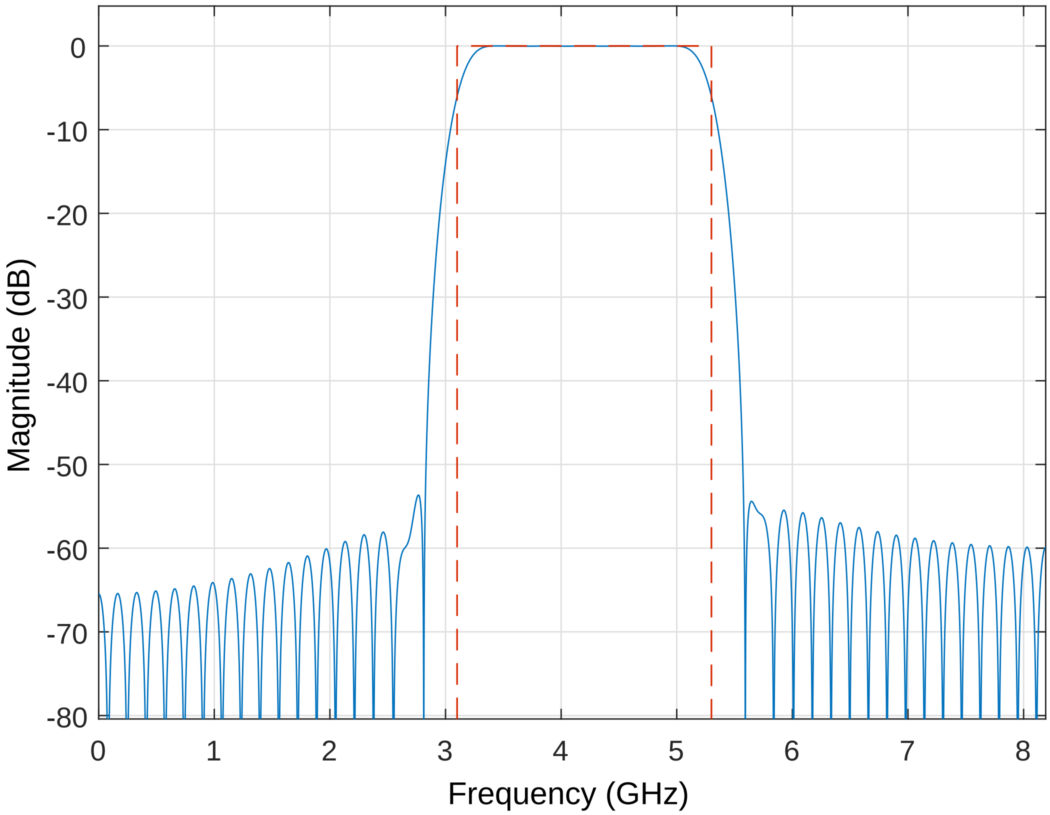

Figure 6.5: Bandpass filter $H[n]$ spectrum used to filter $\beta_i[n]$.

the steering vector, since a two-way path from transmitter to imaging point to the receiver is used, half of this distance (0.9 cm) becomes the limit on the pixel dimensions for DAS beamforming in free space for a single scanning location. If the flight path distance from transmitter to arbitrary point A back to transmitter is within ±0.45 cm of the flight path distance from transmitter to arbitrary point B back to transmitter, then one or both of these flight path distances will be rounded when calculating the steering vector and there will be no distinction between the points A and B. In non-magnetic media, such as soil, the velocity of electromagnetic waves is $v_{soil} = \frac{c_0}{\sqrt{\epsilon_{r,soil}}}$ and thus the limit on the resolution for a single transceiver becomes $\frac{0.9}{\sqrt{\epsilon_{r,soil}}}$ cm. Typical relative permittivity values for dry soil at room temperature at around 4.2 GHz provides about a 0.2 cm limit on the pixel dimensions [47,57].

There are many other factors which need to be considered in the resolution capabilities of this system, so potential issues regarding the sampling rate of the P410 is eliminated by upsampling and interpolating. MATLAB's *interp* function upsamples a given signal and then interpolates the new samples to minimize the mean-square error between the new samples and their ideal values [53]. $B_i[n]$ will be used to denote the final filtered, upsampled, and interpolated signal. An upsampling factor of 10 was found to have the best results for all scans taken.

6.3 Data Processing: Delay-and-sum Beamforming Methodology

The delay-and-sum beamforming algorithm used for the experimental trials is unmodified from the algorithm used for the simulated trials, with the exception of $B_i[n]$ being used in placed of the unfiltered $b_i[n]$. See Section 4.3 for a detailed formulation. The height used for the DAS beamforming algorithm is the height of the transmitter for the experimental trials. The soil relative permittivity $\epsilon_{r,soil}$ used in the steering vector calculations was determined empirically through trial and error by comparing the average diameter and depth results to the ground truth. In the end, for the soil used, a relative permittivity of about 25 was used for the soil since this value provided the most accurate diameter and depth measurements. This falls in line with literature for dry soil at frequencies around 4 GHz [47, 57].

6.4 Image Processing and Analysis: Methodology

For the most part, the methodology used for the experimental trials is unmodified from the algorithm used for the simulated trials. See Section 4.4 for a detailed formulation. The difference is that there is an additional procedure for calculating the ground truths for the depth and average diameter measurements.

6.4.1 Methodology for Calculating Ground Truth Depth and Average Diameter

Top-down image of the carrots to be scanned are taken with an RGB camera, as shown in Figure 6.6. The carrots are on top of a monotonously coloured background alongside measuring tape. The RGB image captured is cropped to remove the measuring tape then segmented using MATLAB's *kmeans* function which segments the image based on the K-Means clustering method [53]. The segmentation separates the carrot from the paper background. The pixel density for the image is manually measured by using the measuring tape to scale.

Figure 6.6: An example of the RGB image taken to determine the ground truth values for the depth and average diameter of the buried carrot.

The observed area of the carrot is approximated by counting the number of pixels in the segmented area. The height of the carrot is measured by collapsing the columns with a bitwise 'or' operation and then summing the remaining pixels. The average diameter is then calculated by dividing the measured area by the measured height.

6.5 Image Processing and Analysis: Results

Figures 6.7 and 6.8 show the unprocessed DAS beamforming results for Carrot 1, which was measured to have a depth of 6.3 cm and an average diameter of 2.1 cm. The scans at 90°and 270°are flipped and concatenated with 0°and 90°, respectively, to create a cross-sectional image of the scanned root in the pot for easier viewing. Each of the images at still processed individually for measurements. Similar to the simulated experiments, the large size of the high intensity areas makes determining the location of the root fairly uncertain relative to the root's overall size. This causes issues with determining finer details in the root itself. Using the developed image processing and analysis methods from the simulations, we arrive at an average depth measurement of 5.9 cm and an average diameter of 2.6 cm.

Figures 6.9 and 6.10 show the results for Carrot 2, which was measured to have a depth of 5.7 cm and an average diameter of 2.1 cm. These set of scans suffer from the same issues as the other root, but the system shows consistency in its measurements. We have an average depth measurement of 5.4 cm (averaged across the 4 produced images) and an average diameter measurement of 2.5 cm.

Table 6.1 summarizes the experimental trial results, as well as the ground truth results. Note that the measured depths for all tests are consistently lower than the true depth. This suggests difficulties in detecting the tips of the carrots in the soil and results in larger average diameter measurements.

Table 6.1: Summary of depth and average diameter measurements on the experimental trials.

Carrot Test Number and Side	Depth Measurement (cm)	True Depth (cm)	Diameter Measurement (cm)	True Diameter (cm)
Carrot 1, Side 1	5.75	6.29	2.85	2.32
Carrot 1, Side 2	6.05	6.26	2.36	2.13
Carrot 2, Side 1	5.45	5.61	2.40	2.10
Carrot 2, Side 2	5.30	5.51	2.63	2.08

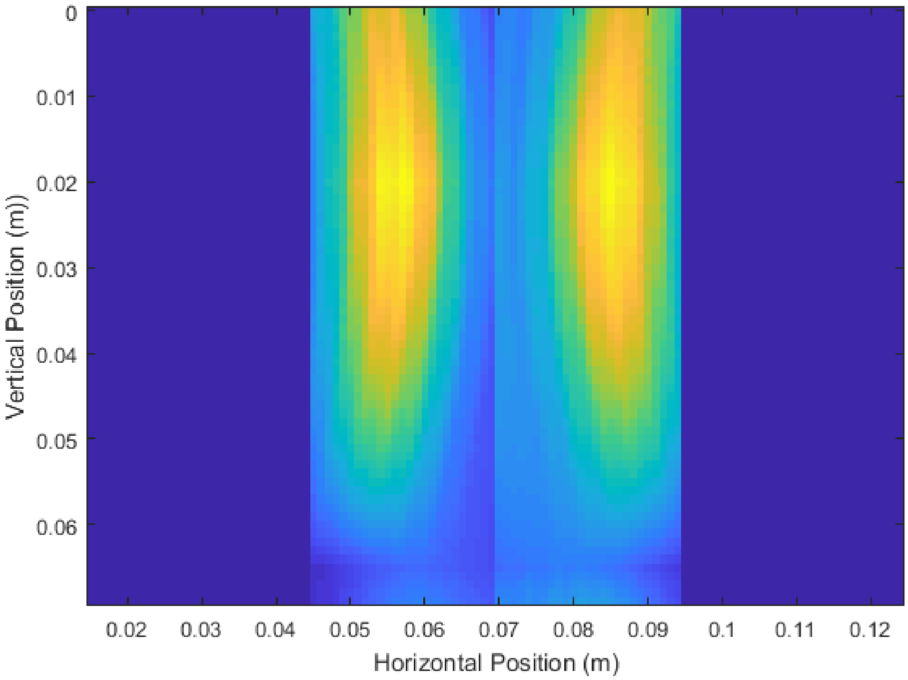

Figure 6.7: Unprocessed DAS beamforming results of Carrot 1 Side 1 with vertical scans taken at 0°and 180°, depth measurements after processing of 5.7 cm and 5.8 cm respectively. Average diameter after processing measured to be 2.85 cm.

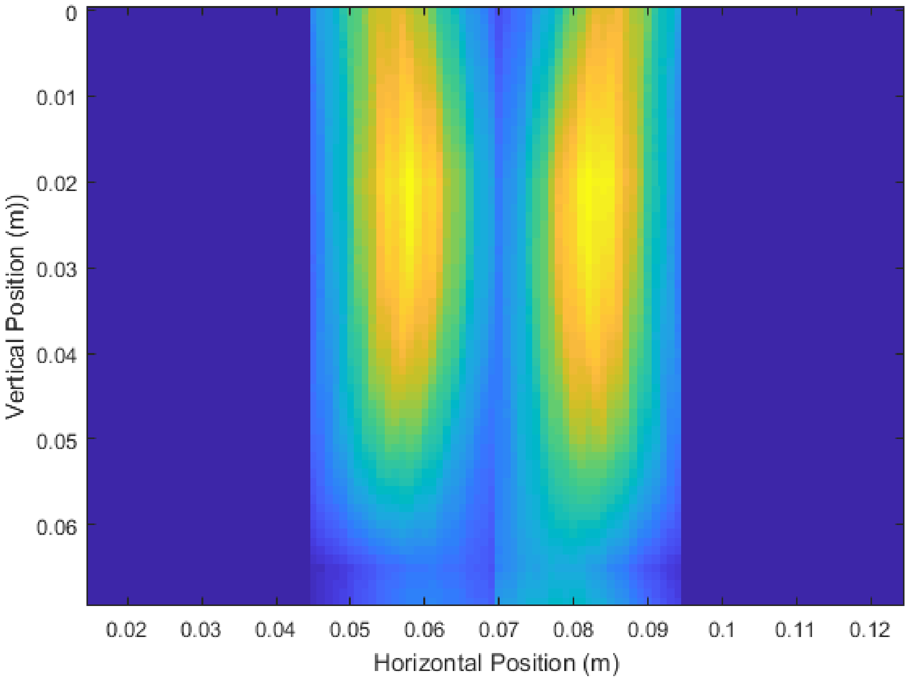

Figure 6.8: Unprocessed DAS beamforming results of Carrot 1 Side 2 with vertical scans taken at 90°and 270°, depth measurements after processing of 5.7 cm and 6.4 cm respectively. Average diameter after processing measured to be 2.36 cm.

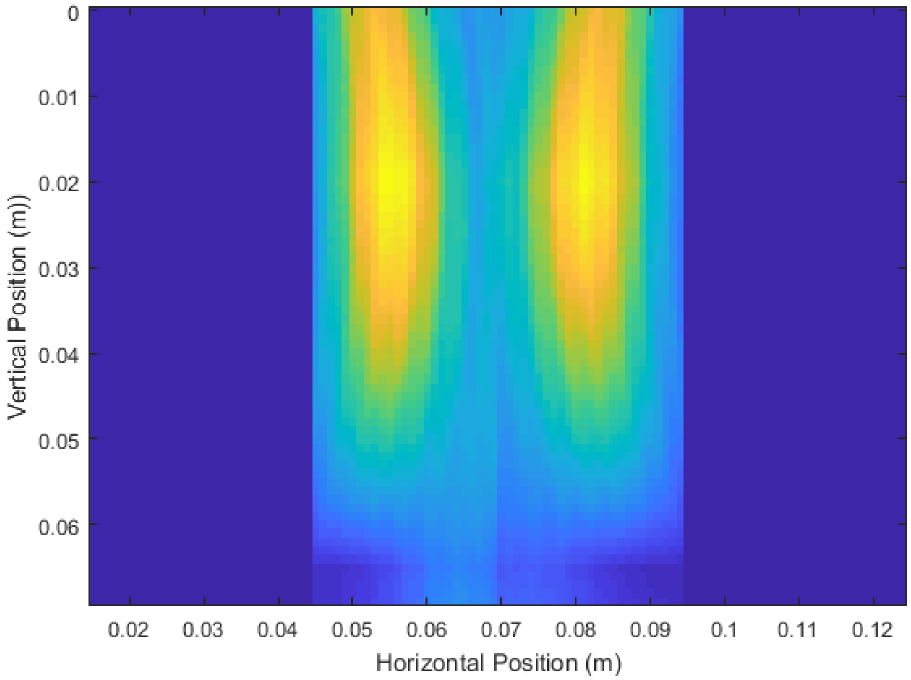

Figure 6.9: Unprocessed DAS beamforming results of Carrot 2 Side 1 with vertical scans taken at 0°and 180°, depth measurements after processing of 5.5 cm and 5.1 cm respectively. Average diameter after processing measured to be 2.40 cm.

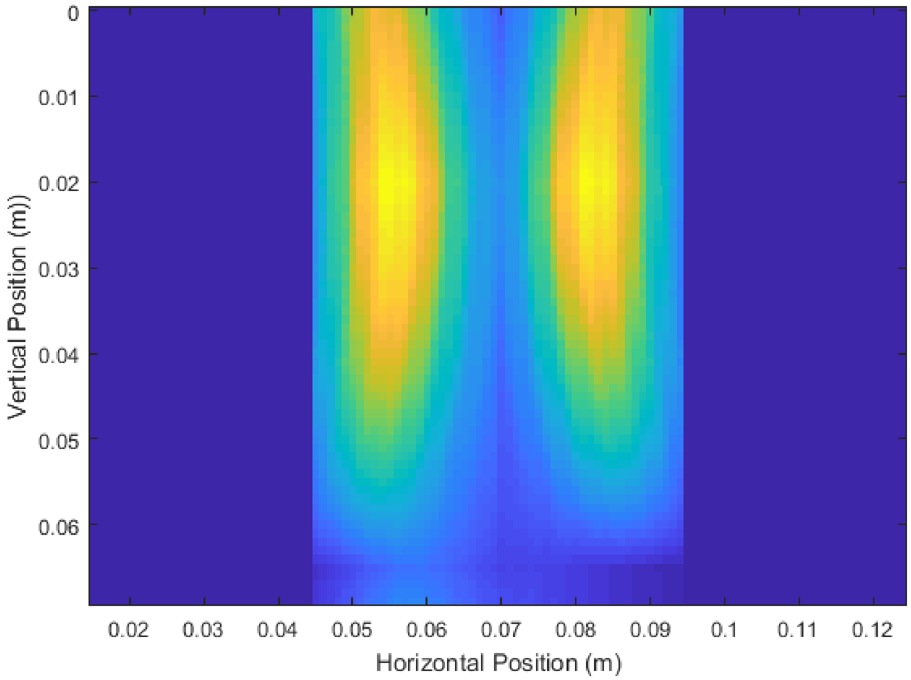

Figure 6.10: Unprocessed DAS beamforming results of Carrot 2 Side 2 with the vertical scans taken at 90°and 270°, depth measurements after processing of 5.6 cm and 5.3 cm respectively. Average diameter after processing measured to be 2.63 cm.

Chapter 7

Simulating Experimental Trials and Sources of Improvement

This chapter seeks to recreate the experimental trials using simulations in order analyze both the simulated and experimental systems for sources of improvement. Simulating the circumstances for the experimental trials is needed to accomplish two crucial goals. The first goal is to verify the accuracy of the simulation set-up and the simplifications that were made to reduce simulation complexity. This is covered in Section 7.1. The second goal is to examine faults and seek sources of improvement for the experimental trials. This is covered in Section 7.2. The primary differences between the simulated trials and the experimental trials were the source waveform used and the physical and electrical parameters of the system under test.

7.1 Simulation Parameters to Match Experimental Trials

7.1.1 P410 Source Waveform

Figure 7.1 shows the source waveform of the P410 device as measured by the developers at Time Domain [21]. Some important qualities of this waveform to note is that there is a lot of noise and some distortion caused by the measurement hardware once the initial pulse has finished. Moreover, the duration of the main pulse is approximately 1.8 ns, which is significantly longer than the 1.0 ns duration of the pulse used in the simulated trials. This causes the more energy to be spread in the DAS beamforming image, resulting in larger areas of high intensity which in turn means less certainty in the exact location of the surface of the root. The waveform depicted in Figure 7.1 is modified by removing the ringing caused by the hardware after about 4.5 ns. This modified waveform will be the source waveform to be injected into the simulations.

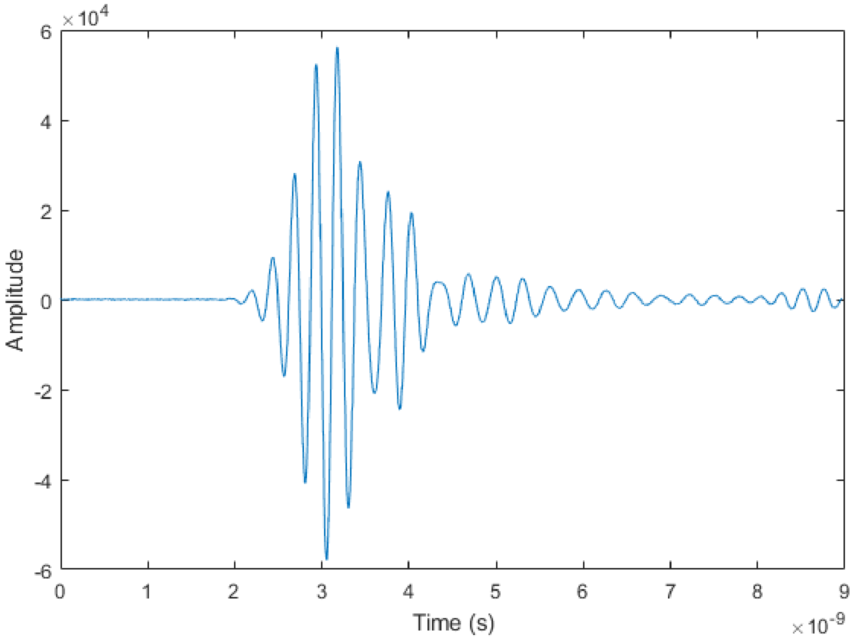

Figure 7.1: UWB source waveform for the P410 device.

7.1.2 Physical and Electrical Parameters

Figure 7.2 shows an example of the physical and electrical parameters of the system under test for simulating Carrot 1, Side 1 from the experimental trials. $\epsilon_{r,soil} = 25$ is selected and $\epsilon_{r,root} = 10$ is selected. The transmitter and receiver are separated by 4 cm to simulate the bi-static set-up of the P410 antenna. The top marked 'x' is the transmitter location while the bottom marked 'x' is the receiver location. The transmitter and receiver are positioned 1.5 cm from the surface of the pot. 10 scan positions were made starting at 2 cm depth from the soil and ending at 11 cm depth. The root itself was modeled by taking the diameter at the top and diameter at the bottom and linearly interpolating the shape of the root in between top and bottom.

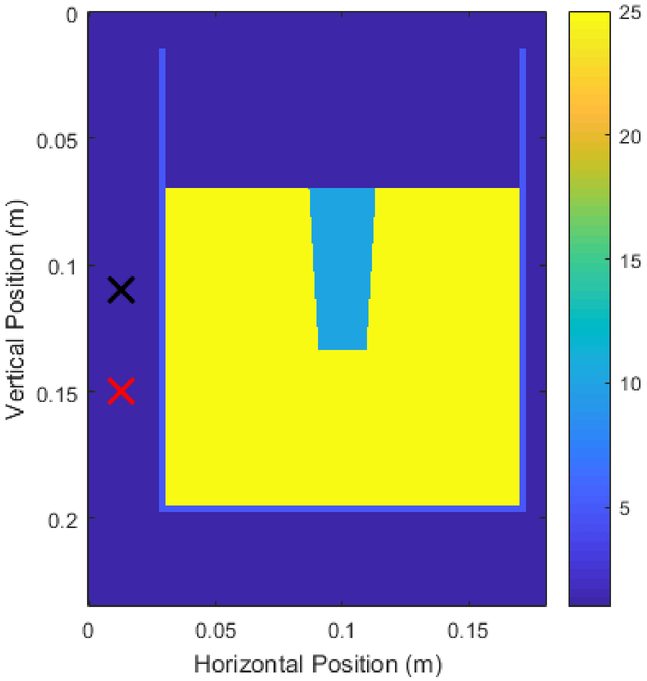

Figure 7.2: Physical and electrical parameters of system under test which models the experimental trials.

7.1.3 Data Processing and Image Processing Parameters

The simulations must have a minimum time step according to the Courant stability condition outline in Section 4.2.1. As such, the measured signal from the simulations is resampled to match the P410 sampling frequency. After the resampling, the data processing and image processing modules are unmodified.

7.1.4 Simulation Results

Figure 7.3 shows the results of the simulations for Carrot 1. Note that the DAS beamforming was done for areas past the center of the pot to check if the back surface of the root interferes with the front surface of the root. For Carrot 1, the back surface reflections do not interfere with the front surface. Figure 7.4 has the results for Carrot 2, however, there is some interference due to the differences in the size and shape of the root. This shifts the center of the area towards the center of the pot, which coincidentally is beneficial to the measurement algorithm, but only if this interference is known to be present. To compensate for this

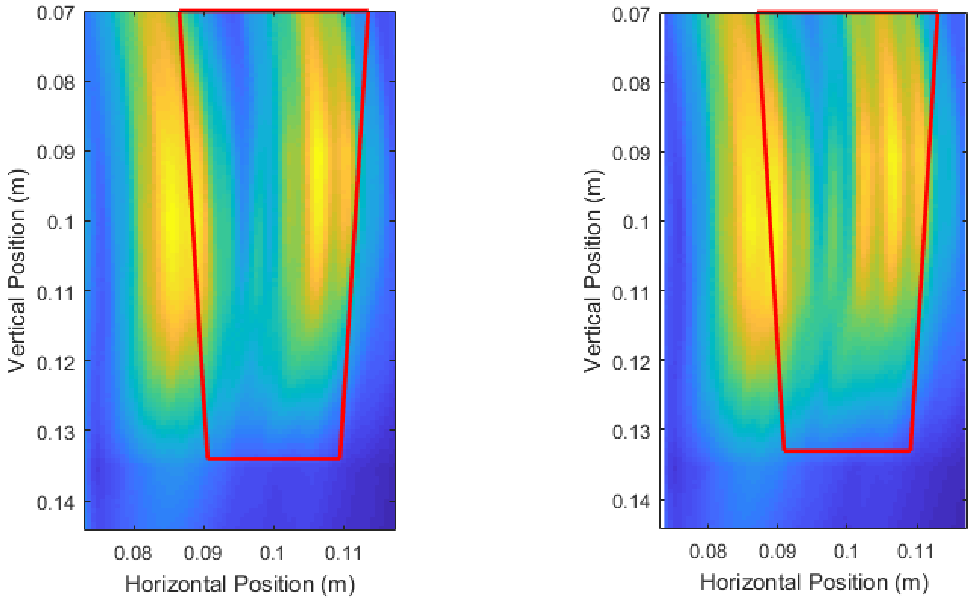

(a) Unprocessed DAS beamforming image for Carrot 1, Side 1.

(b) Unprocessed DAS beamforming image for Carrot 1, Side 2.

Figure 7.3: Unprocessed DAS beamforming images for (a) Carrot 1, Side 1 and (b) Carrot 1, Side 2.

interference, instead of removing half the area of the intensity area, we remove one third of the area for better measurements.

Ignoring the area past the center of the pot (which is at 10 cm in the horizontal position of the simulation grid), we arrive at very similar qualitative results to the experimental trials. This justifies the simplifications made in our simulations to be negligible, at least for the current hardware and set-up limitations. Tables 7.1 and 7.2 shows that the measurements between the experimental trials and the simulated recreation are also similar.

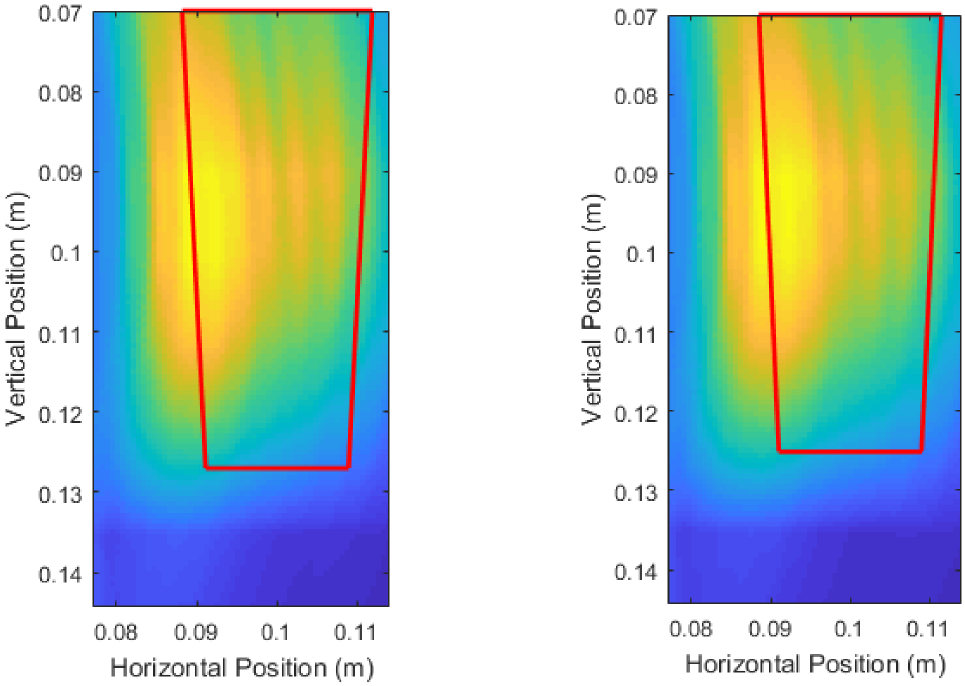

(a) Unprocessed DAS beamforming image for Carrot 2, Side 1.

(b) Unprocessed DAS beamforming image for Carrot 2, Side 2.

Figure 7.4: Unprocessed DAS beamforming images for (a) Carrot 2, Side 1 and (b) Carrot 2, Side 2.

Table 7.1: Summary of depth measurements on the experimental trials and simulated recreation.

Carrot Test Number and Side	**Experimental Depth Measurement (cm)**	**Simulated Depth Measurement (cm)**	**True Depth (cm)**
Carrot 1, Side 1	5.75	6.13	6.29
Carrot 1, Side 2	6.05	5.93	6.26
Carrot 2, Side 1	5.45	5.53	5.61
Carrot 2, Side 2	5.30	5.33	5.51

Table 7.2: Summary of average diameter measurements on the experimental trials and simulated recreation.

Carrot Test Number and Side	Experimental Diameter Measurement (cm)	Simulated Diameter Measurement (cm)	True Diameter (cm)
Carrot 1, Side 1	2.85	2.64	2.32
Carrot 1, Side 2	2.36	2.26	2.13
Carrot 2, Side 1	2.40	2.33	2.10
Carrot 2, Side 2	2.63	2.34	2.08

7.2 Sources of Improvement

7.2.1 Developing an Automated Scanning Apparatus

At the moment the apparatus set-up for scanning roots and devices is very cumbersome and time-consuming to use. The user needs to manually measure and adjust the vertical height and angle of the transmitter and receiver. The design and implementation of an automated apparatus which automatically adjusts the rotation and the scan height will greatly improve the time it takes to conduct scans. Ideally, the apparatus would interact with the user interface that also controls the scanning of the P410. The user will be able to simply place the pot and plant to be scanned, set the desired scanning parameters, and let the apparatus conduct the scans and rotations.

7.2.2 Increasing Bandwidth and Frequency of Source Pulse

A large limitation on the resolution of the P410 device is the duration of the emitted UWB pulse. Increasing the bandwidth and the frequency of the UWB pulse results in a much shorter UWB pulse emitted. This improves the quality of the DAS beamforming images significantly since the size of the window used can be reduced, resulting in more localized regions of high intensity in the final DAS beamforming image.

The frequency of the source pulse is increased to be 2 GHz to 12 GHz. Figure 7.5 shows the pulse to be injected in the simulations. Note that the duration of this pulse is significantly shorter than all previous tests at about 0.4 ns.

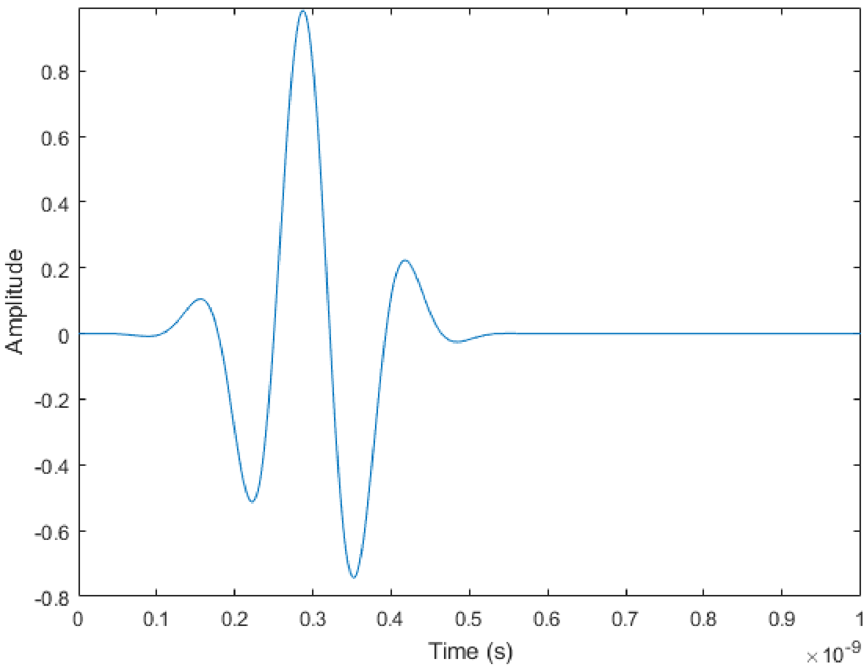

Figure 7.5: 2 GHZ to 12 GHz waveform used in high frequency simulations.

Carrot 1 is simulated again with the waveform depicted in Figure 7.5 and with the same electrical and physical parameters as before.

Figure 7.6 shows the results of increasing the frequency and bandwidth of the source pulse. The high intensity regions are much more localized around the surface of the root, resulting in much better measurements by the image analysis module.

Tables 7.3 and 7.4 summarizes the measurement results of the high frequency simulations and compares them to the experimental results.

Table 7.3: Summary of depth measurements on the high frequency simulations.

Carrot Test Number and Side	**Experimental Depth Measurement (cm)**	**Simulated High Frequency Depth Measurement (cm)**	**True Depth (cm)**
Carrot 1, Side 1	5.75	6.48	6.29
Carrot 1, Side 2	6.05	6.36	6.26

Table 7.4: Summary of average diameter measurements on the high frequency simulations.

Carrot Test Number and Side	**Experimental Width Measurement (cm)**	**Simulated High Frequency Width Measurement (cm)**	**True Width (cm)**
Carrot 1, Side 1	2.85	2.21	2.32
Carrot 1, Side 2	2.36	2.21	2.13

7.2.3 Increasing Sampling Frequency

The sampling frequency of the device severely limits the image resolution possible using DAS beamforming. Fortunately, the upsampling and interpolation method used to increase the sampling frequency can be shown to perform very well. The simulated experimental results from Figure 7.3 uses a resampled version of the simulation results to match the experimental trials after upsampling and interpolation. Figure 7.7 shows the image produced when no resampling is done and the sampling frequency is approximately 900 GSa/s, which is at the minimum time step required for simulation stability. The upsampled and interpolated figure performs very similarly to extremely high frequencies.

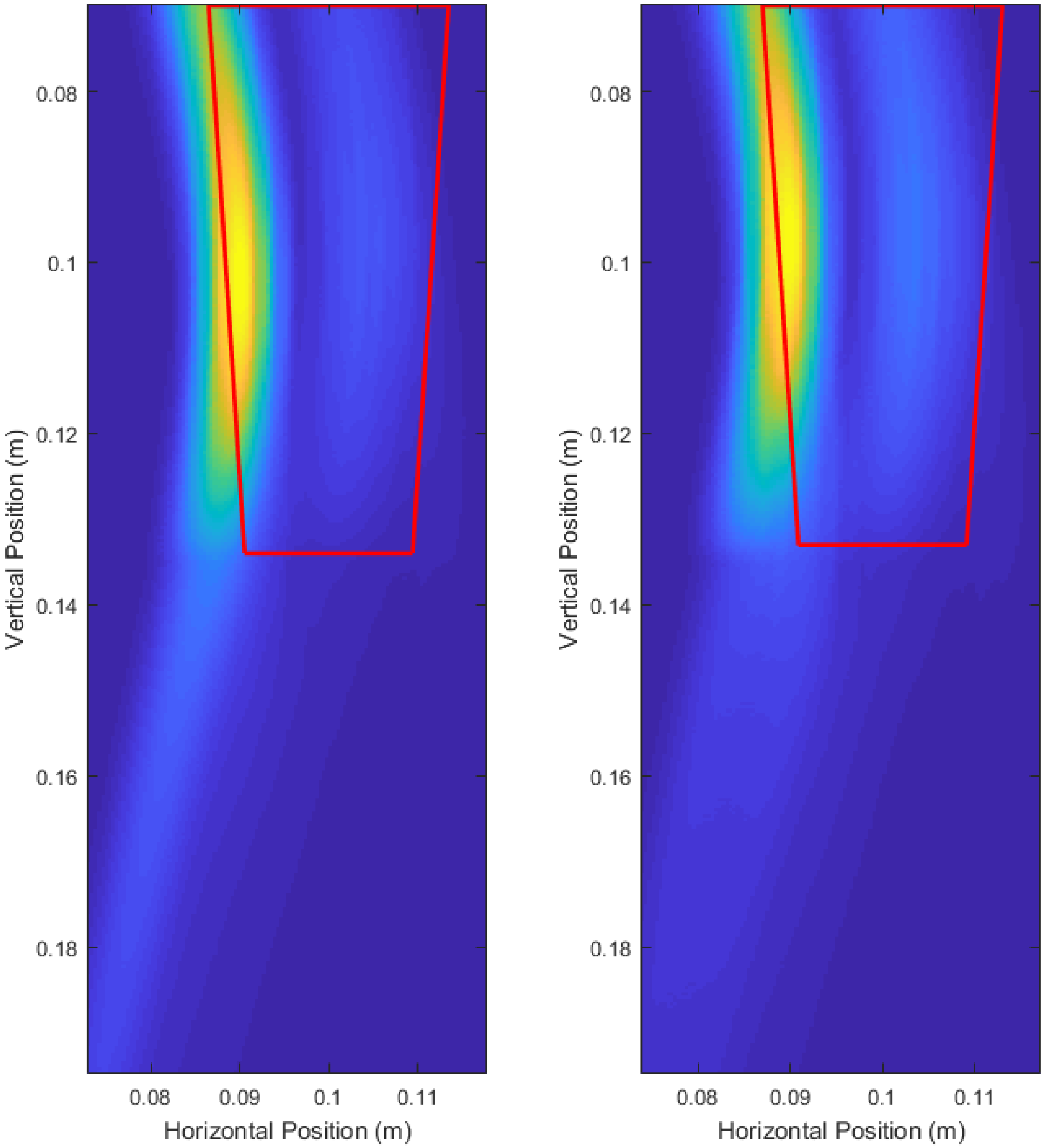

(a) Unprocessed DAS beamforming image for Carrot 1, Side 1.

(b) Unprocessed DAS beamforming image for Carrot 1, Side 2.

Figure 7.6: Unprocessed DAS beamforming images using a high frequency source pulse for (a) Carrot 1, Side 1 and (b) Carrot 1, Side 2.

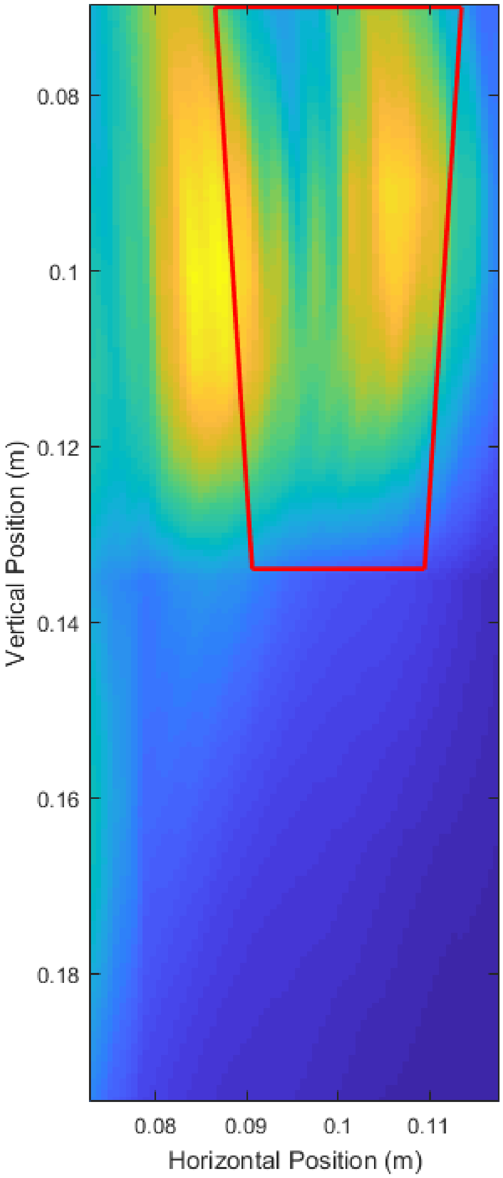

Figure 7.7: Unprocessed DAS beamforming image of Carrot 1, Side 1 with no resampling and interpolation performed.

Chapter 8

Conclusion and Future Explorations

This chapter provides a summary of the results obtained in the thesis and provides insight into the needed future work for additional improvement and research into the system designed.

8.1 Conclusion

Crop yield and crop production has seen large improvements in the last half century due to the effectiveness of plant phenotyping and the development of environmentally stress tolerant crops. Unfortunately, effective plant phenotyping requires large amounts of plant data on characteristics as the plant grows. Non-destructive root information is expensive and difficult to generate on large scales. Ultra-wideband technology has shown promise in detecting the concealed structures for weapon detection and breast cancer detection, but its use in imaging roots has been relatively unexplored.

In this thesis, an ultra-wideband system was designed to collect, process, and analyze reflection data on potted roots. Three main modules were designed: a Data Acquisition module, a Data Processing module, and an Image Processing and Analysis module.

The Data Acquisition module sought to collect data on root reflections. Initially, finite-difference time-domain simulations were done to model the electromagnetic interactions of an emitted 3.1 GHz to 5.3 GHz ultra-wideband pulse with a pot and root system under test. A non-contact, mono-static, single transceiver synthetic aperture radar set-up was used to scan the pot and root model. The root was simulated to be a taproot, a type of root which consists of a large primary root. These simulations provided reflection data until the hardware needed for the experimental trials arrived.

The Data Processing module received the reflection data from the Data Acquisition module and uses delay-and-sum beamforming to create an image. Delay-and-sum beamforming uses known physical and electrical parameters to estimate the propagation time of the ultra-wideband pulse to go from transmitter, to an arbitrary imaging point, and back to a receiver. This information was then used to create a mapping of backscattered energy as an image.

The Image Processing and Analysis module is responsible for processing and analyzing the image formed by the data processing module to detect and measure the surface location of the root that was scanned. This module measured the root depth and average root diameter in an unsupervised fashion. The error in these two measurements will be the primary metrics which the system was evaluated on.

A baseline system capable of collecting data, processing the data, and then analyzing and measuring results was created using the simulation data. From here, important parameters and limitations for each module were identified and analyzed. These parameters significantly impacted the quality of the results of the ultra-wideband imaging system and interact with each other in complex ways that need to be understood to design an optimal system.

For the Data Acquisition module, parameters such as the scan spacing, the root size, and the soil relative permittivity were examined. It was found that for larger tap roots ranging from about 15 cm depth to 35 cm depth, a scan spacing of about 3 cm is sufficient to accurately image the roots. Finer spacings result in longer scan times with marginal performance improvements, while courser spacing created artifacts which severely degraded performance. For smaller roots, a finer scan spacing is necessary for optimal performance; however, the image quality at smaller scan spacings ($\approx$1 cm) becomes limited by other parameters in the system such as the soil relative permittivity, and root relative permittivity, and source frequency. As for soil relative permittivity, it was found that a high contrast between root and soil relative permittivity is needed to have good system performance in noise. Finally, a higher source frequency ($\approx$ 2.0 GHz-12.0 GHz) was shown to have significant improvements in image quality, reducing the error of the measurements on an experimental trial from $approx$ 0.5 cm at 3.1 GHZ-5.3 GHz to $approx$ 0.1 cm at 2.0 GHZ - 12.0 GHz. Careful design of these parameters in the Data Acquisition module are critical to the performance of the ultra-wideband imaging system.

Important parameters for the Data Processing module include the steering vector design and the window size value. Delay-and-sum beamforming uses an impulse response delayed by the propagation time. The calculations for this propagation time are relatively simple for mono-static set-ups, but can complicate quickly if a bi-static set-up is used. The accuracy and processing power needed for beamforming is heavily dependent on the steering vector design. While this thesis did only a brief analysis of steering vector design, careful consideration of the steering vector is crucial for generating high quality root images. The window size value is carefully selected to be approximately one period length of the carrier frequency (0.24 ns for the 4.3 GHz carrier and 0.14 ns for the 7 GHz carrier) of the source pulse. A window size too large are more susceptible to interference and multi-path issues, while a window size too small creates image with many artifacts caused high frequency oscillations caused by the carrier frequency.

The Image Processing and Analysis module made heavy use of morphological transformations and energy histograms to process and measure the images produced by the Data Processing module. As such, the size of the structuring elements for the morphological transformations are critical to the performance of the system. For imaging larger roots, larger structuring elements can be used to remove smaller, low intensity artifacts in the image. However, structuring elements that are too large may cause the morphological transformations to erode essential root information. Likewise, for dealing with images containing high intensity noise, careful analysis of the energy histogram is needed to not remove essential root information when quantizing the image to remove large areas of low intensity noise. For roots of approximately 35 cm depth and 3 cm average diameter, circular structuring elements of approximately 4 mm in diameter were sufficient in improving measurement results. A method for calibration will be needed for determining optimal structuring element size in the future.

With knowledge of these essential parameters in mind, experimental trials were done using Time Domain's P410, an ultra-wideband device capable of transmitting and receiving a 3.1 GHz to 5.3 GHz pulse. Instead of using simulated data, experimental trials were conducted on buried carrots to analyze the limitations of the system and to verify the simulation results. A non-contact, bi-static, synthetic aperture radar set-up was used. For one test, the carrot was buried approximately 6.3 cm deep and had an average diameter of 2.2 cm. For the second test, the carrot was buried approximately 5.6 cm and had an average diameter of 2.1 cm. The implementation of this device for the Data Acquisition module brought attention to some additional issues when designing an ultra-wideband imaging system.

One issue not considered in the simulations is the noise caused by the hardware involved in the ultra-wideband pulse generation, transmission, and receiving circuits of the device. For this particular device, the hardware noise was very consistent and easily temporally isolated so a Weiner filter was able to estimate and remove the noise. For different devices, knowledge of the hardware noise and being able to effectively remove this noise is essential.

Another potential issue for hardware implementation is the sampling frequency of the devices. The P410 device had a sampling frequency of approximately 16.384 GSa/s, which severely limits the minimum pixel dimension that can be used when applying delay-and-sum beamfoming. To compensate for this, the received signals from the P410 were upsampled and interpolated. Fortunately, the upsampling and interpolation showed little degradation in image quality.

The images produced from the experimental trials performed reasonably well, but the quality was still quite poor relative to the simulated results on larger roots. For the first test, the system measured approximately a 5.9 cm depth (true depth of 6.3 cm) and a 2.6 cm average diameter (true diameter of 2.2 cm). For the second test, the system measured approximately a 5.4 cm depth (true depth of 5.6 cm) and a 2.5 cm average diameter (true diameter of 2.1 cm). Simulations were then run to recreate the parameters of the experimental trials to verify the accuracy of the simulations as well as to analyze the experimental trials for sources of improvement. With the system parameters used in this project, the non-linear and anisotropic nature of soil was not found to have a significant effect on the system since the simulated and experimental trials had similar results.

This thesis explored the feasibility of UWB technology as a low-cost and portable solution to non-destructively measure potted taproot plants. In the end, the results of this thesis has determined many important design decisions needed to the develop an UWB system for non-destructively imaging root. The success of the system itself is heavily dependent on many parameters and variables such as soil conditions, root sizes, and hardware limitations as analyzed in this thesis and future work into the imaging system must be carefully designed.

8.2 Future Work and Recommendations

Some sources of improvement such as increasing the sampling frequency and the frequency range have been suggested, simulated, and analyzed in detail in Section 7.2. In implementation, however, these improvements are not as straightforward as simply increasing sampling frequency and bandwidth. As demonstrated by the additional filtering needed to arrive at acceptable results in Chapter 6, there are many additional sources of noise. As the frequency and bandwidth increases, the effect of phenomena such as dispersion and anisotropy may become more pronounced in the final results. As previously examined in Section 5.2, knowledge the electrical properties of the soil is essential to the image forming algorithm. This is also true for methods such as MRI and PET, which also have difficulties adapting to the extremely dynamic properties of soil. Further research into devices for measuring and modeling the soil properties is needed and should be the focus of the near future research into developing UWB imaging devices for imaging the RSA.

References

[1] N. Fahlgren, M. Gehan, and I. Baxter, "Lights, camera, action: high-throughput plant phenotyping is ready for a close-up,," *Current Opinion in Plant Biology*, 2015.

[2] L. Li, Q. Zhang, and D. Huang, "A review of imaging techniques for plant phenotyping," *Sensors*, 2014.

[3] J. Araus and E. Cairns, "Field high-throughput phenotyping: the new crop breeding frontier," *Trends in Plant Science*, 2014.

[4] D. Tilman, C. Balzer, J. Hill, and B. L. Befort, "Global food demand and the sustainable intesification of agriculture," in *Proceedings of the National Academy of Sciences of the United States of America*, 2011.

[5] D. Ray, N. Ramankutty, N. Mueller, P. West, and J. Foley, "Recent patterns of crop yield growth and stagnation," *Nature Communications*, 2012.

[6] F. Fiorani and U. Schurr, "Future scenarios for plant phenotyping," *Annual Review of Plant Biology*, 2013.

[7] K.A.Nagel. (2014) Root phenotyping. [Online]. Available: http://www.plant-phenotyping.org/lw_resource/datapool/_items/item_155/22_nagel.pdf

[8] C. Peveling-Overhag and P. Schulze Lammers, "Ultra-wideband radar-sensor for non destructive analysis of storage roots," *Landtechnik*, vol. 67, no. 2, pp. 102–105, 2015.

[9] S. Mancuso, *Measuring Roots An Updated Approach.* Springer, 2012.

[10] C. Hillnhutter, R. A. Sikora, E. C. Oerke, and D. V. Dusschoten, "Nuclear magnetic resonance: A tool for imaging belowground damage caused by heterodera schachtii and rhizoctonia solani on sugar beet," *Journal of Experimental Botany*, 2012.

[11] Z.-H. Cho, Y.-D. Son, H.-K. Kim, K.-N. Kim, S.-H. Oh, J.-Y. Han, I.-K. Hong, and Y.-B. Kim, "A fusion petmri system with a high-resolution research tomograph-pet and ultra-high field 7.0t-mri for the molecular-genetic imaging of the brain," *Proteomics*, vol. 8, no. 6, pp. 1302–1323, 2008.

[12] J. Sachs, *Handbook of Ultra-Wideband Short-Range Sensing.* Wiley-VCH, 2012.

[13] A. Paez-Garcia, C. M. Motes, W.-R. Scheible, R. Chen, E. B. Blancaflor, and M. J. Monteros, "Root traits and phenotyping strategies for plant improvement," *Plants*, vol. 4, pp. 334–355, 2015.

[14] J. Grossman and K. Rice, "Evolution of root plasticity responses to variation in soil nutrient distribution and concentration." *Evolutionary Applications*, 2012.

[15] A. Wasson, R. Richards, R. Chatrath, S. Misra, S. Prasad, G. Rebetzke, J. Kirkegaard, J. Christopher, and M. Watt, "Traits and selection strategies to improve root systems and water uptake in water-limited wheat crops," *Journal of experimental botany*, vol. 63, no. 9, pp. 3485–3498, 2012.

[16] R. Haling, L. Brown, A. Bengough, I. Young, P. Hallet, P. White, and T. George, "Root hairs improve root penetration, root-soil contact, and phosphorus acquisition in soils of different strength," *Journal of experimental botany*, vol. 64, no. 3711-3721, 2013.

[17] L. A. Judd, B. E. Jackson, and W. C. Fonteno, "Advancements in root growth measurement technologies and observation capabilities for container-grown plants," *Plants*, vol. 4, pp. 369–392, 2015.

[18] M. Sarracanie, C. D. LaPierre, N. Salameh, D. E. J. Waddington, T. Witzel, and M. S. Rosen, "Low-cost high-performance mri," *Nature - Scientific Reports*, vol. 5, 2015.

[19] Medical imaging equipment guide. Block Imaging. [Online]. Available: www.blockimaging.com

[20] Spectrum analyzers. Tektronix. [Online]. Available: https://www.tek.com/

[21] Pulson 410: Monostatic, bistatic, and/or multi-static radar resources. Time Domain. [Online]. Available: http://www.timedomain.com/p400-mrm.php

[22] D. D. Silva and R. C. Beeson, "A large-volume rhizotron for evaluating root growth under natural-like soil moisture conditions," *HortScience*, 2011.

[23] L. A. Judd, B. E. Jackson, and W. C. Fonteno, "Advancements in root growth measurement technologies and observation capabilities for container-grown plants," *Plants*, vol. 4, pp. 369–392, 2015.

[24] H. Poorter, J. Buhler, D. v. Dusschoten, J. Climent, and J. A. Postma, "Pot size matters: a meta analysis of the effects of rooting volume on plant growth," *Functional Plant Biology*, 2012.

[25] D. P. Brown, T. K. Pratum, C. Bledsoe, E. D. Ford, J. S. Cothern, and D. Perry, "Noninvasive studies of conifer roots: nuclear magnetic resonance (nmr) imaging of douglas-fir seedlings," *Canadian Journal of Forest Research*, vol. 21, no. 11, pp. 1559–1566, 1991.

[26] S. Jahnke, M. I. Menzel, D. van Dusschoten, G. W. Roeb1, J. Buhler, S. Minwuyelet, P. B. mler, V. M. Temperton, T. Hombach, M. Streun, S. Beer, M. Khodaverdi, K. Ziemons, H. H. Coenen, and U. Schurr, "Combined mripet dissects dynamic changes in plant structures and functions," *The Plant Journal*, vol. 59, pp. 634–644, 2009.

[27] S. R. Tracy, J. A. Roberts, C. R. Black, A. McNeill, R. Davidson, and S. J. Mooney, "The x-factor: visualizing undisturbed root architecture in soils using x-ray computed tomography," *Journal of Experimental Botany*, vol. 61, pp. 311–313, 2010.

[28] M. Lontoc-Roy, P. Dutilleul, S. O. Prasher, L. Han, T. Brouillet, and D. L.Smith, "Advances in the acquisition and analysis of ct scan data to isolate a crop root system from the soil medium and quantify root system complexity in 3-d space," *Geoderma*, vol. 137, pp. 231–241, 2006.

[29] S. Mairhofer, S. Zappala, S. Tracy, C. Sturrock, M. J. Bennett, S. J. Mooney, and T. Paul, "Recovering complete plant root system architectures from soil via x-ray - computed tomography," *Plant Methods*, vol. 9, 2013.

[30] H. Ozier-Lafontaine and T. Bajazet, "Analysis of root growth by impedance spectroscopy (eis)," *Plant and Soil*, vol. 277, pp. 299–313, 2005.

[31] Y. Cao, T. Repo, R. Silvennoinen, T. Lehto, and P. Pelkonen, "An appraisal of the electrical resistance method for assessing root surface area," *Journal of Experimental Botany*, vol. 61, no. 9, pp. 2491–2497, 2010.

[32] M. Amato, B. Basso, G. Celano, G. Celano, G. Bitella, G. Morelli, and R. Rossi, "In situ detection of tree root distribution and biomass by multi-electrode resistivity imaging," *Tree Physiology*, vol. 28, pp. 1441–1448, 2008.

[33] M. Amato, G. Bitella, R. Rossi, J. A. Gomez, S. Lovelli, and J. Gomes, "Multi-electrode 3d resistivity imaging of alfalfa root zone," *European Journal of Agronomy*, vol. 31, pp. 213–222, 2009.

[34] T. Zenone, G. Morelli, M. Teobaldelli, F. Fischanger, M. Matteucci, M. Sordini, A. Armani, C. Ferre, T. Chiti, and G. Seufert, "Preliminary use of ground-penetrating radar and electrical resistivity tomography to study tree roots in pine forests and poplar plantations," *Functional Plant Biology*, vol. 35, pp. 1047–1058, 2008.

[35] J. R. Butnor and K. H. Johnsen, "Imaging tree roots with borehole radar," in *11th International Conference on Ground Penetrating Radar*, Ohio, USA, 2006.

[36] N. Bassuk, J. Grabosky, A. Mucciardi, and G. Raffel, "Ground-penetrating radar accurately locates tree roots in two soil media under pavement," *Arboriculture and Urban Forestry*, vol. 37, no. 4, pp. 160–166, 2011.

[37] X. Cui, L. Guo, J. Chen, X. Chen, and X. Zhu, "Estimating tree-root biomass in different depths using ground-penetrating radar: Evidence from a controlled experiment," *IEEE Transactions on Geoscience and Remote Sensing*, vol. 51, no. 6, 2013.

[38] X. Zhuge, "Short-range ultra-wideband imaging with multiple-input multiple-output arrays," Ph.D. dissertation, Delft University of Technology, 2010.

[39] M. Yuce, *Ultra-Wideband and 60 GHz Communications for Biomedical Applications.* Springer, 2014.

[40] M. Dupuis, *RSS-220 Devices Using Ultra-Wideband (UWB) Technology*, 2009.

[41] L. Nhien, T. Thai, N. Thang, A. Dinh, and T. V. Van, "Design and implementation of a low-cost device for breast cancer detection using ultra wide band technology," *International Conference on the Development of Biomedical Engineering in Vietnam*, 2017.

[42] H. K. Bidhendi, H. M. Jafari, and R. Genov, *Ultra-Wideband Imaging Systems for Breast Cancer Detection.* Springer, 2014.

[43] T. Henriksson, M. Klemm, D. Gibbins, J. Leendertz, T. Horseman, A. W. Preece, R. Benhamin, and I. Craddock, "Clinical trials of a multistatic uwb radar for breast imaging," in *Antennas and Propagation Conference (LAPC)*, 2011.

[44] M. Klemm, I. Craddock, J. Leendertz, A. Preece, and R. Benjamin, "Experimental and clinical results of breast cancer detection using uwb microwave radar," in *Antennas and Propagation Society International Symposium*, 2008.

[45] C. Peveling-Oberhag, "Erfassung der wurzelarchitektur von zuckerrben und mangold mittels uwb-radar," Ph.D. dissertation, University of Bonn, 2013.

[46] R. L. van Dam, B. Borschers, and J. M. H. Hendricks, "Methods for prediction of soil dielectric properties: a review," in *Proceedings of the SPIE, Volume 5794, p. 188-197*, 2005.

[47] D. A. Boyarskii, V. V. Tikhonov, and N. Y. Komaroba, "Model of dielectric constant of bound water in soil for applications of remote sensing," *Progress in Electromagnetics Research*, 2002.

[48] J. R. Wang and T. J. Schmugge, "An emperical model for the complex dielectric permittivity of soils as a function of water content," *IEEE Transactions on Geoscience and Remote Sensing*, 1979.

[49] A. Taflove and S. C. Hagness, *Computational Electrodynamics, the finite-difference time-domain method.* Artech House, 2005.

[50] R. C. Rumpf. (2017) Electromagnetic analysis using the finite-difference time-domain method. Lecture Notes from EE 5303 at the University of Texas at El Paso. [Online]. Available: http://emlab.utep.edu/ee5390fdtd.htm

[51] K. Yee, "Numerical solution of initial boundary value problems involving maxwell's equations in isotropic media," *IEEE Transactions on Antennas and Propogation*, vol. 14, no. 3, pp. 302–307, 1966.

[52] S.O.Kasap, *Optoelectronics and Photonics.* Pearson Education Limited, 2013.

[53] MATLAB, *Documentation in version 9.2.0.538062 (R2017a).* Natick, Massachusetts: The MathWorks Inc., 2017.

[54] Canola Council of Canada. (2014) Canola growth stages. [Online]. Available: http://www.canolacouncil.org/canola-encyclopedia/crop-development/growth-stages/

[55] V. K. Madisetti, *The Digital Signal Processing Handbook, Second Edition.* CRC Press, 2009.

[56] *Canadian Table of Frequency Allocations*, 2014. [Online]. Available: http://www.ic.gc.ca/eic/site/smt-gst.nsf/eng/sf10759.html

[57] J. Xua, S. D. Logsdonb, X. Ma, R. Hortond, W. Hane, and Y. Zhaoe, "Measurement of soil water content with dielectric dispersion frequency," *Soil Science Society of America Journal*, vol. 78, no. 5, pp. 1500–1506, 2014.

Appendix

Additional Imaged Results on Various Taproots

A.1 Potato

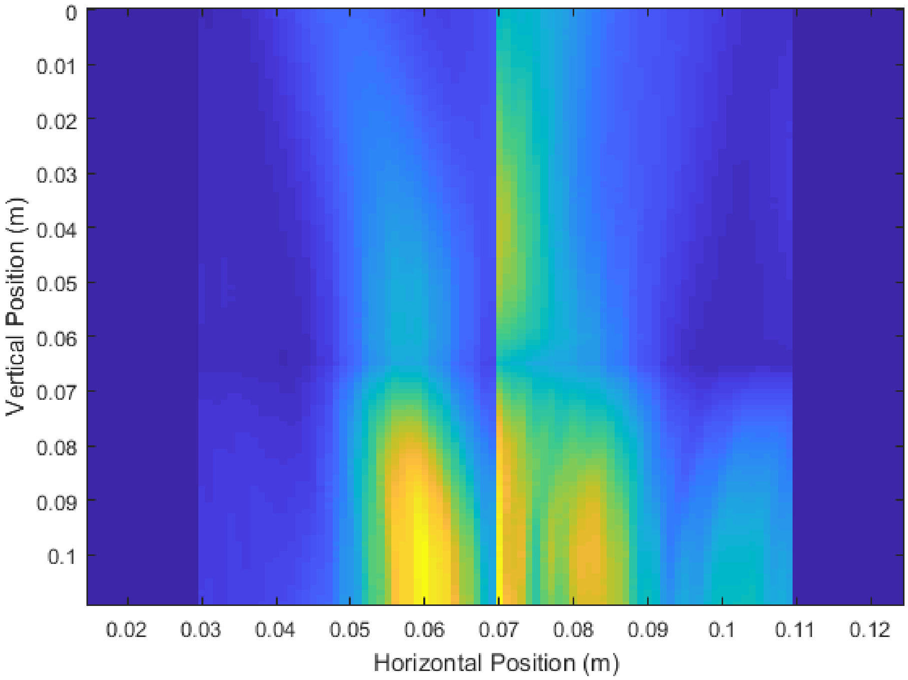

Figure A.1: Unprocessed DAS beamforming results of a potato taken at 0°and 180°.

Figure A.1 shows the imaging results of a buried potato of approximately 9 cm depth and 4 cm average width. The quality is very poor, and upon brief examination reveals that the amplitude of reflections of the potato are of similar amplitude to noise in the signal. This is likely due to a poor relative permittivity contrast between soil and root and also the presence of scattering heterogeneities in the soil.

A.2 Beet

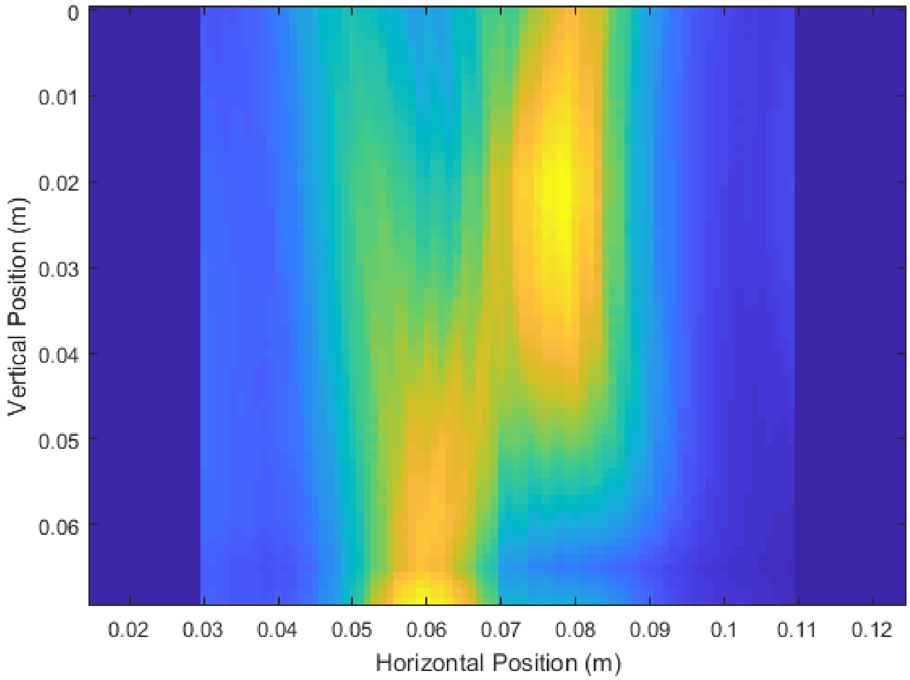

Figure A.2: Unprocessed DAS beamforming results of a beet root taken at 0°and 180°.

Figure A.2 shows the imaging results of a buried red beet with approximately 6 cm depth and 5 cm average width. The image taken at 0°is dominated by scatterers in the soil medium, but the outline of the beet is still somewhat present.

A.3 Additional Carrot

Figures A.3 to A.6 contain the imaging results from various angles on a carrot of approximately 6 cm depth and 3 cm average width. Again, some occasional artifacts arise, likely from some unwanted high energy reflections caused by heterogeneities in the soil.

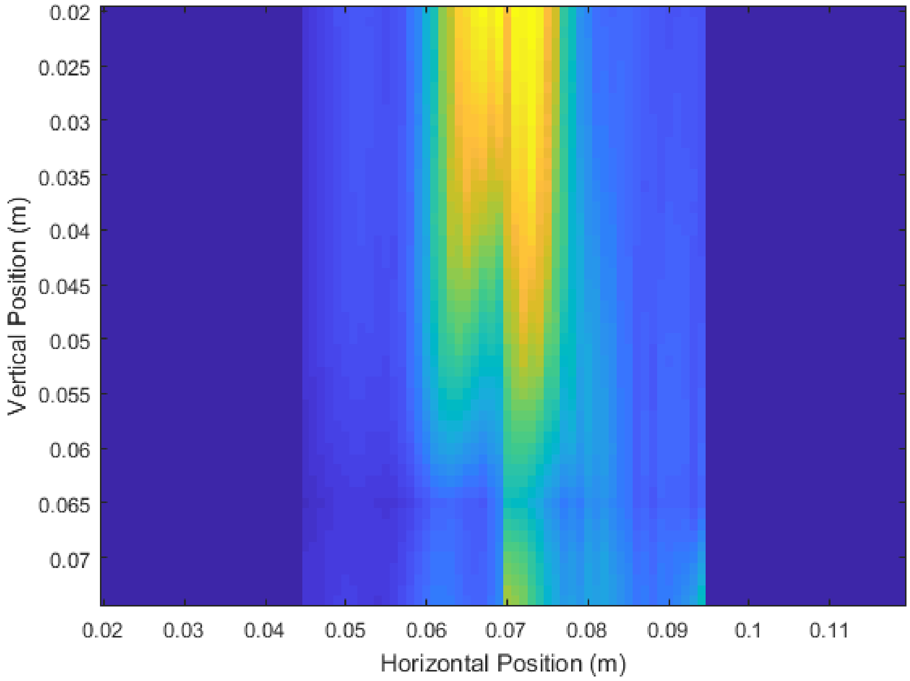

Figure A.3: Unprocessed DAS beamforming results of a carrot taken at 0°and 180°.

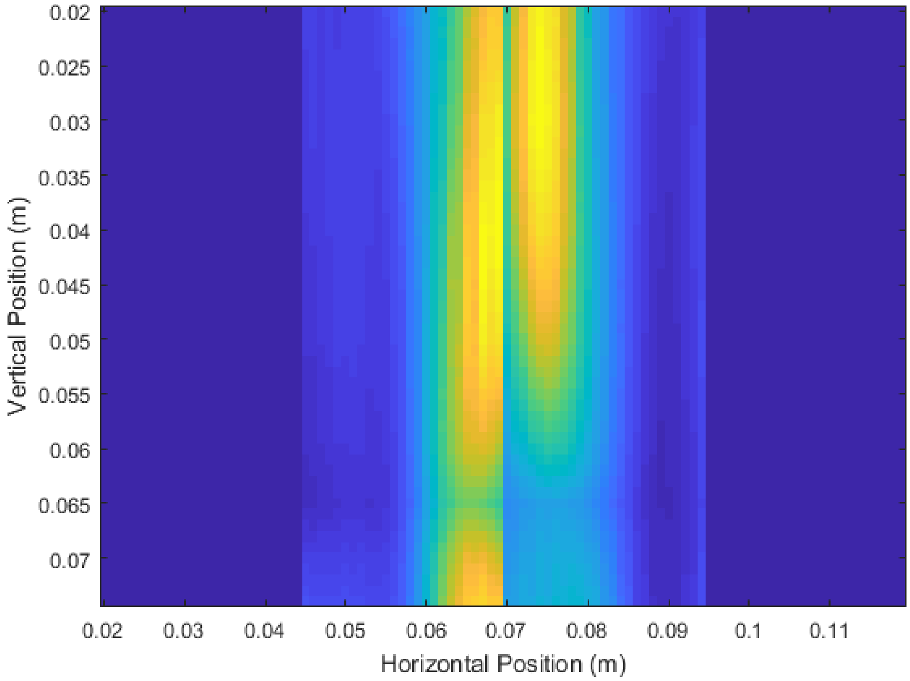

Figure A.4: Unprocessed DAS beamforming results of a carrot taken at 45°and 225°.

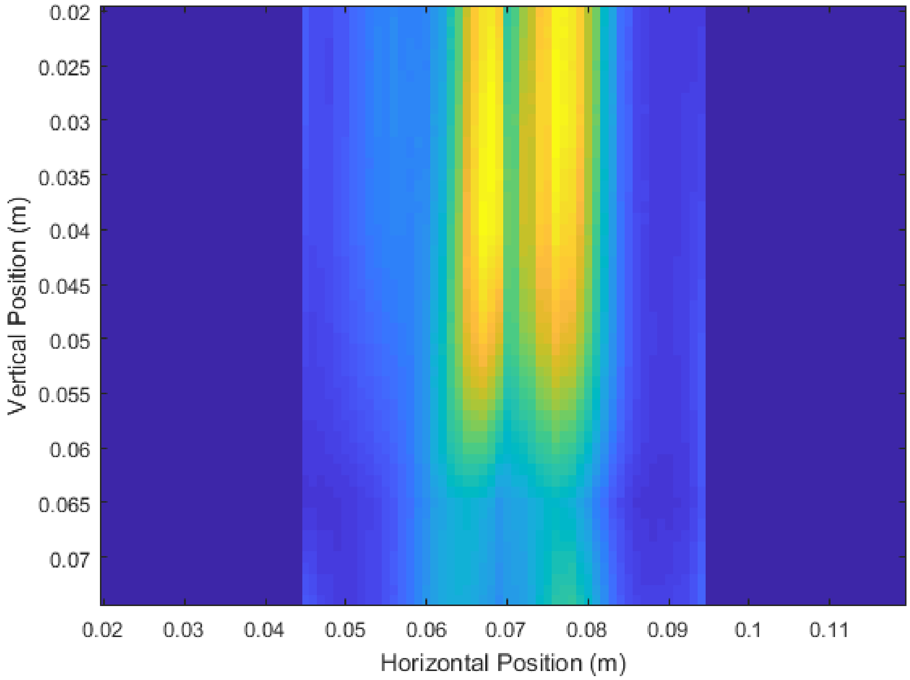

Figure A.5: Unprocessed DAS beamforming results of a carrot taken at 90°and 270°.

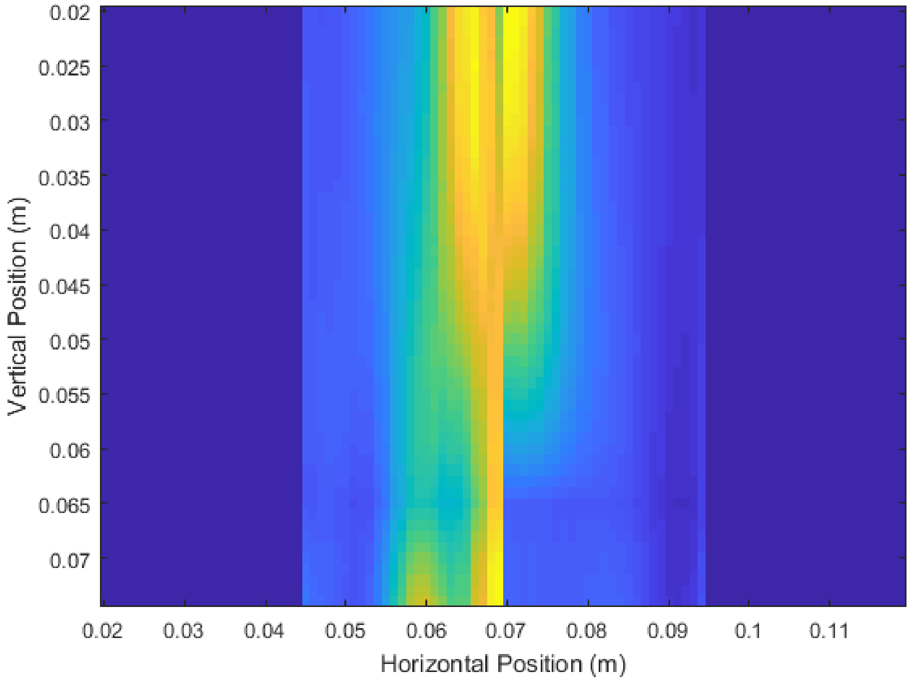

Figure A.6: Unprocessed DAS beamforming results of a carrot taken at 135°and 315°.